Chiral interactions of Quantum Dots embedded within Nanophotonic Waveguides

David Michael Price

Submitted for the degree of Doctor of Philosophy

Department of Physics and Astronomy

University of Sheffield

February 26, 2019

ii

Abstract

This thesis describes the couplings and interactions of quantum dots embedded within nanoscale photonic waveguides. Optical spectroscopic measurements were performed on these devices for the development of integrated quantum optical circuits using III-V semiconductors and self-assembled quantum dots.

Due to the confinement of electromagnetic radiation in photonic structures, it is possible to have a longitudinal component of the electric field within a waveguide, opposed to only a transverse component. This means that the electric field experienced by an emitter varies depending on the position of the emitter within the waveguide. In the symmetric case emission rates are equal along each arm of the waveguide. For a non-symmetric case (a chiral case) the emission for a QD exciton transition is not equal along both waveguide arms. In the most extreme case unidirectinal emission arises. Using this, a method of directly reading out the spin state of an emitter via spin to path conversion is achieved.

By injecting quasi-resonant light into one side of the QD-waveguide system, determining the propagation direction, it is possible to selectively excite QD exciton transitions. This path to spin conversion breaks the reciprocity

of the system, as light travelling the opposite direction will only interact with the orthogonal QD component. The subsequent re-emission is also directional.

Resonant transmission and reflection measurments are performed on a chirally coupled QD in a waveguide geometry. Dips in the transmission and peaks in the reflection spectra are observed. The chiral interface causes an asymmetry to be observed in transmission for opposite helicity QD exciton components. An asymmetry is also observed in reflection, which is unexpected, but is explained by use of a numerical model which reveals the effect is due to partial saturation of the more strongly coupled QD exciton component.

Acknowledgements

Firstly, I would like to thank my supervisor Maurice Skolnick for all the support, knowledge, and guidance I have received during my Ph.D and in the writing of this thesis. I would also like to thank Maxim Makhonin for his efforts inside and outside of the lab, and thank all the members of the LDSD group with whom I have had many fruitful discussions and who have helped me greatly. Lastly, I have to thank my wife Leanne, for her continued encouragement and tolerance during the harder times.

List of publications

Chirality of nanophotonic waveguide with embedded quantum emitter for unidirectional spin transfer

R. J. Coles, <u>D. M. Price</u>, J. E. Dixon, B. Royall, E. Clarke, P. Kok, M. S. Skolnick, A. M. Fox and M. N. Makhonin

Nature Communications **7**, 11183 (2016)

Path-dependent initialization of a single quantum dot exciton spin in a nanophotonic waveguide

R. J. Coles, <u>D. M. Price</u>, B. Royall, E. Clarke, M. S. Skolnick, A. M. Fox and M. N. Makhonin

Physical Review B **95**, 121401(R) (2017)

Nonreciprocal Transmission and Reflection of a Chirally Coupled Quantum Dot

D. L. Hurst, <u>D. M. Price</u>, C. Bentham, N. M. Makhonin, B. Royall, E. Clarke, P. Kok, L. R. Wilson, M. S. Skolnick and A. M. Fox

Nano Letters **18 (9)**, (2018)

Contents

List of Figures

Chapter 1

Introduction

1.1 Introduction

In 1982, Richard Feynman proposed that a new kind of computer would be needed to perform quantum simulations[1]; a quantum computer. Such a computer would need quantum elements to operate and should offer many advantages over classical computing, such as increased security and a speed up in calculation times. There have been several algorithms reported which show the benefit that quantum computers may have when compared to classical computers. Two well known algorithms are Shor's and Grover's, which deal with large prime number factorisation[2] and the searching of unordered lists[3] respectively.

Several schemes have been suggested as potential platforms for a physical implementation of quantum computing, such as cold trapped ions[4], Cooper pairs[5] and others[6, 7, 8]. Using photons offers an attractive route to quantum computing as information can easily be encoded in the polarisa-

tion or path of the photon. Photons are also largely free from decoherence issues which can be a major problem using other systems[9]. A quantum computer can be realised with the use of single-photon sources and detectors combined with linear optical elements, such as beam splitters and phase shifters[10], and is referred to as linear optical quantum computing (LOQC). Current LOQC demonstrations use externally located single photon sources connected to often relatively large scale optical setups[11, 12] or waveguide circuits[13, 14]. These current schemes are difficult, if not impossible to scale up, and so single photon sources will need incorporating with quantum elements and circuitry[15] in compact and scalable architectures.

1.1.1 Scope of this thesis

This thesis focuses on the interactions between InGaAs quatum dots embedded within GaAs nanophotonic structures, specifically waveguides, which can contain and direct the flow of light. By tailoring the coupling between an emitter and the photonic environment in which it resides, directional emission of photons can take place where the photons can be routed a specific way along the waveguide, as well as the breaking of reciprocity.

In chapter 2, a brief introduction to quantum information processing is presented along with basic concepts of semiconductor quantum dots and information about photonic waveguides.

Chapter 3 concerns the computational and experimental methods used in this work. Methods used for the simulation and experimental work is presented here.

Chapter 4 introduces the directional emission of photons from QDs arising

from their local positions within the waveguides. Simulations are used in conjunction with experimental work; and a method of registering the QD position is used to verify findings from simulations and randomly distributed QDs. The chiral interface that arises due to the local fields within photonic structures is introduced here also.

Chapter 5 demonstrates the quasi-resonant initialisation of a QD exciton in a waveguide geometry, where the path of the excitation photon determines the spin state of the QD upon absorption. Subsequent re-emission is also directional as shown in Chapter 4.

Chapter 6 investigates resonant interactions between an excitation field and a chirally-coupled QD embedded within a photonic waveguide. Transmission and reflection measurments are performed and the non-reciprocal nature of this system is shown again.

Finally, chapter 7 gives a summary of the experimental chapters and an overview of potential future work.

Chapter 2

Background

2.1   Introduction

In this chapter some basic semiconductor quantum dot (QD) physics is presented and discussed, such as the optical properties of Indium Arsenide (InAs) QDs. Some background information, which may be useful for the understanding of future chapters, is also included.

2.2   Quantum Information Processing

Quantum information processing (QIP) offers many advantages over its classical counterpart in terms of computational performance and security[16]. A connected network of quantum nodes would allow the sending and receiving of secure information via a quantum internet[17]. Most current demonstrations of principles required for QIP rely on large scale optical setups. This limits the scalability of this technology and as such miniaturisation of the

5

components is needed. This could be done by developing integrated low loss optical components with photonic waveguide circuits[18]. There has been progress towards this goal with integrated optical components, such as beam splitters (BS), and using embedded quantum dots as single photon sources.

Classically, digital data is stored as a series of binary 'bits', which can take values of either 0 or 1. The information can be processed by passing it through a series of logic gates, which may change the value of the bit if certain criteria are met. Classical information processing, however, has a limit and in an attempt to overcome this limit, a scheme based on quantum mechanical effects has been proposed. In analogy to the classical 'bits' used in classical information processing; quantum information processing will be done using 'quantum bits' or 'qubits'. A qubit can not only be in the pure states of 0 or 1, but it can also be in both states at the same time, a quantum mechanical effect known as the superposition principle[19]. The state of a qubit is described by its wavefunction, given by,

$$|\Psi\rangle = \alpha|0\rangle + \beta|1\rangle \tag{2.1}$$

where α and β are complex amplitudes with a requirement that,

$$|\alpha|^2 + |\beta|^2 = 1 \tag{2.2}$$

The ability to process information taking advantage of the superposition principle allows several calculations to be performed simultaneously. There are many other advantages that quantum mechanics can offer to information processing, that are not available in classical systems, such as quantum entanglement and quantum logic gates, such as the hadamard gate, which have

no classical analogues. Shor's algorithm and Deutsch's algorithm are two schemes that show QIP can be faster than classical information processing. To fully realise QIP in the solid state a number of requirements for the chosen two-level system must be met. These requirements of the physical hardware are given by the DiVincenzo criteria[20]. One example of such a criterion is that the decoherence time of the qubit state, once initialised, must be much longer than the gate operation time.

The ability to transmit information from one place to another is also a highly sought after property of many QIP schemes. In proposed schemes, such as using QDs in III-V semiconductor materials, a qubit state would need to be initialised, stored and processed in QDs (nodes). The nodes then need to be linked. This could be done with photons which will act as 'flying' qubits, these will travel and carry information between the nodes[21].

A number of structures already exist which can control the flow of light, such as nanowires, which control the photon path using total internal reflection (TIR). Photonic crystals (PhCs) are another technology that can confine and control the flow of light[22]. The spin state of a QD has potential to be used as a static qubit in QIP applications. It has been reported that these systems can have coherence times of microseconds[23, 24] and radiative lifetime limited optical transitions[25] making them useful for QIP.

2.3 Single photon sources

Single photon sources (SPS) only emit one photon at any given time. An ideal two level quantum emitter would be an SPS. They are an important

requirement in many applications of QIP. Many quantum cryptography protocols, such as quantum key distribution[26] demand single photons, as more than one photon could allow an eavesdropper to gain information and render the communication channel insecure[27]. An ideal SPS[28] would emit photons 'on-demand', the photons would be indistinguishable[29] and the emitter should have a fast repetition rate. There are several examples of systems that can be used as sources of single photons, such as; quantum dots[30], colour centres[31], single atoms[32], ions[33], molecules[34] and atomic ensembles.

2.4   Semiconductor Quantum Dots

Quantum dots (QDs) are nanometre sized objects which can confine electrons and holes in all three spatial directions; on the order of their wavelength[35]. Quantum dots can be produced in a variety of ways[35, 36, 37, 38, 39, 40, 41], each with their own advantages and disadvantages, but in general consist of an inner region surrounded by a region with a larger bandgap. This helps improve the quantum efficiencies of quantum dots as they help reduce the number of non-radiative recombination paths. In the following work Stranski–Krastanov (SK) QDs are used. These QDs are epitaxial self-assembled quantum dots (SAQDs), and have properties desirable for quantum information processing. Self-assembled quantum dots (SAQDs) made from indium arsenide (InAs) in a gallium arsenide (GaAs) matrix are used throughout the work presented in this thesis. InAs QDs offer an excellent source of single photons with a near zero probability of multi-photon emission[42, 43, 44, 45, 46, 47, 48]. QDs have been produced in other semicon-

ductor material systems including groups II-VI[38, 49, 50], III-V and IV[51]. Semiconductor fabrication technologies, such as EBL and ICP etching, are relatively mature, and offer a route to creating photonic circuits with embedded QDs (see section 3.3.2). All the work presented in this thesis uses InAs SAQDs in GaAs photonic waveguides (see section 2.8).

2.4.1 Electronic and Optical Properties of InAs QDs

InAs QDs are islands of InAs enclosed by a region of GaAs. Bulk InAs and GaAs have bandgaps of 0.35eV and 1.42eV (at 300K) respectively. The large difference in bandgaps enables charge carriers to be captured and held in quantised states (see figure 2.1). A three-dimensional potential well is formed, as the inner region (InAs) is energetically favourable for charge carriers to reside in, requiring additional energy to escape. In reality the difference in bandgaps is not as large as the difference of the two bulk materials. This is due to several factors such as; strain effects[52] due to the lattice mismatch[53] between the materials and diffusion of Ga through the QD[54]. Confinement effects also offset the lowest energy levels from the band edge by approximately 70-100meV and 400-500meV for the valence and conduction bands respectively[55]. A typical energy splitting of a captured electron and hole is 1.33eV. The emission energy of a QD also depends of the growth parameters such as size and shape. A schematic diagram showing the energy levels of a QD is presented in figure 2.1.

InAs QDs have many properties that make them useful for QIP applications. InAs is a direct bandgap semiconductor[56] meaning efficient radiative decay may take place. The emission energy of a photon emitted by an InAs
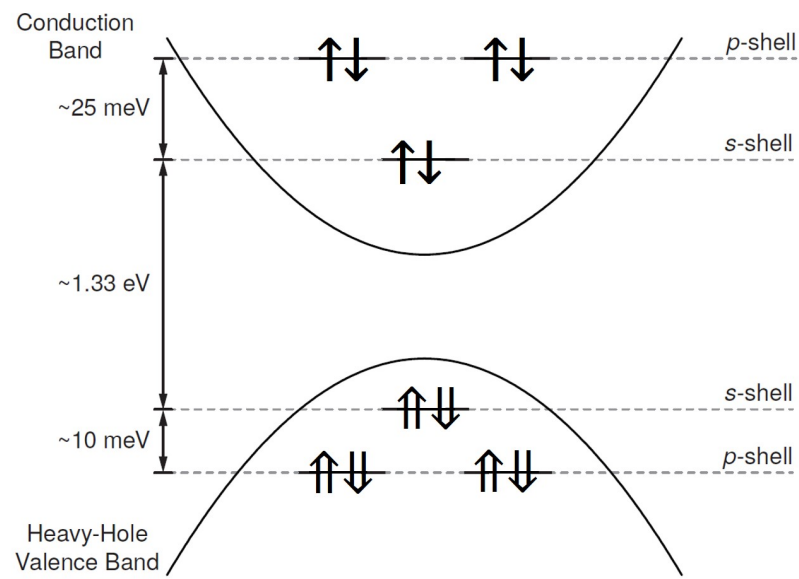
Figure 2.1: Energy level diagram of the s and p-shells within a QD. Energy level spacing is not to scale. Exact energy level spacing depends upon QD growth parameters.

QD is lower than the bandgap of GaAs, meaning the photon is able to travel throughout the material without re-absorption. Some of the light confinement in waveguides is provided by total internal reflection (TIR), where light is reflected from a boundary if a critical angle is exceeded, and the relatively high refractive index of GaAs helps keep the light confined. The emission energy of the QD is close to the GaAs bandgap energy, which enables captured carriers to be scattered out of the QD by phonon interactions at energies kT (where k is the Boltzman constant and T is the temperature), meaning that InAs QDs need cooling ($<$50K) to minimise the effect of the phonons and for any quantum effects to be observed. By minimising the thermal energy of charge carriers it is possible for a QD to capture a single electron and hole and have them populate the lowest energy level of the conduction and valence bands respectively. The band structure of a QD in this regime is well approximated by a two-level system and as such may be referred to as 'artificial atoms'[57].

As electrons and holes have opposite charges they will be electrostatically attracted to one another. In a QD they can form a bound excitonic state. A single electron and hole will form a neutral exciton. However, several different excitonic states exist; such as charged excitons where there are differing numbers of electrons and holes bound within the QD, and biexcitons which have two electrons and holes. The biexciton decays by emission of two photons sequentially and it has been shown that these photons are entangled[58]. Using the biexciton cascade, where the biexciton decays to the ground state via the sequential emission of two orthogonally polarised photons, as an entangled photon source[59, 60, 61] and in quantum telepor-

tation experiments[62] has been demonstrated. These states are optically active but the Coulomb interaction between the electrons and holes in the biexciton cause it to have a different energy when compared to the neutral exciton. Excitonic states containing more than two electrons and holes[63] are not considered in this work and the majority of the measurements are performed on neutral or charged excitons (trions). In the neutral exciton an electron in the conduction band has an angular momentum of $l = 0$ (s-type) and a spin of $s = \pm 1/2$, and a hole in the valence band level has $l = 1$ (p-type) and $s = \pm 1/2$. The hole states have $m_j = \pm 1/2$ (light hole states) and $m_j = \pm 3/2$ (heavy hole states) where the degeneracy is lifted due to lattice mismatch induced strain between the GaAs and InAs. The energy level splitting of light and heavy holes are $\sim 30meV$. The light hole states are usually ignored when considering the lowest energy states of the QD. This gives total angular momentum values of $m_j = \pm 1, \pm 2$ as there are 4 possible combinations of electron and hole angular momentum; $-\frac{3}{2} + \frac{1}{2}, -\frac{3}{2} - \frac{1}{2}, \frac{3}{2} + \frac{1}{2}$ and $-\frac{3}{2} - \frac{1}{2}$. As photons always have an angular momentum of 1, the $m_j = \pm 2$ cannot recombine optically and are called dark states. The $m_j = \pm 1$ states are optically allowed according to dipole selection rules and are called bright states. In a perfectly symmetrical QD the bright states are degenerate. In real systems there is QD asymmetry which lifts the degeneracy of the two states, this is due to the electron-hole exchange interaction, and is also known as fine structure splitting (FSS). The polarisation of the emitted states are orthogonal to one another.

2.5 Zeeman effect

The Zeeman effect in atomic physics is characterised by the splitting of atomic levels into magnetic sublevels. The effect is the same in semiconductor QD physics, that is, application of a magnetic field will energetically separate degenerate states. For example, when no magnetic field is applied, the σ^+ and σ^- transition energies of a trion (charged exciton), are degenerate. When a magnetic field is applied the degenerate states will split and their energies will be given by: $h\nu_X(S_z) = h\nu_0 \pm \mu_B g_X B_z S_z$, where g_x is the excitonic g-factor, which is different for every QD, but has a typical value around ∼1.2.

2.6 Quantum-Confined Stark Effect

As the QDs studied in this work are SKQDs, they have a range of possible emission energies, and being able to tune the emission energies of individual QDs enables many physical phenomena to be observed. By applying an electric field across a photonic device (see section 3.3.3), the band structure can be modified, resulting in a change in the emission energy of embedded QDs. Any charge carriers confined to the QD will have their energy separation reduced, reducing the energy of the emitted photons upon recombination. They will remain confined to the QD as the band gap difference between the InAs QD and surrounding GaAs is relatively large. The change in emission energy with applied electric field is known as the quantum-confined Stark effect[64] (QCSE). The change in emission energy, E, is given by

$$\Delta E = pF + \beta F^2 \qquad (2.3)$$

where F is the electric field strength, p, is the electric dipole moment and β, is the polarisability. As the electric field strength is increased, the energy separation of the electron and hole will decrease. This process continues until the electric field is large enough to cause the charge carriers to tunnel out of the QD before they recombine. Tuning ranges of up to 25meV have been shown in the literature[65] using barriers to minimise the probability of carriers tunelling out of the sample. The QCSE is also of great interest for QIP applications as it provides a method of tuning the emission from a QD source. Using this tuning method it is possible to tune the emission of a single QD exciton into resonance with emission from another remote QD[66]. This process is in theory scalable, but the emission from each QD would need to be tuned individually, which may be difficult as the number of QDs increases.

2.7 Cavity Quantum Electrodynamics

2.7.1 Introduction

Cavity quantum electrodynamics describes the behaviour of systems, whereby a quantum emitter in a cavity can absorb and emit photons from and into cavity modes. Standing waves form in the cavity and depending on the frequency of the radiation, constructive and destructive interference can occur. Destructive interference can cause some frequencies to not be supported by the cavity (a photonic bandgap) and other frequencies will be amplified. The amplified frequencies will be resonant with the cavity, ω_{cav}, with the resonant frequencies defined by the properties of the cavity. The cavity changes the

density of states of the emitter and leads to increased emission into the cavity mode while supressing emission into other modes.

In an ideal cavity, the resonant modes would take the form of delta functions. In reality, however, the resonant modes are broadened due to imperfections and this leads to a reduction in the lifetime of the cavity photons. One measure used to characterise a cavity is the quality factor (Q-factor) of the cavity, and is given by

$$Q = \frac{\omega_{cav}}{\kappa} \tag{2.4}$$

where κ is the photon loss rate from the cavity. Another value used to describe the cavity is the mode volume, V, this is defined as the integral of the normalised electric field energy density over the cavity volume. The mode volume is usually given in units of cubic wavelengths $(\frac{\lambda}{n})^3$, where n is the refractive index of the cavity.

The emission properties of an emitter coupled to a cavity are modified compared to those of an emitter in free space. The interaction between the emitter and the cavity can be characterised by three parameters. These are the photon loss rate from the cavity, κ, the non-resonant decay rate, γ, and the emitter-photon coupling rate, g_0. The non-resonant decay rate is the rate of emission into unsupported cavity modes and any non-radiative decay paths. For InAs QDs at low temperatures the non-radiative decay rate is negligible[67] and emission into non-resonant cavity modes varies based on cavity design and the quality of fabrication.

The emitter-photon coupling rate gives the rate at which energy is transfered between the cavity and the emitter. It is given by

$$g_0 = \sqrt{\frac{\mu^2 \omega}{2\epsilon_0 hV}} \tag{2.5}$$

where μ is the electric dipole matrix element for the emitter and ϵ_0 is the permitivity of free space. The matrix element is determined by the properties of the emitter as well as the cavity mode volume. The coupling between the emitter and the cavity can be classified into two coupling regimes. A system is in the weak coupling regime when photons are more likely to be lost from the cavity before the emitter is able to absorb them, i.e $g_0 \gg (\kappa, \gamma)$. The strong coupling regime is where photons have a greater chance of being re-absorbed by the emitter, and re-emitted, than lost from the cavity, i.e $g_0 \ll (\kappa, \gamma)$.

2.7.2   Weak Coupling

As stated above, the emission properties of an emitter are modified when placed in a cavity. Fermi's golden rule states that the transition rate of an emitter is proportional to the density of final states. A cavity changes the density of states for an emitter and so the emission properties also change. This is known as the Purcell effect[68] and was first observed with atoms in a resonant circuit cavity. The enhancement or inhibition of emission is described by the Purcell factor, which is the ratio of spontaneous emission rate in the cavity, Γ_{cav}, and the spontaneous rate in free space, Γ_{fs}. The Purcell factor is given by

$$F_P = \frac{\Gamma_{cav}}{\Gamma_{fs}} = \frac{3}{4\pi^2}(\frac{\lambda}{n})^3(\frac{Q}{V})\epsilon^2 L(\omega) \tag{2.6}$$

where $\frac{\lambda}{n}$ is the wavelength in the material and $L(\omega)$ is the lineshape of

the cavity. ϵ is the normalised dipole orientation factor which represents the overlap between the emitter and cavity in terms of location and polarisation.

2.7.3 Strong Coupling

In the strong coupling regime, photons will remain in the cavity for a long enough period that they may be reabsorbed several times by the emitter before leaving the cavity. In this case, the absorption from and re-emission into the cavity by the emitter can be considered a reversible process. A two-level system coupled to a resonant cavity is described by the Jaynes-Cummings model[69]. The oscillations between a photon in the cavity and the excited state of the emitter are known as vacuum Rabi oscillations[70]. A quasi-particle known as an exciton-polariton[71] is formed. Strong coupling is shown experimentally by the observation of an anti-crossing[72, 73] when tuning either the cavity or emitter through resonance with the other. On resonance, a splitting between the energy of the cavity and emitter is observed[74, 75].

2.7.4 Photonic Crystals

Photonic crystals (PhCs) are periodic arrangements of dielectric material in one, two or three dimensions. Just as an electronic bandgap can arise from the periodic arrangement of atoms in a semiconductor, a photonic bandgap can arise in photonic crystals. Photonic crystals were first considered in 1987 by Yablonovitch[76] and John[77] as a way to influence or define the optical modes of a material.

Photonic crystal cavities are challenging to fabricate as the periodicity of
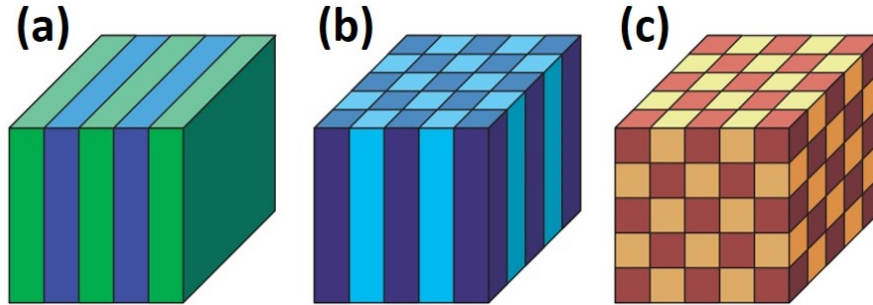
Figure 2.2: Illustration showing periodicity in (a) one, (b) two and (c) three dimensions.

them must be comparable to wavelength of light they are to be operated with. The QDs used throughout the work in this thesis generally emit between 880-930nm, as such, a lattice constant of around 230nm is used. Advanced fabrication techniques, such as electron beam lithography (EBL) are needed (see section 3.3.2). By removing certain holes from a photonic crystal with a triangular lattice of air-holes, it is possible to create structures that can confine and/or guide light. For example an H1 cavity is formed by removing a single hole from a photonic crystal and a W1 waveguide is formed by removing an entire row of holes.

2.8   Waveguides

Semiconductor waveguides are used to confine and guide light emitted from QDs. In the following chapters two types of waveguide are used. One is a suspended nanobeam waveguide and the second is called a W1 photonic crystal waveguide.
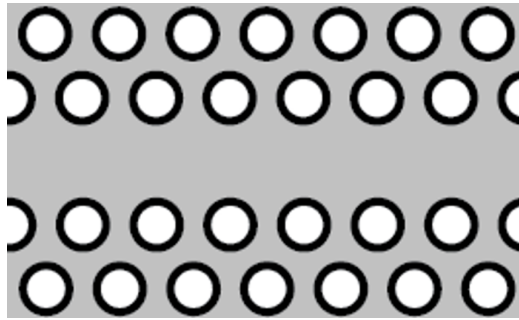
Figure 2.3: Schematic showing a W1 photonic crystal waveguide. The waveguide is formed by removing a single row of holes in a triangular lattice.

2.8.1   Nanobeams

Suspended nanobeam waveguides have a rectangular cross-section and are air-clad on all sides. Confinement is provided by TIR as discussed in section 2.4.1. The width and height chosen for the the waveguide ensure that the waveguide supports a single mode around the wavelengths of typical QD emission. SEM images of typical nanobeam waveguides are presented in figures 4.1, 5.1 and 6.1.

2.8.2   W1 Waveguide

A W1 waveguide is made by omitting a single row from a triangular lattice of air holes in a dielectric slab. This creates defect states in the photonic band gap; which can allow the propagation of certain optical modes along the defect axis. Figure 2.3. shows a schematic of a W1. By changing the design parameters of a W1, it is possible to enhance the light-matter interation within the waveguide, by decreasing the group velocity of the light. This is known as the slow light regime.

2.9   Stokes parameters

The Stokes parameters are a set of 4 values that serve to describe the polarisation state of electromagnetic radiation. Here, they will be referred as I, Q, U and V, where I is the intensity, and Q, U and V are the degrees of linear, diagonal and circular polarisation respectively. The Stokes parameters are easily measured experimentally and provide an efficient way to analyse the internal field profiles of simulated structures. The Stokes parameters are given by:

$$I = |E_x|^2 + |E_y|^2 \tag{2.7}$$

$$Q = |E_x|^2 - |E_y|^2 \tag{2.8}$$

$$U = 2\mathbb{R}(E_x E_y^*) \tag{2.9}$$

$$V = -2\mathbb{I}(E_x E_y^*) \tag{2.10}$$

where $|E_x|$ and $|E_y|$ are orthogonal field components and $*$ denotes the complex conjugate.

Chapter 3

Methods

3.1   Introduction

This chapter details the computational and experimental methods used for studying the devices presented in following chapters. Firstly, the computational methods are presented. Simulations and modelling are used to aid in the design of samples, as well as giving ideas around the expected experimental outcomes. Next, sample fabrication methods will be presented. This includes an overview of quantum dot growth using molecular beam epitaxy (MBE) and the fabrication techniques used in the production of photonic structures and diodes. Finally, optical measurement techniques will be presented, as well as the cryogenic systems that were used to study the devices and perform experiments.

3.2   Computational Methods

All the devices presented in the following chapters were simulated using computational methods before they were fabricated. This enables the optimisation of devices before fabrication takes place. Two of the main methods used in this thesis are: finite-difference time-domain (FDTD), which allows the temporal study of nanophotonic devices, and a frequency-domain eigenmode solver, which computes eigenstates of Maxwell's equations for periodic dielectric structures.

3.3   Experimental Methods

This section describes the experimental methods used to fabricate, characterise and study the photonic structures presented in this thesis. First, MBE growth of a typical GaAs wafer containing a layer of randomly grown SAQDs is discussed before moving on to the lithographic techniques that produce photonic structures and diodes. Next comes the experimental optical measurements before finishing with the cryogenic systems used. For all the devices presented in this thesis the wafers were grown by Dr. Edmund Clarke and further processing was undertaken by Dr. Benjamin Royall and Dr. Deivis Vaitiekus.

3.3.1   Quantum Dot Growth

The wafers containing QDs are grown in an MBE reactor. A clean and epitaxy ready substrate is placed into the reactor and held in a high vacuum

reaction chamber (pressure below $1x10^{-10}$ mbar)[78]. Several effusion cells, each containing an ultra-pure solid element, such as indium or arsenic, is heated until the element sublimes. By opening and closing shutters surrounding the elements, tailored amounts of each element can enter the chamber and react on the surface of the substrate. The growth control is precise enough to deposit material with monolayer accuracy. Combining this with the ability to abruptly change the materials being deposited enables the fabrication of very precise structures. GaAs for example, can be grown by opening the shutters of Ga and As, this will cause the two molecular beams of atoms to react with one another on the surface of the substrate. The beams interact at the wafer surface due to the long mean free path of each atom. The wafer is heated and held at a high enough temperature so annealing can occur as this helps to minimise sample defects. High purity wafers containing very few defects[79] are produced using this technique.

The wafers produced for use in this work are GaAs. The QDs are grown using the SK growth method, which relies upon an instability in epitaxial growth, where due to a lattice mismatch the system seeks to reduce strain, known as the Asaro-Tiller-Grinfield instability[80, 81]. They are produced by depositing monolayers of InAs, layer by layer, until a critical thickness is reached. The critical thickness depends on several factors, such as strain and chemical potential. Once the critical thickness is reached, the system seeks to reduce strain by nucleating into islands, leaving a thin layer (the wetting layer) and 3D islands (QDs). The QDs are then capped with more GaAs to move the air-substrate interface further from the QDs; improving their optical quality by increasing the distance between them and dangling bonds.
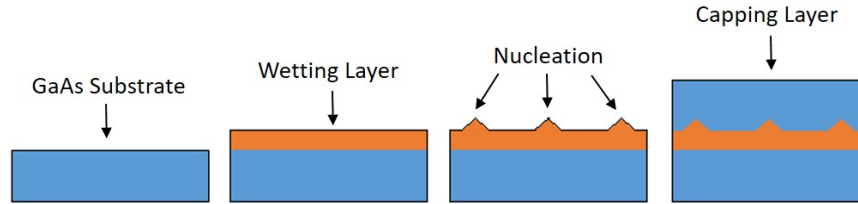
Figure 3.1: Diagram showing the Stranski-Krastanov (SK) method of QD growth. GaAs (InAs) is shown in blue (orange).

Dangling bonds can provide efficient non-radiative recombination pathways, leading to the quenching of QD emission[82]. See figure 3.1 for a schematic of SKQD growth.

3.3.2   Device Fabrication

Photonic structures have features on the order of the wavelength of light. Fabrication is done using electron beam lithography (EBL) and etching. Firstly the sample wafer is cleaned to remove any surface contaminants, and the surface treated with an adhesion promoter. Next a resist (ZEP520A) is spun onto the wafer surface. The resist is then hardened by baking it. ZEP520A is a positive resist which means that regions exposed will become more soluble in a developer.

A computer aided design package is then used to design the photonic structures to be etched. The pattern is then transferred to the resist as follows. Select regions of the resist are exposed to a scanning electron beam. The resist is then developed in xylene, leaving a mask to be used during etching. Regions of the resist patterned by the electron beam will be removed.

The resist pattern can then be transferred to the wafer by an inductively coupled plasma (ICP) etch. ICP etching is able to produce features very close to the patterned dimensions due to highly anisotropic etching[83], whereby the vertical etching occurs at a much higher rate than the lateral etching. Once the etch is complete the resist is removed. See figure 3.4 for a pictorial schematic of the fabrication process.

All wafers used in the production of samples used in this thesis have a sacrificial layer of $Al_{0.6}Ga_{0.4}As$. See figure 3.2 for a cross sectional diagram of the wafer structure used to make samples. This sacrificial layer is etched away using hydrofluoric acid to leave free standing photonic structures. The difference between the etch rates of AlGaAs and $Al_{0.6}Ga_{0.4}As$ can be as great as $10^5 : 1$. So removing up to 2μm of sacraficial layer should result in no more than 1nm of the photonic structure being removed.

Once the samples are under-etched they need to go through a process of critical point drying using supercritical CO_2[84], see figure 3.3. This is done because structures can be pulled and even broken, because of surface tensions, during the drying process. To avoid this acetone is used to remove any water from the sample. The sample is then held under high pressure and liquid CO_2 is added to remove the acetone. The temperature and pressure are increased to turn the CO_2 supercritical as a supercritical liquid has no surface tension so the samples should not be pulled by it during drying. The pressure is then lowered allowing the liquid to transition into a gas leaving a dry sample. See figure 3.3 for a pictorial schematic of how critical point drying is preformed.
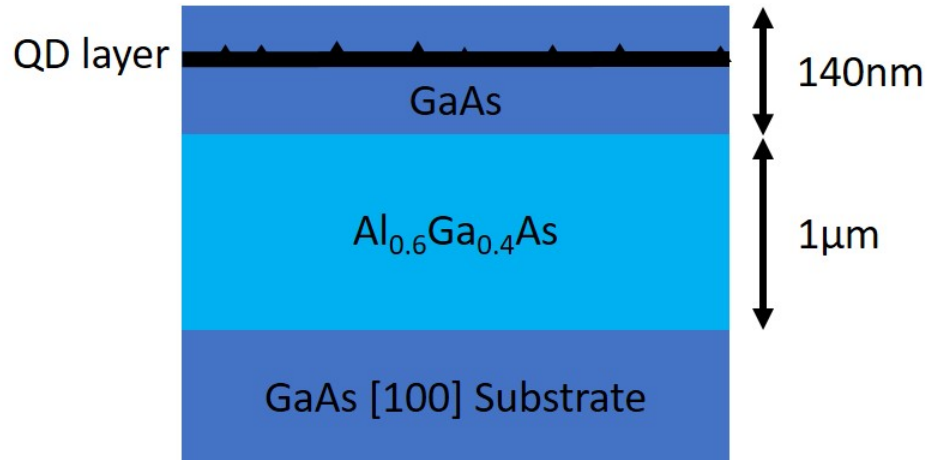
Figure 3.2: Diagram showing the typical structure of the wafers used to make samples. The middle section (light blue) is underetched to leave free standing structures. The QD layer is in the centre plane of the top section.

3.3.3   Diode Fabrication

By fabricating photonic devices on diodes, it is possible to apply an electric field across the sample, and use the QCSE to tune the emission energies of QDs (see chapter 7). For diode samples, the wafer structure is modified to include a doped layer grown above and below the QD layer. This provides barriers that stop tunneling out of the active region. The process of diode fabrication can be explained in 5 steps. Firstly, The sample is spin coated with SPR350 photoresist to create a layer approximately 1 μm thick in the centre of the sample. Thin films produced like these have a fluctuating thickness, and often need excess material on the edges removing before fabrication can continue. Once the photoresist is applied, it is baked at 90^oC for $60s$, this has the effect of setting the resist and making in resistant to some solvents.
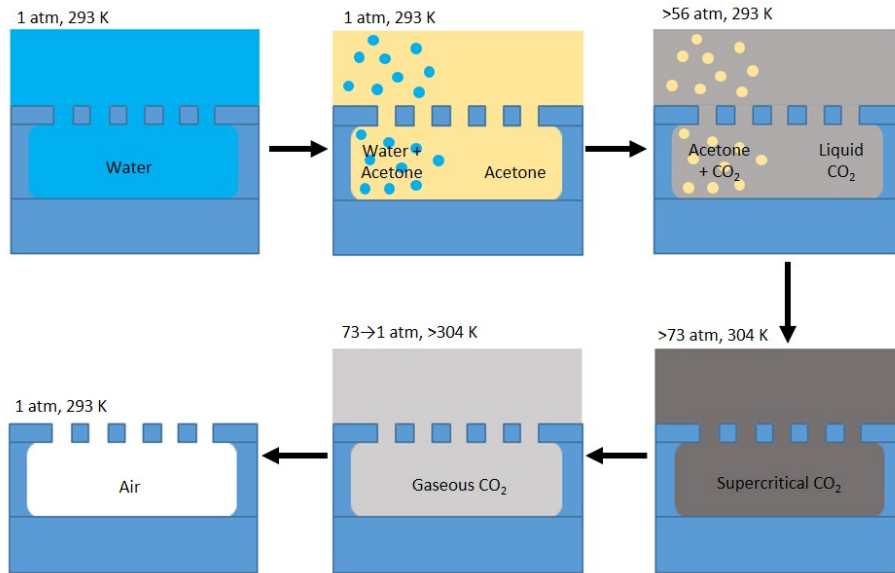
Figure 3.3: Schematic showing the stages of critical point drying. A sample immersed in water is purged with acetone. The chamber is then pressurised and liquid CO^2 is added. The chamber conditions are changed to cause the CO^2 to become supercritical. By then dropping the pressure the CO^2 becomes gaseous, leaving a dry sample.
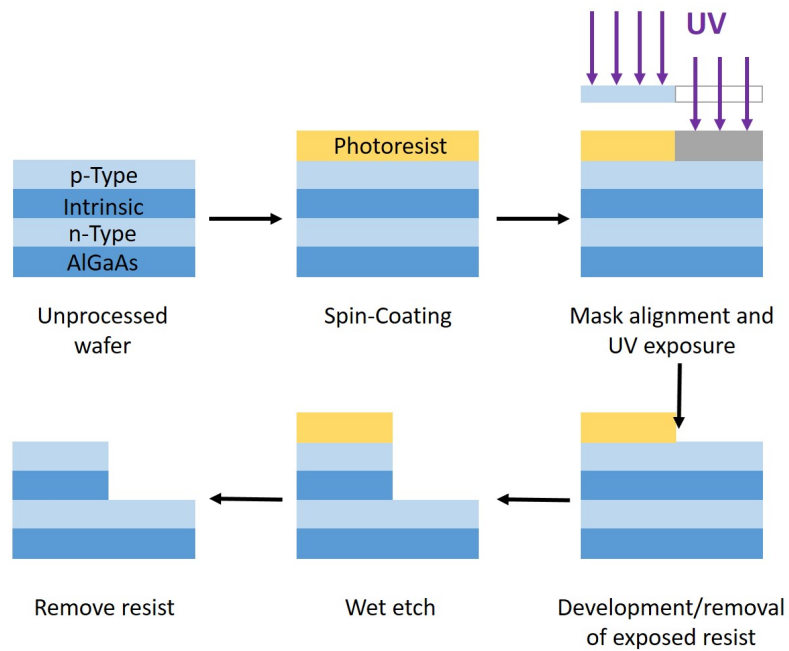
Figure 3.4: Schematic showing the stages involved in diode fabrication. A layer of photoresist is spin-coated onto the sample. The sample is exposed to UV light in a mask aligner. The resist is then developed, removingthe exposed areas. A wet etch is perfomed to reach the n-type layer before finally the photoresist is removed with acetone.

Next, the sample is placed in a mask aligner where selective parts of the resist are exposed to UV light. SPR350 is a positive photo resist, which means the the exposed regions will be removed duing development. The parts of the resist that have been exposed can then be removed by developing the resist in MF26a for approximately 1 min. Next, the sample is then wet using sulphuric acid or phosphoric acid. The etch depth can be checked using a Dektak stylus profiler system, and finally the photoresist can be removed using acetone.

Once the mesa structure is complete a similar process is used to add n-type and p-type contacts to the diode. For the p-type layer usually a Ti/Au contact is used with thicknesses ranging for 20 to 200nm and the n-type contact is usually Ni/Ge/Au with thickness ranging between 5 and 200nm. The sample is then cleaned and wired up for use.

3.3.4 Microphotoluminescence Spectroscopy

By exciting QDs either optically or electronically, they can be made to luminesce. This happens when an electron and hole are in a bound state and recombine to emit a photon. Under electrical excitation, electro-luminescence (EL) happens due to electrons and holes being injected from the n- and p-type contacts by the electric field.

Optical excitation has three distinct excitation regimes; Non-resonant, quasi-resonant and resonant. Non-resonant excitation is where the incoming excitation photon has an energy equal to or greater than the wetting layer bandgap. Depending on the energy and dynamics of the system, the electron hole pair may recombine optically at an energy equal to either the bandgap
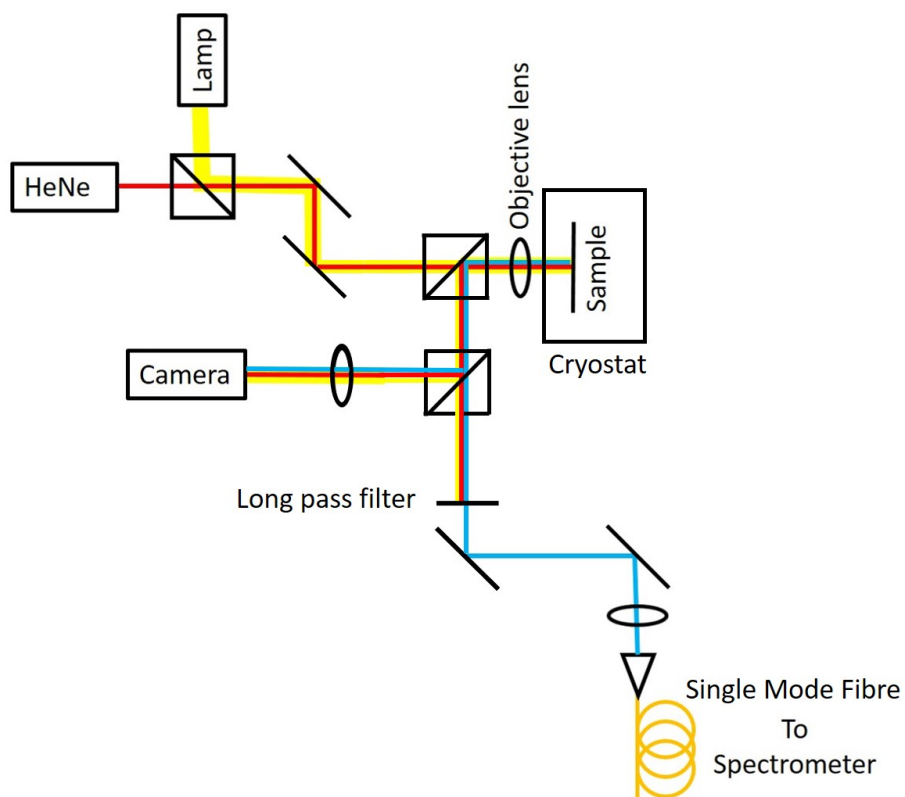
Figure 3.5: Schematic showing the optical apparatus used with the continuous flow cryostat to perform experimental measurments. A Helium Neon laser is used to excite the sample through an objective lens and signal is collected from the same position. The signal is filtered and sent to a spectromenter.
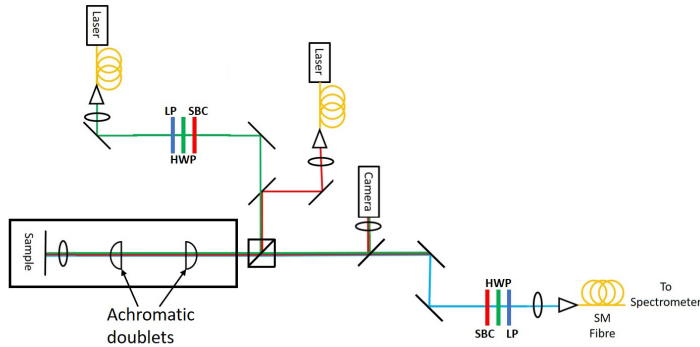
Figure 3.6: Schematic showing the optical apparatus used with the bath cryostat to perform experimental measurments. There are two independently positionable excitation paths. The collection path for the signal is also independent. Meaning spatially seperate regions for excitation and signal collection is possible.

of GaAs or the bandgap of the wetting later, or may be captured by a QD. Any relaxation/scattering processes that occur remove any coherence with the excitation photons.

In quasi-resonant excitation the excitation photon has an energy equal to either a p-shell state[85] or a longitudinal optical (LO) phonon-assisted state[86, 29]. When exciting with p-shell excitation a polaron state is generated which quickly decays into the s-shell within tens of picoseconds[87, 88]. LO phonon excitation will excite the QD transition and generate an LO phonon.

Resonant excitation or fluorescence (RF) is performed on resonance with the QD transition and directly excites the ground state transition at the Rabi frequency.[89, 90]. Resonant excitation is challenging due to the excitation and emitted photons having the same energy which makes filtering spectroscopically difficult. Methods have been developed to help distinguish

between the two types of photons. Polarisation control is one method of seperating the excitation photons from the emitted photons.

3.3.5   Photoluminescence Excitation Spectroscopy

Photoluminescence excitation (PLE) spectroscopy measurements are performed by measuring the PL signal, as a function of excitation energy. By tuning through a range of energies it is possible to probe the internal electronic structure of QDs[91, 92, 93]. A PLE measurement is usually required for each individual dot as variations in size, shape, and the surrounding environment vary from dot to dot. Once the internal structure of a QD is known, it is then possible to excite the QD quasi-resonantly using p-shell or LO phonon-assisted states. A PLE spectrum used to find resonances for a QD embedded within a nanobeam waveguide is shown in fig. 5.4. Diagrams showing the optics used in the continuous flow cryostat and bath cryostat setup are shown in figures 3.5 and 3.6 respectively.

3.3.6   Polarisation control

The polarisation of the excitation field was controlled via use of a linear polariser and quater waveplate. A variable waveplate was used to account for any birefringence in the system. The ability to excite with any arbitrary polarisation enables the response of the sytem under different polarisations to be studied. It has also proved useful for resonant experiments, where it is impossible to differentiate spectrally between excitation photons and QD photons, and so by cross polarising the excitation and detection arms any scattered laser signal can be minimised.
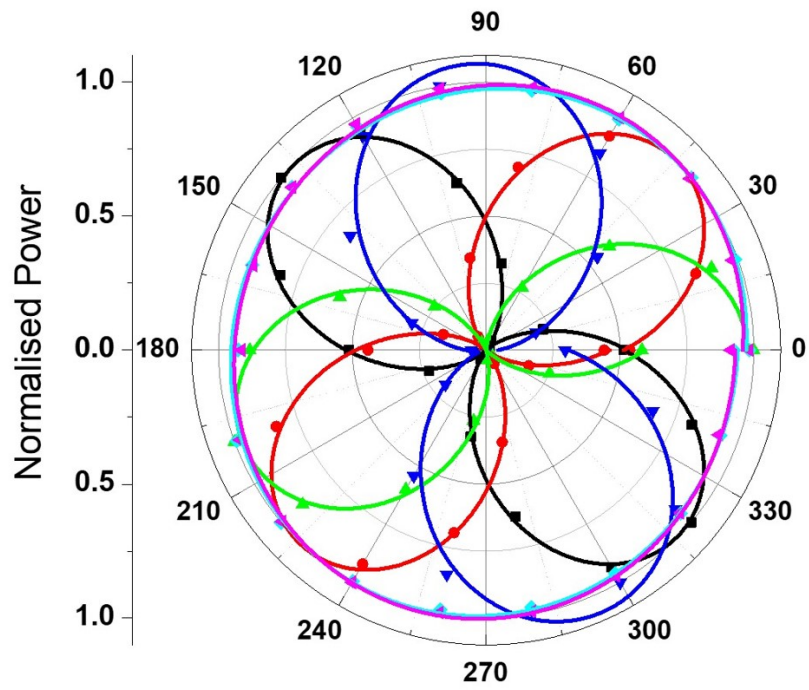
Figure 3.7: Polar plot showing different polarisations, linear and circular, which can be generated experimentally using waveplates.

Figure 3.7 shows how changing the angle of a linear polariser with the addition of a quarter waveplate can produce any arbitrary linear or circular polarisation. The polarisations are matched to the waveguide geometries. The linear polarisations are co- and cross polarised with the terminating Bragg couplers (black and red) and the diagonal polarisations are at 45° to these (green and blue). The circular polarisations are σ^+ (cyan) and σ^- (magenta).

3.3.7   Time-Correlated measurements

This section details the time-correlation measurements performed on QDs embedded with nanophotonic waveguides.

Lifetime measurements

Lifetime measurements can be performed by exciting the QD transition with a pulsed laser and measuring the intensity decay over time. By using a photo-diode connected to the output of the laser as a reference signal, and recording the time the QD emits, the time difference between the laser pulse and the QD emission can be measured. This gives the QD lifetime. As this is a statistical process the measurement needs repeating several times. In an ideal two-level system the decay of the exciton should follow a single exponential. If there are non-radiative recombination paths or feeding processes then the decay may follow a double-exponential decay. The results of a typical QD lifetime measurement is shown in figure 3.8. This QD has a radiative lifetime of $\sim$0.95ns.
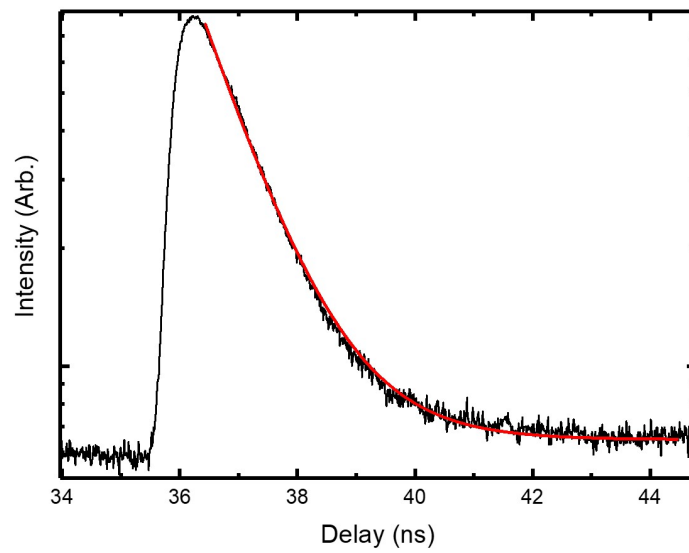
Figure 3.8: Example of a typical QD lifetime measurement. Experimental data is presented as a solid black line with the red line being an exponential fit to the data.

Hanbury Brown and Twiss

A second order correlation function or Hanbury, Brown and Twiss (HBT) measurment is a standard measurement in quantum optics that is used to verify the single photon nature of emitters. It was originally used to measure correlations between light detected from Sirius by two detectors six meters apart. The measurement proceeds by taking a light source, QDs in the case of this thesis, and passing the emission through a beam splitter towards one of two detectors. Any correlations between the two arms can then be measured.

In the case of a laser, where the emission follows Poissonian statistics (photons arriving at random intervals) there are no correlations in arrival time. In the case of thermal light, where $g^{(2)} > 1$, bunching occurs. This means there is increased probability in finding more than one photon in a short time window. Finally, there is sub-poissonian statistics, such as light emitted from a QD. This has a decreased probability of having one or more photons arriving in a short time interval. See Figure 3.9(a) which shows a simple schematic of the experiment and (b) which shows the results expected from bunched (blue trace), anti-bunched (red trace) and no correlations found from a coherent source.

3.3.8   Cryogenic Systems

All of the experimental work presented in this thesis were performed at a temperature of ∼5K. Samples were held in either a continuous flow or an exchange gas cryostat. The relative pros and cons of each system will be presented.
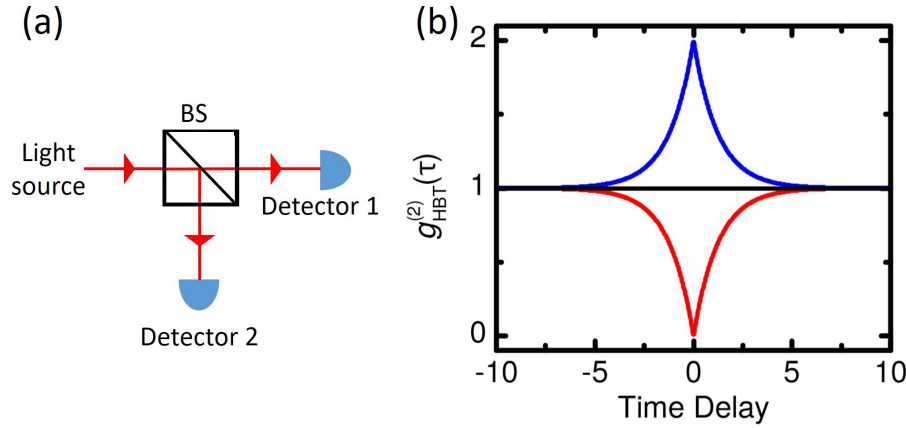
Figure 3.9: (a) Shows a schematic of how a typical HBT measurment is performed. (b) Example of potential HBT results where the blue, red and black traces show bunching, anti-bunching or poissonian statistics in the arrival times of detected photons.

Cold Finger Continuous Flow Cryostat

A continuous flow cryostat holds samples on a copper cold finger which is in thermal contact with a heat exchanger. Liquid helium is continually pumped through system to lower and maintain the temperature. The chamber where the sample is mounted is also placed under vacuum using a pump to evacuate the chamber so no contaminants condense on the sample during cooling. This type of cryostat usually holds samples at a higher temperature than a bath type cryostat due to its smaller size and also the sample is under high vacuum so heat transfer is provided by thermal contact with a copper coldfinger. Optical access to the samples is provided by a glass window on top of the cryostat.

The main advantage of a continuous flow cryostat is that it can be loaded,

cooled and unloaded relatively quickly compared to a bath type cryostat. As such, this type of cryostat is mainly used for quicker measurments, such as sample characterisation, where long term stability is not required. The optical apparatus is presented in figure 3.5. A helium neon (HeNe) laser is used to excite the sample. A 50x objective lens is placed above the sample to focus the laser light onto the sample. Sample movement is provided by a 3-axis homemade translation stage, which the cryostat is clamped to. Emission is collected through the same lens and is coupled to a single mode fibre and then sent to a spectrometer with a nitrogen cooled charge couple device (CCD). A lamp provides white light to illuminate the sample to aid moving around the samples, with the image from a camera displayed on a monitor. This type of cryostat is mainly used for quicker measurements, such as sample characterisation, or where sample stability is not a primary concern. The optics used with this cryostat is presented in figure 3.5

Liquid Helium Bath Cryostat

A helium bath cryostat holds samples near the bottom of a tube that is submerged into liquid helium. Cooling happens via heat exchange with a small volume of helium gas inside the tube. As with the flow cryostat optical access is granted from a glass window at the top of the tube. Achromatic doublet lenses are used to increase the scanning range of the microscope.

The main advantage of this style of cryostat is that they are very stable. So it is used for longer measurements or where sample stability is paramount.

The optics used with this cryostat is presented in figure 3.6. Two independent excitation paths are available for exciting the samples. This enables

the excitation of two spatially seperate positions. Emission from the sample is then collected using a third optical path, which is individually positionable, and sent to a single mode fibre and on to a spectrometer and CCD.

3.4 Device Design

In the following chapter two waveguide designs were studied and compared; nanobeams and W1 photonic crystal waveguides. Both waveguides were under etched and so are air-clad on all sides. The waveguides are terminated by Bragg couplers, which allow for efficient in and out-coupling of light. Due to the SK growth of QDs within the samples, the QDs are randomly distributed throughout the device. Fig 3.10 (a) and (b) show SEM images of the two waveguide designs respectively. See section 2.8 for further details on the waveguide designs.

3.5 Experimental Arrangement

In this section the experimental arrangement will be presented. Details of sample growth and the devices fabricated on them (see sections 3.3.1 and 3.3.2) will be presented along with the method used for QD position registration. The experiments were performed in a 4K liquid helium bath cryostat. Two independent optical paths were used for exciting the samples and collecting any emission. An above bandgap laser was used to excite the QDs. The collection is mainly done at the terminating couplers. See section 3.3.8 figure 3.6 for more details. A magnetic field of up to 5T can be
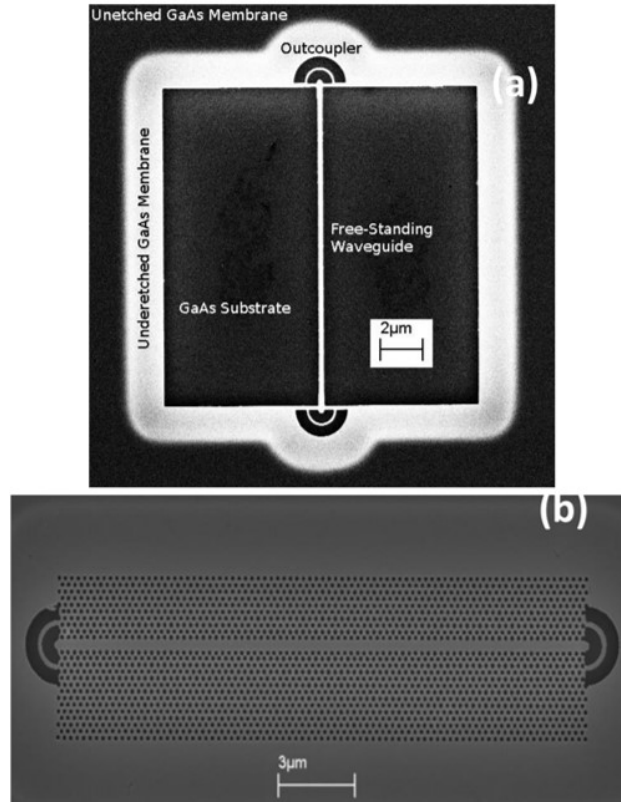
Figure 3.10: (a) SEM of a typical suspended nanobeam waveguide. (b) SEM of a typical W1 photonic waveguide. Both waveguides are terminated with Bragg outcouplers.

applied along the growth direction of the QDs. Positioning of the samples was achieved using a 3-axis piezo stage stack. Optical access was through a confocal microscopy[94] setup. The spot sizes on the excitation and collection paths were below $1.5\mu m$ in diameter and had travel range of more than $15\mu m$ using scanning mirrors to obtain the exact geometry required for each experiment. The PL signal was recorded using a single 0.75m spectrometer and liquid N2 cooled charge-coupled device (CCD) camera with resolution of

17μeV. For time-correlated single-photon counting measurements $g^{(2)}(\tau)$, the QD emission was filtered using the spectrometer, passed into a fibre beam splitter and detected by two avalanche photodiodes (APDs).

3.5.1 Sample Fabrication

The samples were fabricated using the method in section 3.3.2. The samples were grown by molecular beam epitaxy on an undoped [100] GaAs substrate, and consisted of a 140nm thick GaAs membrane with a layer of InGaAs SAQDs grown in the centre plane of the waveguides ($z = 0$), on a $1\mu m$ thick sacrificial $Al_{0.6}Ga_{0.4}As$ layer. The suspended nanobeams were $15\mu m$ long, 280nm wide and 140nm high. The W1 waveguides were designed to have lattice constant $a = 254nm$ and hole radius $r = 0.31a$. All waveguides were terminated with Bragg couplers.

3.5.2 QD Position Registration

To verify the results presented in the following section, a selection of QDs were selected and their positions registered so they could be deterministically positioned with the waveguides. QD registration is carried out in a scanning micro-PL set-up with two collection paths. The process of registration involves three steps. Firstly, pre-registration markers are fabricated on the sample. Then the positions of QDs are determined relative to the markers. Finally, photonic strucures are fabricated around the QDs determining their positions inside the structures. Figure 3.11 shows the main steps in QD position registration. Many thanks to James Dixon who conducted nearly all of the registration work.
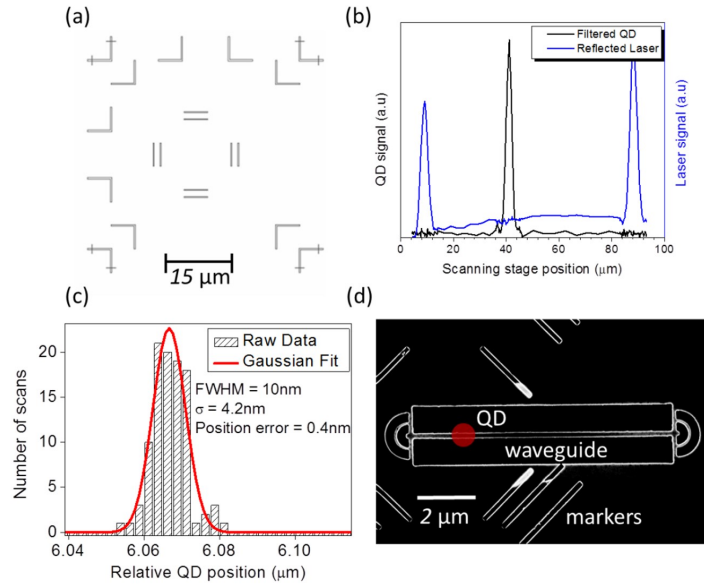
Figure 3.11: (a) Shows a design of markers that were patterned or etched into the surface. Using these relative QD positions could be determined. (b) Spectra where the blue trace shows signal reflected from the markers and the black trace shows the QD position. This type of scan is performed many times and along two orthogonal axis. (c) Shows a histogram of QD position scans. (d) shows an SEM image of a waveguide after QD registration has taken place. The position of the QD is highlighted in red.

Chapter 4

Chirality of nonophotonic waveguide with embedded quantum emitter for unidirectional spin transfer

4.1   Introduction

Controlling the flow of light, and henceforth data, around a photonic circuit is a current active area of research in physics. Using photonic chips with embedded quantum emitters and optical components provides a promising platform for QIP tasks. This type of architecture helps solve the miniaturisation problem, as quantum optical elements can be integrated onto photonic chips/circuits and waveguides[9]. Scaling this platform should also be possible due to advanced fabrication techniques; and with recent developments of

43

passive and active components[95] on-chip, such as beam-splitters.

By tailoring the photonic environment surrounding quantum emitters, not only can phenomena such as Purcell enhancement be observed, but other emission properties, such as directional emission can also arise. Connecting static qubit nodes (QDs) with flying qubits (photons) enables distributed quantum computing[16] and may facilitate the quantum internet[17], which will require high-fidelity conversion between the two, to store and transfer information[96, 20, 97]. The spin of an electron or hole has potential to store information (spin state) in a quantum network, but a method is needed to reliably map the spin state of a QD to quantity that is directly measurable. The coupling of a QDs spin to the direction of photon emission in a nanophotonic waveguide offers a possible solution. The first reports of unidirectional propagation of electromagnetic radiation, in engineered nanostructures first appeared appeared in 2013, where surface plasmons[98] and atomic dipoles[99] were excited by circularly polarized light, and changing the handedness of the light changed the propagation direction of the emitted photons. This chiral effect manifests in these systems due to the coupling of the emitter with the evanescent field of the photonic nanostructure. The evanescent field has longitudinal components which enable circularly polarized states to propagate, with the field rotating within the longitudinal plane defined by the photonic structure[100, 101, 102, 103]. The first report of directional emission from a quantum-emitter embedded within a photonic structure was in a cross-waveguide structure[104], since then directional emission has been observed using a specially engineered glide-plane waveguide[105], which confirms theoretical predictions for directional emission in PhC WGs[106].

In this chapter, directional emission from a QD embedded within a nanophotonic waveguide is presented. Using embedded QDs as probes allows the demonstration that the internal electromagnetic field in photonic waveguides is intrinsically chiral. This may at first be surprising as the system posses inversion symmetry and the dielectric material that it is produced from is non-chiral. The importance of the position of the emitter within the waveguide is shown, as anything from totally symmetric emission up to complete unidirectional emission can occur, depending on the emitter's location. Due to the strict spin selection rules for a QD exciton; efficient coupling between the QD exciton spin and the direction of photon propagation is achieved in these systems.

Theory and simulations give a good understanding of how the phenomenon of directional emission arises in this system; by comparing different waveguides, nanobeam and W1 (see chapter 2 section 2.8), comments on the strengths and weaknesses of each system are drawn. Simulations are also used in conjunction with experimental work. Suspended nanobeam and W1 waveguides were investigated experimentally with randomly distributed QDs. Emitters located in the centre of waveguides will show non-chiral emission. However, by displacing the position of a QD laterally by 32% of the waveguide width, maximum chiral emission is observed. Using this understanding enabled the deterministic positioning of QDs within nanobeam waveguides. Using a QD position registration technique[107, 108], it was possible to deterministically position the QDs within waveguides and achieve directional dependent readout by design.

4.2   Theory and Simulations

4.2.1   Directional emission in Nanobeam waveguides

Unidirectional emission arises due to the distribution of the internal electromagnetic field within the laterally confined nanophotonic waveguide. The confinement of EM-radiation within the waveguides modifies the field components from the case of EM-radiation propagating in free space. A longitudinal component of the electric field arises due to this confinement. Transverse (E_y) and longitudinal (E_x) field components have position dependent amplitudes and as such the waveguides can support elliptical polarisations.
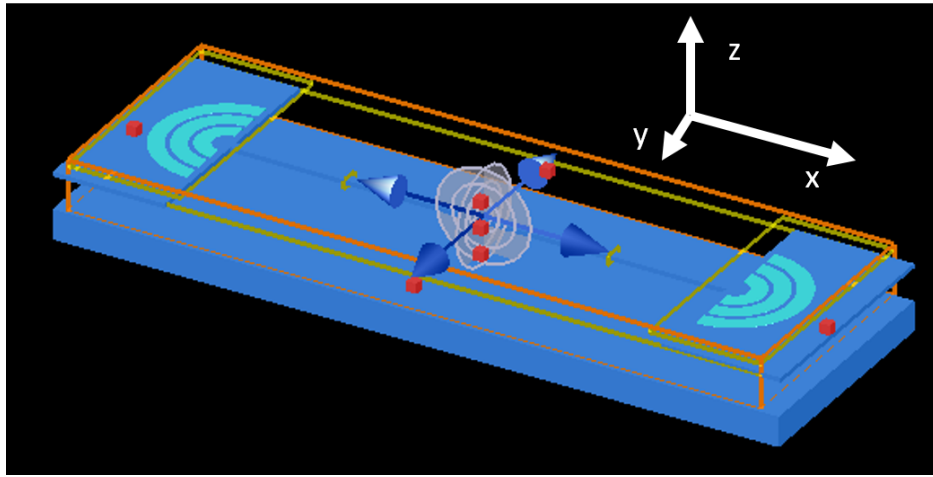
Figure 4.1: Image of a suspended nanobeam created in Lumerical.

The field profile of the waveguide was calculated using an eigenmode solver (MPB). Figure 4.2 shows the amplitudes of the electric field components (E_x and E_y) of the waveguide as well as the phase difference between them as a function of lateral displacement from the centre. The $|E_y|$ com-
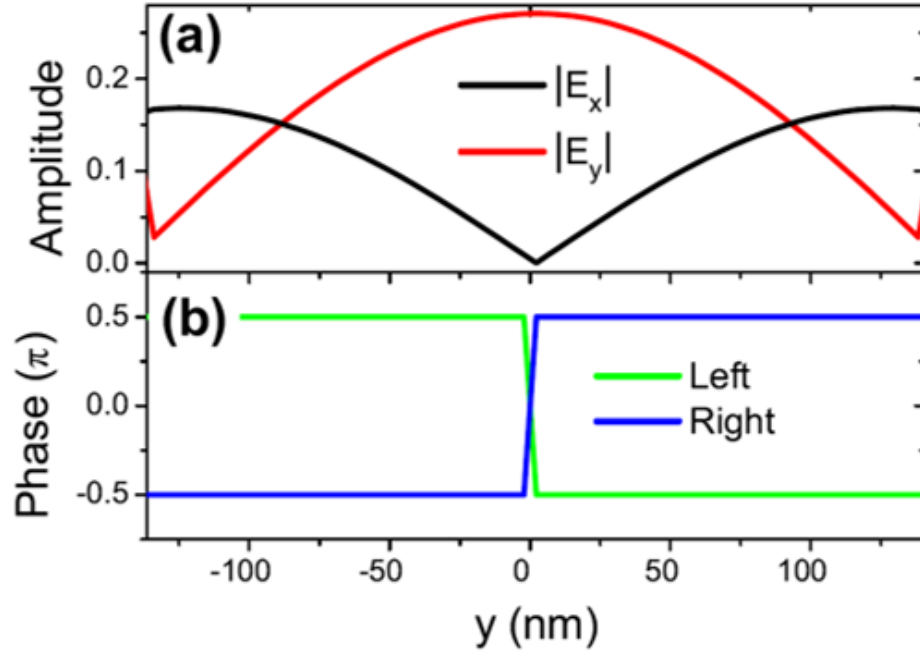
Figure 4.2: (a) Electric field amplitudes as a function of lateral position. (b) Phase difference between the field components as a function of lateral position and propagation direction.

ponent has a field maximum in the centre of the waveguide, and the $|E_x|$ component has two maxima near the edges of the waveguide. The relative phase between the two components is $\pm\frac{\pi}{2}$ with the sign changing as $y = 0$ is crossed. The asymmetry in the phase allows chiral behaviour as the waveguides can support regions of circular polarisation, which occur where $|E_x| = |E_y|$, the phase difference is $\pm\frac{\pi}{2}$ and they occur at a lateral displacement of $\sim$90nm. The chiral points are positions within the waveguide where the field is circularly polarised, as the field rotates in time during propagation of the mode, and the helicity depends on the propagation direction as

shown if Fig. 4.2(b), and the $\sigma^{\pm}$ components couple to modes propagating in opposite directions.

Simulations of the nanobeam waveguides with dipole sources placed in the z=0 plane (centre plane of waveguide) were performed to see how the position of the emitter influences its emission properties as well as polarisation and wavelength of the emission. Simulations were performed using Lumerical[109], a premium Finite Difference Time Domain simulation package, and MPB[110], a freely avaliable frequency domain eigenvalue solver. Firstly, an infinitely long nanobeam waveguide was simulated as computationally this was the simplest starting point. Fig 4.1 shows an example of a waveguide created in the simulation package.

Simulating a dipole source in a waveguide

When simulating the dipole sources two polarisations were used; linear and circular. The linearly polarised dipole showed no dependence on position within the waveguide, as in simulations the dipole emission always coupled equally to each propagation direction. The beta factor, which is the fraction of emitted light that couples to the waveguide mode over the entire emission into all modes, does vary based on the dipole position. The coupling efficiency of a circularly polarised dipole positioned at a chiral point was also simulated. The directional coupling efficiency is defined as the fraction of the emitters power that is directed along a single propagation direction within the waveguide, and is calculated to be 68%. This is an increase of ∼2.8 times greater than for a circular dipole positioned at the centre of the waveguide and ∼1.4 times greater than for a linearly polarised dipole in the centre of

the waveguide. So positioning a circularly polarised emitter at a chiral point should offer greater coupling efficiencies compared to emitters in the centre of the waveguide.

By changing the position of a circularly polarised dipole, displacing it laterally from the centre of the waveguide, it was found that the power transmitted along each arm of the waveguide was not equal. In the centre of the waveguide, any dipole polarisation will be symmetrically coupled, as the field at this point is linearly polarised transverse to the waveguide axis. By displacing the dipoles laterally from the centre of the waveguide; varying degrees of unidirectional emission was observed. By using a broadband source (900-1000nm) and simulating many positions, it was possible to see how displacement and wavelength affects the directional emission. Fig 4.3 shows the results from these simulations.

Directional emission in an infinite waveguide

Figure 4.3 shows the degree of unidirectional emission as a function of emitter displacement and emission wavelength. The power that propagates along each arm of the waveguide was recorded, see figure 4.2 for an illustration of a simulated waveguide with an internally located dipole, where a value of 0 corresponds to equal power being transmitted along each waveguide arm and 1 showing the complete unidirectional transmission of the emitted power from the dipole. The degree of unidirectional emission is largely independent of the emission wavelength; with almost complete unidirectional emission being predicted by the simulations at a displacement of around 90nm. The scale in figure 4.4 runs from 0 (symmetric coupling) to 1 (unidirectional emission).
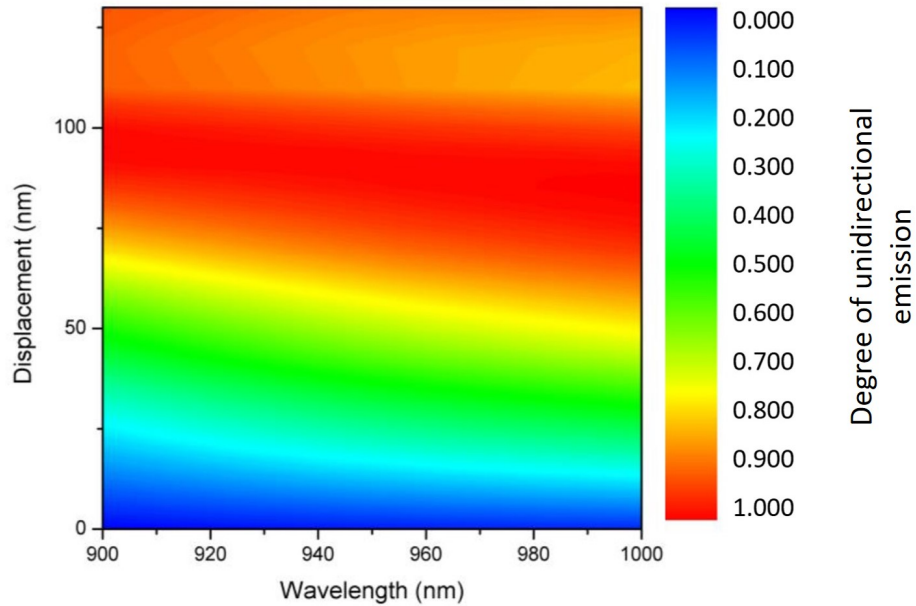
Figure 4.3: Degree of unidirectional emission for a circular dipole in an infinite nanobeam waveguide as a function of lateral displacement and emission wavelength.

Directional emission in a finite waveguide

Bragg couplers [111] [112] were added to terminate the ends of the waveguides. Simulations of the waveguide with the bragg couplers were modified from the infinite case, see fig 4.4, to see how this will influence the system compared to the infinite case. The bragg couplers form a weak cavity due to reflections and Fabry-Perot type fringes are observed in simulations. As can be seen in Fig 4.4; there are now areas where high directionality can be observed at lower displacement, but these now become more sensitive to the wavelength of the emission. The highest unidirectional emission and least sensitive to wavelength and displacement for the emitter is still around

90nm.
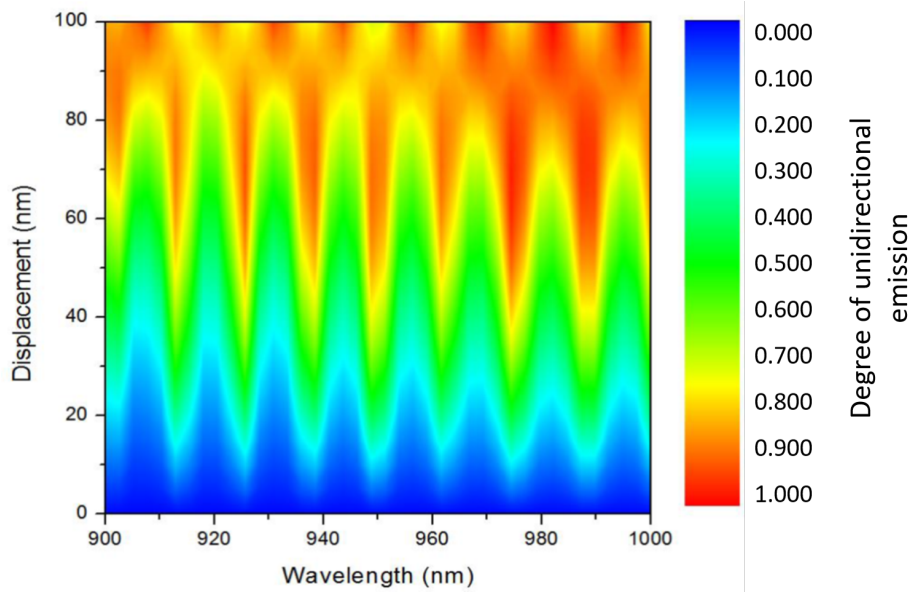
Figure 4.4: Degree of unidirectional emission for a circular dipole in a finite nanobeam waveguide as a function of lateral displacement and emission wavelength.

Video monitors, which record the electric field amplitudes over time, were used in the simulations to produce movies showing how the EM-radiation propagates through the devices. Figure 4.5 shows the emission of a circularly polarised dipole positioned at the centre (left side panels) and at a chiral point (right side panels). The Top panels show the radiation a short time after dipole emission and the bottom shows some of the radiation being reflected from the out-couplers. The arrows show the direction the emitted radiation propagates. The dipole is in the centre couples equally to both directions, emitting equal power along each waveguide arm, so no chiral emission is observed. The right panel shows a circularly polarised emitter at a

displacement of 95nm. As can be seen in this panel most of the power, $\sim 99\%$ of the confined light, is directed towards the right, with $\sim 1\%$ propagating to the left. Reflections from the Bragg couplers can also be observed (bottom panel) where the left (right) is symmetrically (chirally) coupled to the waveguide mode. Reflections will lower the contrast observed in experiment, as the stronger component will have the most reflected signal, which in turn propagates back along the waveguide and contributes to the signal at the other side of the waveguide.

4.2.2   Electric field distributions in photonic waveguides

Infinite Nanobeam

Another way of looking at the internal electric field of the waveguide is to use the Stokes' parameters. These describe the polarization state of electromagnetic radiation (See section 2.9). A mode source was used to inject a wavepacket into the fundamental mode of the waveguide and the electric field components were recorded. From this, plots showing the position dependent internal polarisation of the waveguide were produced. Fig 4.6 shows the degree of circular polarisation as a function of position within the waveguide. An emitter placed within the waveguide will couple differently to the waveguide modes depending on where it is located. Due to the simulated waveguide being infinite, there is continous translational symmetry along the x-axis, with polarisation varying with lateral displacement. It is again observed that the highest degree of circular polarisation occurs at ± 90nm. See figure 4.6.
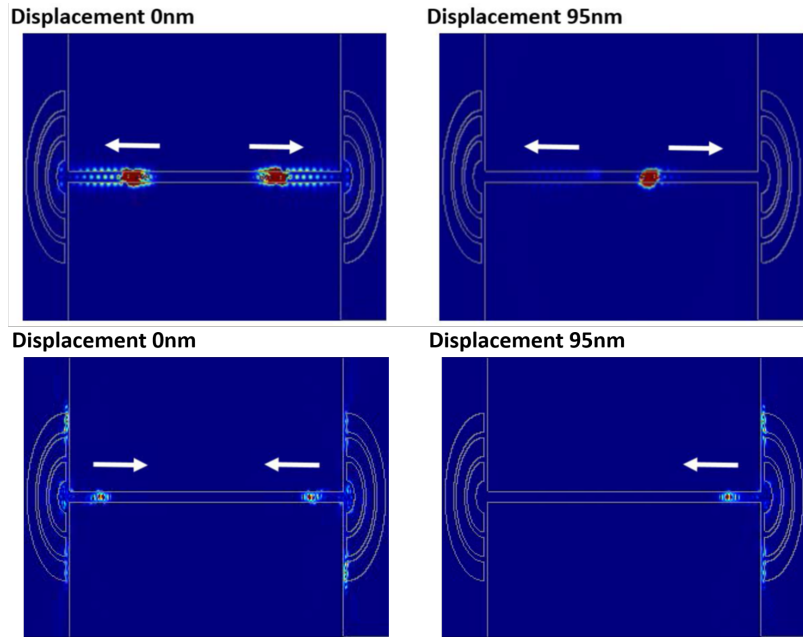
Figure 4.5: Still images taken from a simulation movie monitor showing the electric field amplitudes over time. The top row is taken shortly after dipole emission and the bottom row shows some of the emission travelling back along the waveguide after reflecting off the out-couplers; with the direction of the emission given by the white arrows. The left (right) column shows a symmetrically- (chirally-) coupled QD exciton.

Finite Nanobeam

Similarly to figure 4.4, the infinite case in figure 4.2 was modified to include terminating couplers at either end of the waveguide. In moving from the infinite case to the finite one, Fabry-Perot type oscillations occur, which is due to back reflections from the couplers. This makes the position of the emitter sensitive to its x-axis position. This has the result of modulating the field distribution. The chiral mechanism remains unchanged, however, the
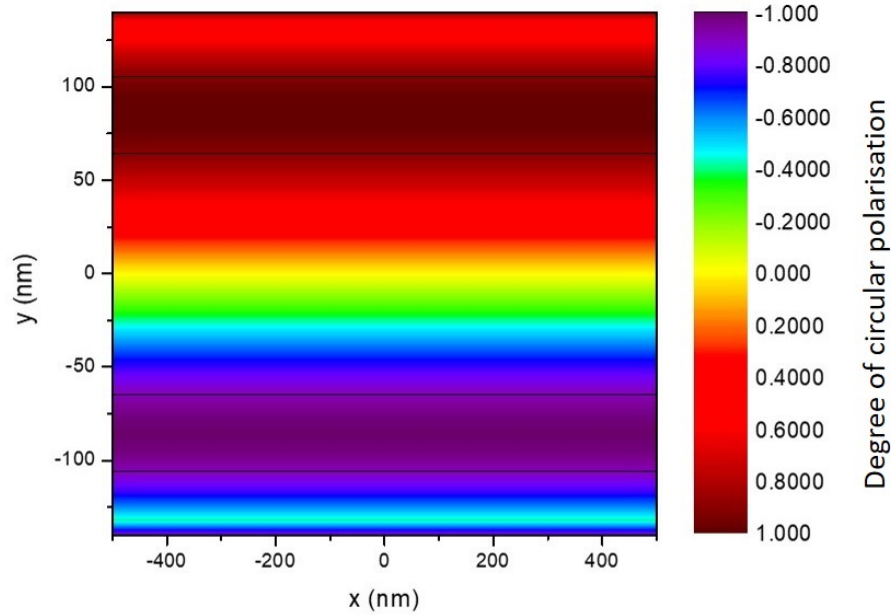
Figure 4.6: Degree of circular polarisation of the local electric field within an infinite nanobeam waveguide as a function of position within the waveguide. Where the values of ±1 correspond to complete circular polarisation and a value of 0 corresponds to linear polarisation.

contrast is reduced due to these reflections. The probability of finding a QD exciton with high contrasts exceeding 90% is reduced by ∼52%. See fig. 4.7.

W1 Photonic crystal waveguide

A standard photonic W1 waveguide was also simulated, see figure 3.10(b). Fig 4.8 shows a section of a W1 and the degree of circular polarisation. When comparing the chiral areas of the nanobeam and W1 waveguides, the nanobeams have much larger chiral areas. This means the chances of finding a
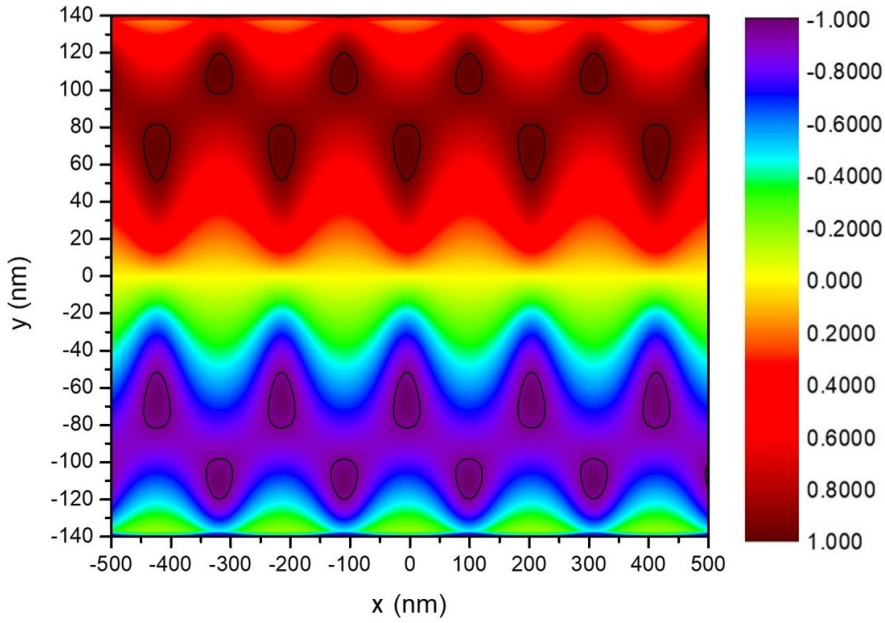
Figure 4.7: Degree of circular polarisation of the internal electric field as a function of position within a finite nanobeam waveguide. Where the values of ±1 correspond to complete circular polarisation and a value of 0 corresponds to linear polarisation.

highly chirally-coupled QD is higher in this design of waveguide. Simulations show the area within a nanobeam waveguide with contrast exceeding 90% is 14%, whereas in the W1 the area exhibiting contrasts 90% is ~ 0.8%. When looking at chiral areas with contrasts above 80%, a nanobeam has 34% of its area exhibiting high contrasts and a W1 has ~ 1.5%, (see figures 4.7 and 4.8). The chiral points in W1 waveguides also correspond to areas of low field intensity, which leads to poor dipole coupling to the waveguide modes. The highly chiral areas of the W1s, which are ~20 times smaller than the nanobeams, coupled with the low field intensities show the advantages of
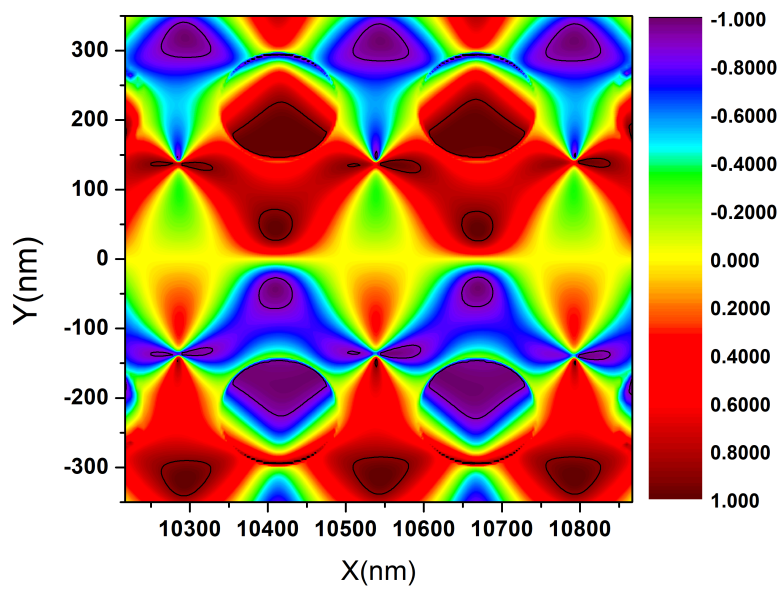
Figure 4.8: Degree of circular polarisation of the internal electric field as a function of position within a W1 photonic crystal waveguide. Where the values of ± 1 correspond to complete circular polarisation and a value of 0 corresponds to linear polarisation.

using nanobeam waveguides over W1s for spin readout. The near continuous translational symmetry of the nanobeams, compared to W1s, means the positioning of the QD is not as restrictive. Photonic crystal waveguides may provide additional benefits as they can take advantage of higher beta factors and slow light modes. Glide-plane techniques[105] may used to modify the waveguide design, by shifting one side of the waveguide by half a lattice constant as well as making other modifications, attempting to increase the amount of highly chiral areas.

4.3   Results

In this section the experimental spin readout results will be presented. The systems under investigation are suspended nanobeam and standard W1 waveguides (see section 4.2 for details), with embedded QDs. The QDs serve as internal quantum emitters with spin-exciton eigenstates coupling to modes propagating in opposite directions, leading to directional emission from the QD upon exciton recombination. As previously stated, nanophotonic waveguides have both transverse and longitudinal field components (E_x and E_y), and as will be shown, allow the transfer of in-plane circular polarisation ($E_x \pm iE_y$; see Fig. 4.1). A QD positioned at a c-point will emit circularly polarised photons along a single direction inside the waveguide, where the direction the emitted photon takes is dependent of the excited spin state of the exciton.

A schematic of the experimental geometry is given in Fig. 4.9(a). The left- and right-circularly polarised photons arise from recombination of up

and down exciton spin states from a QD embedded within the waveguide. With application of a magnetic field in the growth direction, the QD exciton spin states are Zeeman split, leading to the emission of circularly polarised photons, regardless of the excitonic species, see Fig. 4.9(b). The photons propagate along the waveguide and are diffracted by the terminating Bragg couplers to a spectrometer.
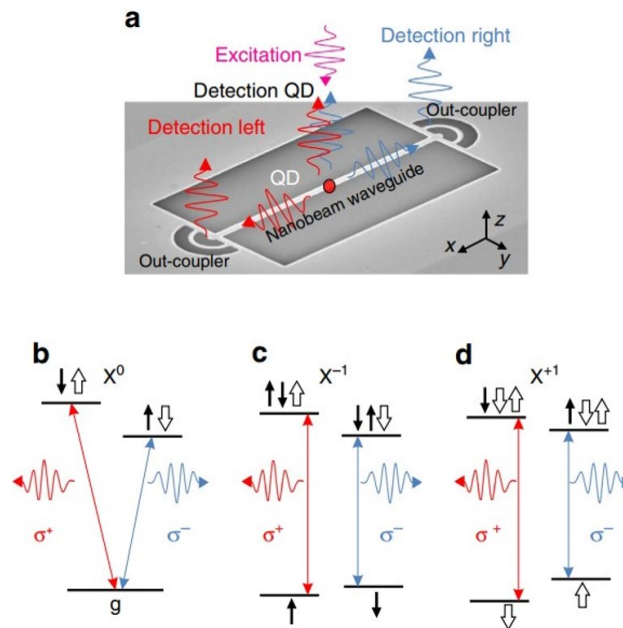
Figure 4.9: (a) Schematic showing the experimental setup used for spin readout. Excitation is shown in pink. Blue and red shows how a chirally coupled QD would emit. (b-d) Shows the selection rules for neutral and charged excitons.

Statistics from numerous QDs located in the suspended nanobeam and standard W1 waveguides will be presented and compared with each other as well as with the simulation results. A magnetic field dependence is also shown under non-resonant (above bandgap) and resonant excitation showing

how the contrast varies with field strength.

4.3.1 Spin Readout in photonic waveguides

As described in section 4.4, above bandgap excitation (808nm) was used to excite QDs which are randomly distributed throughout the waveguides. Emission from the QDs is collected from above the QD and from the terminating Bragg couplers. A magnetic field strength of 1T was applied in the growth (Faraday) direction to Zeeman split the QD transition components to create pure spin states, as well as for easy detection and identification (see fig 4.11). The degree of contrast in spin-readout (the directionality factor) is defined as:

$$C_{LEFT/RIGHT} = \frac{I_{\sigma+}^{L/R} - I_{\sigma-}^{L/R}}{I_{\sigma+}^{L/R} + I_{\sigma-}^{L/R}} \tag{4.1}$$

Where I is the intensity, L and R correspond to the left and right detection out-couplers and the subscripts, σ^+ and σ^-, indicate which Zeeman component.

Chirally coupled QD

Figure 4.10 (top panel) shows a spectrum measured from above a highly chirally-coupled QD. A magnetic field strength of 1T is applied in the growth (Faraday) geometry to Zeeman split the QD components. As can be seen the emission intensities of both components are approximately equal. The collection path was then moved from the QD and positioned above each of the terminating gratings and spectra recorded. The bottom panel shows

spectra taken from the left (green trace) and right (red trace) couplers. When collecting from the left, the higher energy Zeeman component is observed, and the lower energy component is not. The opposite is true when collecting from the right, a strong lower energy component is observed and a really weak higher energy component. This shows that the emission from the QD is directed along the waveguide, with the majority of the higher (lower) energy being mainly directed along the left (right) propagation mode of the waveguide. Contrast values, see equation 4.1, of $C = 0.95$ and $C = -0.88$ when collecting from the left and right out-couplers respectively are found. This shows the high fidelity of this system for mapping the spin state of an excited QD to the direction of the emitted photon upon recombination.

Symmetrically coupled (Non-chiral) QD

A symmetrically-coupled QD is one which couples equally to each propagation direction. QDs with low contrasts are referred to as symmetrically coupled as any chiral effects will be minimal due to the roughly equal coupling strengths. The emission couples equally to both arms of the waveguide meaning it could not be used to determine the original spin state or to convert spin to path. See fig. 4.11. Low contrast values of $C = 0.03$ and $C = 0.01$ are found when collecting from the left and right couplers respectively. The low contrast values show the QD exciton components couple equally to both directions within the waveguide.
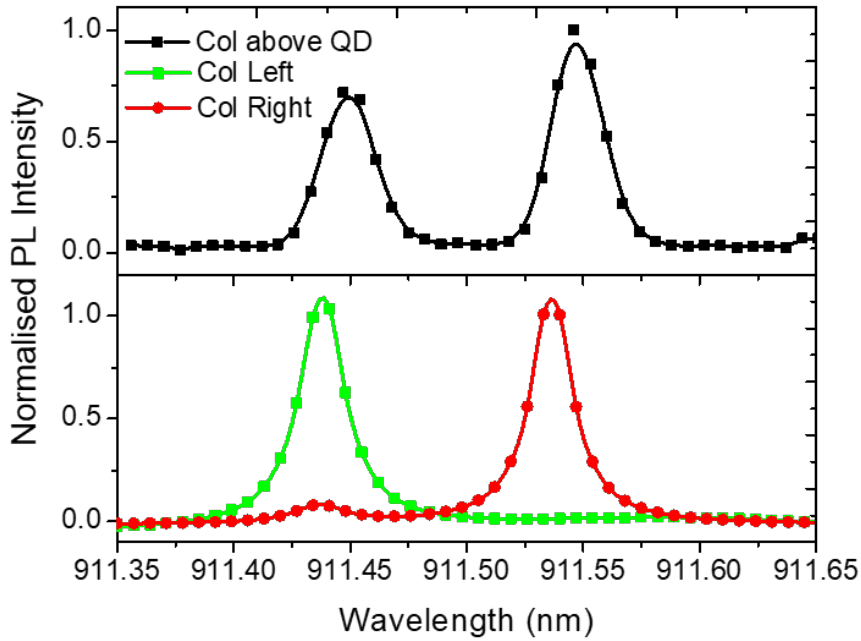
Figure 4.10: (a) shows a spectrum taken from above the QD. The signal is generally weaker when collecting from above the QD. (b) shows two spectra taken from opposite ends of the waveguide. The signal is stronger from the outcouplers and differences in the emission of each emitted component can be seen.

Nanobeam QD Statistics

Figure 4.12 shows the contrasts for 50 QDs embedded in nanobeam waveguides. The black trace shows expected contrasts for ideal circularly polarised dipoles. The scatter around the diagonal may arise due to asymmetrical back reflections from the terminating Bragg couplers, caused by fabrication defects. Also, the circular polarization for the QDs may also be affected in photonic structures by the nanostructure and surface proximity. The finite
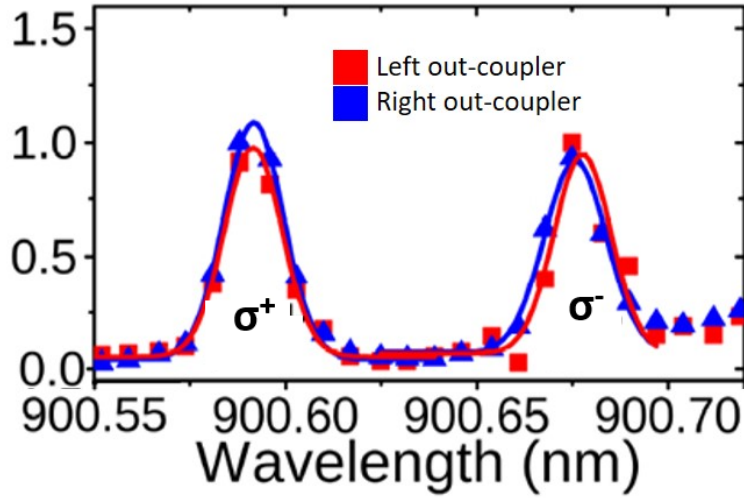
Figure 4.11: Spectra showing QD emission collected from the left (red trace) and right (blue trace) out-coupler. The intensities of each Zeeman split component are roughly equal regardless of which outcoupler they are viewed from.

size of the QD, which is known to cause a breakdown in the point dipole approximation used for the simulations in nanophotonic structures may also affect the contrast. From FDTD simulations, a QD placed at a c-point will have an out-of-plane scattering efficiency from the Bragg couplers of ∼39%, with ∼17% of the emission being reflected from the Bragg couplers, and the rest goes into modes not supported by the waveguide. This means for a single component measured from one coupler, ∼39% of the emission should be measured, neglecting losses in the detection apparatus, and ∼6.5% measured from the opposite coupler due to reflections back along the waveguide. Provided there is little variation in the quality between the two fabricated terminating couplers the back reflections should cause a reduction in measured contrast but not cause any asymmetry. Outcoupler dimensions can

vary by a few nanometers for a single device, but even so this effect is likely to be small. Elliptically polarised QDs will also reduce the measured contrasts. Asymmetric QD states may arise due to the fine structure splitting of the neutral exciton within the QD[113, 33] or piezoelectric effects[30] due to strain in the waveguide. Similar effects are observed in[114, 115, 116]. The insert of fig 4.12 shows a $g^{(2)}$ measurement of a QD from a nanobeam waveguide to check the single photon nature of the emitters. Figure 4.18 (left) shows a comparison between experiment and theory of contrasts for randomly distributed QDs. There is good qualitative agreement here with few contrasts that are 0.2 and below with the majority of contrasts laying around $0.7 - 0.8$.

PhC W1 QD Statistics

Figure 4.13 shows the contrasts for 35 QDs embedded in W1 waveguides. The black trace shows expected contrasts for ideal circularly polarised dipoles. The right panel of figure 4.18 shows a comparison of experimental and simulated contrasts for the W1 waveguide. Again there is a good qualitative agreement between experiment and simulations. There is a lack of high contrast QDs ($>70\%$). This is attributed to the point-like chiral areas within the waveguide design, making it unlikely that a randomly positioned QD will reside in this region. These results show that more higher contrast QDs are found in nanobeams compared to W1.
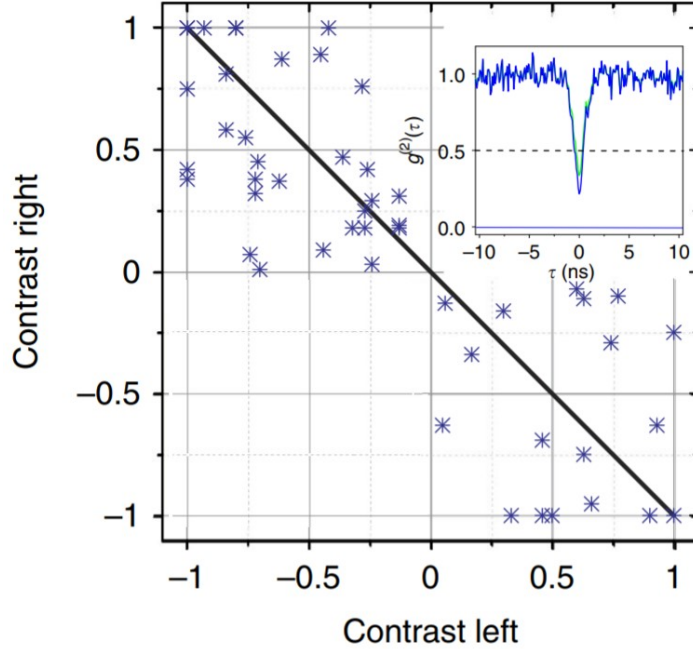
Figure 4.12: Contrasts of randomly distributed quantum dots in a nanobeam waveguide. Black line along the diagonal is the theoretical distribution of dots. There is a spread of points around this line. The inset shows a HBT measurement to verify the single photon nature of the emitters.

Non-resonant Field Dependence

The effect of magnetic field on the contrast was also explored. Figure 4.16 shows the magnetic field dependence for another chirally-coupled QD. Spectra were recorded from both ends of a waveguide at various field strengths, from 1T to -1T in 0.25T increments. All the spectra taken at different magnetic field strengths reveal high directionality of emission with absolute contrast independent of magnetic field to within 10%. As the experiments are performed at a magnetic field strength of 1T, see figure 4.11(c) and (d), the
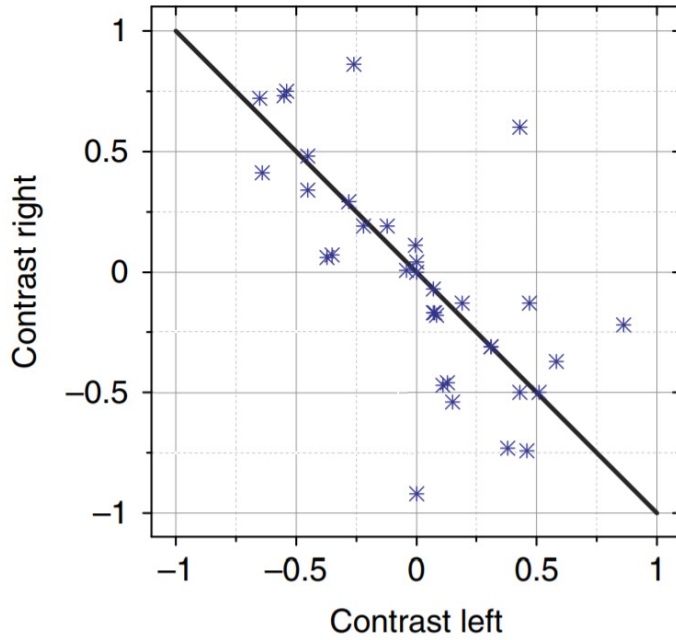
Figure 4.13: Contrasts of randomly distributed quantum dots in a W1 photonic crystal waveguide. Black line along the diagonal is the theoretical distribution of dots. There is a spread of points around this line.

exact excitonic species is not relevant to the observations made.

Resonant Field dependence

The magnetic field dependence was also investigated under resonant conditions. The idea being that in moving from above bandgap excitation, which excites both Zeeman split QD components, to a regime that should only excite a single component, would enable the selective excitation of a single component which may be useful in future QIP applications. Figure 4.15 shows the results of resonant excitation of the same QD as in figure 4.16. The observation of a resonant excitation signal has only been possible with
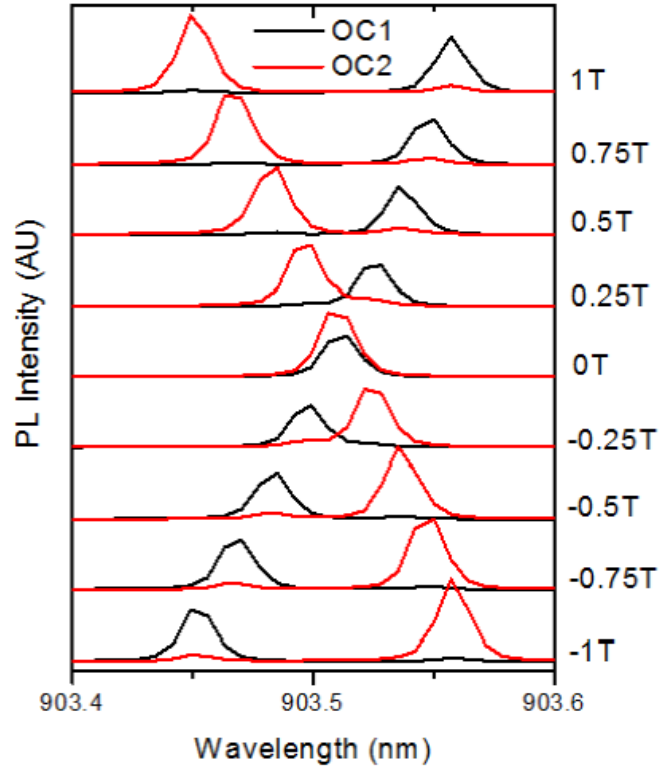
Figure 4.14: Nonresonant excitation of a chirally coupled QD in a nanobeam waveguide. Spectra taken at various field strengths, from -1T to 1T, are shown. There is less than 10% change in contrast over the range used.

a small number of QDs. The results under resonant excitation are similar to non-resonant excitation, with a small contrast change over a 0.2T range. This technique offers a greater resolution and gives a linewidth of $\sim 22 \mu eV$. The x-axis is offset compared to figure 4.14 due to an offset between the wavelength the spectrometer reads and the wavelength of the tunable resonant laser. See chapter 6 for resonant measurments.
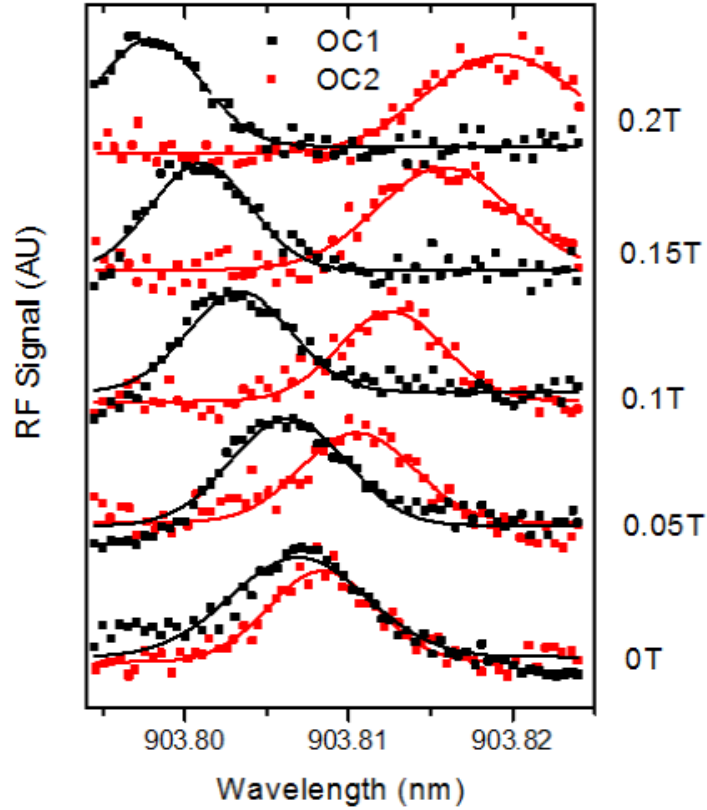
Figure 4.15: Resonant excitation of a chirally coupled QD in a nanobeam waveguide. Spectra taken at various field strengths, ranging from 0T to 0.2T, are shown.

Comparison of Spin Readout in Nanobeam and W1 waveguides

In this section a comparison of the results for the suspended nanobeam and W1 waveguides in simulations and experiments will be made. Figure 4.16(a) shows histograms showing the spread of contrasts for QDs in a suspended nanobeam. The red (green) histogram shows the experimental (simulation) results. When looking at the nanobeams there is a lower probability of finding very low contrast QDs. Experiment and simulation support this.

The opposite is true for the W1s, with a low number of very high contrast QDs being found in experiment, as is predicted by the simulations. There is a good qualitative agreement between simulation and experiment. From these results, it seems the nanobeam is a favourable choice compared to the standard W1 waveguide.
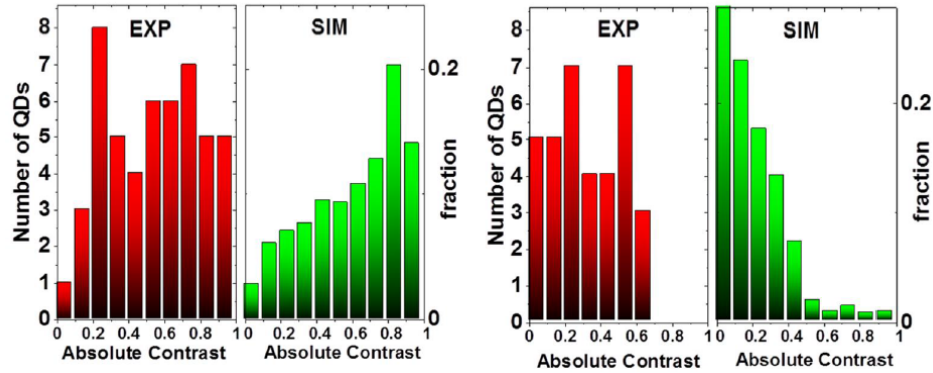
Figure 4.16: Contrast values, both from experiment (red bars) and simulation (green bars) for nanobeam (left) and W1 (right) waveguides.

4.3.2   Spin readout with position registered QDs

The positions of six QDs were registered, so they may be positioned at specific points within the waveguides, to see if the simulation results could be verified experimentally. Of the six registered dots three did not survive fabrication. Results will be shown for a symmetrically and chirally-coupled QD. The QD registration method is explained in section 4.4.3. Figure 4.17(a) (top panel) shows a QD spectrum taken before any fabrication, where the QD exciton is highlighted. The bottom panel shows the same QD after a waveguide has been fabricated around it. The relative intensities of the QD excitation

species changed slightly after fabrication, but the QD was still able to be identified from its spectrum. This QD, which will be referred to as QD I, was positioned at a chiral point. Figure 4.17(b) shows spectra at various field strengths showing chiral emission form QD I. It is clear that the higher (lower) energy component dominates the red (blue) spectra. The directionality factor of this QD is $|C_{LEFT}| = 92\pm3\%$ and $|C_{RIGHT}| = 80\pm3\%$.

A control sample, with a QD (QD II) embedded in the centre of a waveguide, was also studied. Figure 4.18(a) shows spectra of QD II before and after fabrication similarly to Fig. 4.17, and (b) which shows the results of the spin read-out experiment. As can be seen, both components are clearly visible from both outcouplers. Data shown is taken at 0T (black trace) and 2T with the red (blue) traces being recored from the right (left) couplers. The contrasts for this QD are much lower than for QD I. With $|C_{LEFT}| = 3\pm6\%$ and $|C_{RIGHT}| = 24\pm4\%$. This is as expected for a QD located at the centre of a waveguide. This shows that by deterministically positioning QDs within nanophotonic waveguides, unidirectional emisson can be achieved, where the spin of the emitter determines the emission direction. Acknowledgement is given to James Dixon who carried out nearly all of the position registration work.

4.4 Discussion

In conclusion, it has been shown both experimentally and theoretically that chiral behaviour can arise in a simple system comprising of waveguides with embedded emitters, where the position of an emitter within a photonic waveg-
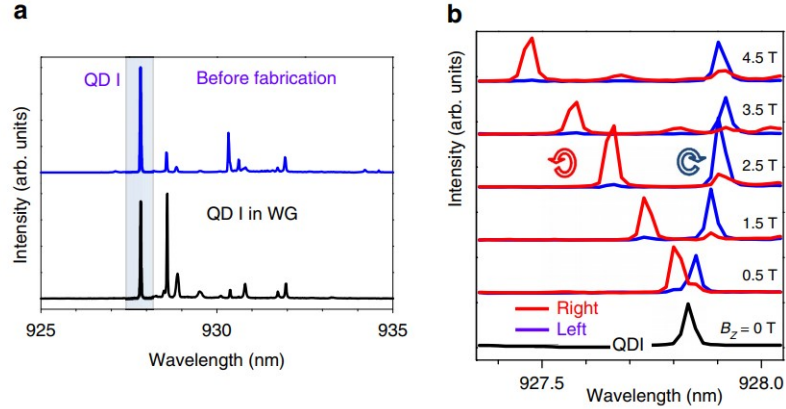
Figure 4.17: (a) Spectra showing a QD in bulk wafer before fabrication (top panel) and after fabrication (bottom panel) (b) Magnetic field dependence of emission from the registered QD I collected from the left out-coupler (blue) and right out-coupler (red).

uide determines the directional properties of the emission. Depending on the position of the emitter anything from complete uni-directional emission to completely symmetrical emission may be observed. The unidirectional phenomena reported here may be used for spin-readout applications and to transfer spin information around a photonic circuit.

Scatter around the diagonal in figures 4.12 and 4.13, is currently unexplained, but may arise due to back-reflections from the couplers or elliptically polarised dots. The directionality may also be affected by the proximity of QDs to surfaces[117] and the finite size of the QD, where the point-like dipole approximation[118] is no longer valid.

By deterministically positioning QDs within waveguides, and by connecting devices together, this may offer a possible route to scalability. The regions found from simulations for the highly chiral areas show that for spin readout
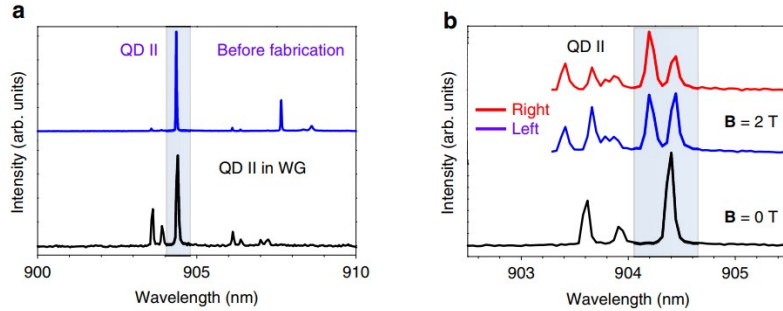
Figure 4.18: (a) Spectra showing a QD in bulk wafer before fabrication (top panel) and after fabrication (bottom panel) (b) Spectrum from the registered QD II collected from the left out-coupler (blue) and right out-coupler (red).

applications, nanobeams are advantageous when compared to PhC W1s due to the larger chiral areas when compared to the W1. Also, with nanobeams being a much simpler structure, there is a lower risk and sensitivity to fabrication defects. The findings and techniques presented here could contribute to the creation of spin-optical on-chip networks and processing devices based on nanophotonic waveguides.

4.5 Further work

The process of QD position registration for use within photonic structures is not limited to one QD. In principle many QDs could be registered and have photonic structures fabricated around them. This could lead to the creation of more complex circuits with several integrated components connect via semiconductor circuitry with deterministically coupled QDs using a chiral interface to realise spin–photon and spin–spin entanglement on chip.

Other photonic structures may offer future advances in this field. One ex-

ample is the glide-plane waveguide, whose structure is designed to overcome the shortcomings of the standard W1 waveguide, by increasing the chiral areas. Photonic crystal waveguides are also able to take advantage of slow-light modes and have Purcell-enhanced emission, whereas a suspended nanobeam waveguide cannot.

Chapter 5

Path-dependent initialization of a single quantum dot exciton spin in a nanophotonic waveguide

5.1 Introduction

There has long been interest in using the spin states of QDs, as matter qubits, for applications in QIP. With many of the necessary processes, such as entanglement between spins separated by large distances[119], being demonstrated using off-chip schemes[120]. As such, scalable and compact spin networks[121, 122], will require the integration of QDs embedded within photonic environments. Embedding QDs within photonic environments can also enhance the light-matter interaction[67] and provide an efficient method for

73

the generation and manipulation of single photons on-chip[123]. Spin networks can then be envisioned, provided there is faithful conversion between matter qubits (QD spins) and flying qubits (photons), where QDs will store and process information and photons will transfer the information between nodes within a photonic circuit[20, 97]. To achieve this, an efficient spin-photon interface is needed to transfer the spin state of a qubit onto the polarisation or propagation direction of the flying qubit.

The previously reported directional emission[124], see chapter 4, is one example of spin-orbit coupling. In nanophotonic systems the spin-orbit coupling is a general property, which arises due to the wavelength-scale confinement of these systems, which in turn can support elliptically polarised electric fields in guided modes[103, 125]. Many experiments in the literature demonstrate unidirectional propagation of photons based on the spin state of an emitter[99, 102, 104, 126, 100, 101, 98, 127, 105]. All these experiments map the spin of an emitter to the direction of propagation of the emitted photons within the photonic structure. This is only half the story however, as a fully realised spin-network will also require the reverse process, mapping the photon propagation direction to the spin state of an emitter. This reversibility has recently been shown in a silicon microdisk coupled to a waveguide[127] and for a single ^{85}Rb atom evanescently coupled to a whispering gallery mode resonator[99].

In this chapter, the path-dependent initialisation of a single quatum dot exciton spin coupled to a single-mode suspended nanobeam waveguide is presented. The fidelity of the path-to-spin conversion is measured using the spin-to-path readout, as presented in chapter 4. By injecting photons into

the waveguide, thereby defining their propagation direction, it is possible to excite a single corresponding component of the QD exciton. Then, due to the chiral coupling between the QD and waveguide, the emission direction of the emitted photon will be dependent on which spin state of the QD is excited. The direction dependent initialization and subsequent readout is a step towards achieving photon mediated spin-to-spin communications, as well as potential logic gate styles of operation, which may help facilitate a quantum spin network.

5.2 Experimental Arrangement

Three independent optical paths were used for exciting the samples and collecting any emission. An above bandgap laser was used to stabilise the charge environment around the dot and enable excitation of the QD using quasi-resonant (p-shell) excitation. The quasiresonant laser can be positioned on either Bragg coupler to inject light into the waveguide mode; defining its direction. The collection path can also be moved around and collection is mainly done at the terminating couplers. See section 3.3.8 for more details. A magnetic field of up to 5T can be applied along the growth direction of the QDs. A schematic of the initialisation experiment is shown in figure 5.1, it shows the relationship between the propagation direction within the waveguide ($-k_x$, k_x), the trion pseudospin ($\uparrow$, $\downarrow$), and photon polarisation (σ^+, σ^-). This only applies for a QD located at a chiral point.

The experimental scheme used for QD spin initialization is presented in Fig. 5.1, and assumes perfect chiral coupling between the QD exciton and
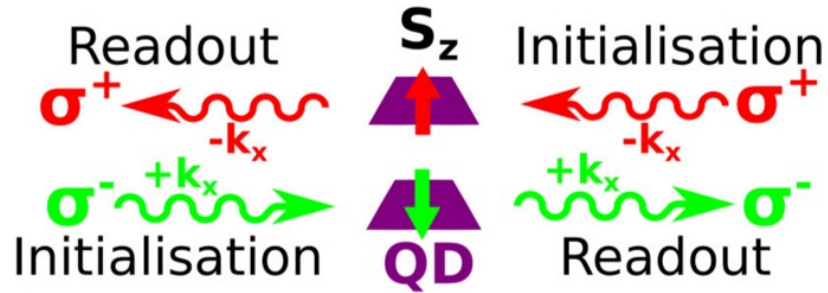
Figure 5.1: Schematic showing the chiral interface for initialization and readout.
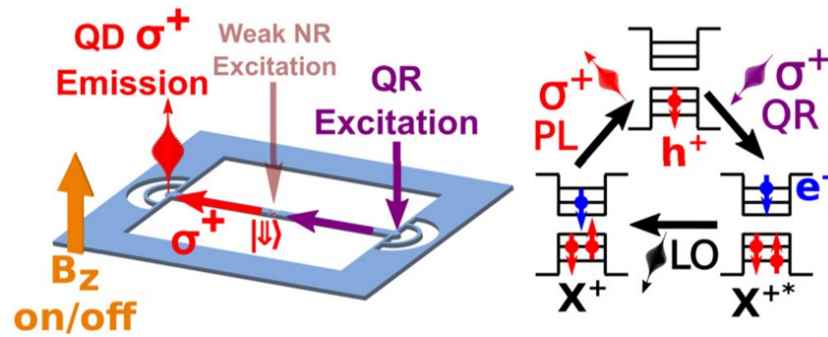
Figure 5.2: (left) Schematic of the initialisation experimental procedure for excitation from the right. (right) Shows the excitonic species involved in QR excitation. The opposite is the case when exciting from the opposite side.

the waveguide mode. If a quantum dot is located at a chiral point (c-point), then the orthogonally polarised exciton spins will emit photons in opposite directions along the waveguide with contrast ~1[124]. By choosing which side of the waveguide is used for excitation, and hence the propagation direction of the excitation photon within the waveguide, dictates which exciton spin component will be excited. When the excited state decays back to its ground state, assuming no spin manipulation or scattering into non-guided modes, the emitted photon will travel in the same direction as the excitation photon.

The fidelity of the path to spin conversion can be measured by collecting photoluminescence (PL) signals from each terminating Bragg coupler.

As these devices contain randomly distributed SK QDs it was necessary to study an ensemble of QDs to find a dot suitable. A good candidate QD for path-dependent initialisation must be highly chirally-coupled, and as such, directional spin-readout was used[124], along with other QD properties such as linewidth etc. to rank several QDs. A non-resonant laser (808 nm) was used to excite the QD from above, see figure 4.11(a) and QD emission was collected at the terminating couplers. A field of 1T was applied in the growth direction of the QDs to Zeeman split the degenerate components for easy identification as the states will be split in energy and circularly polarised as in section 4.5 figure 4.11(b).

5.2.1 Polarisation control

Polarisation control, on the excitation path, was achieved by the use of a linear polariser, half waveplate and a variable waveplate. The variable waveplate was used to account for any birefringence in the system and also to change the linearly polarised light, which is determined by the angle of the linear polariser, to circularly polarised light. With this information it is possible to see what effect if any, polarisation has on this system.

5.3 Results

In the following section, the results from the spin initialisation work will be presented. Similarly to equation 4.1 the initialization contrast is defined as

$$C_{det.l/r}^{init} = \frac{I_L - I_R}{I_L + I_R} \tag{5.1}$$

where the lower case subscripts l/r refer to the detection on either the left or the right coupler, and the uppercase subscripts L/R refer to the couplers used for excitation, and $I_{L/R} = I_{L/R}^{\sigma+} + I_{L/R}^{\sigma-}$ where $\sigma^{+/-}$ refer to the PL emission peaks (see fig 5.9).

5.3.1 Identification of Excitonic Species

Figure 5.3 shows a PLE spectrum of the QD, where the X^0, XX and trion states were identified from their relative power dependences and energy separations. The line under study in this chapter is attributed to the positively charged trion due to lack of detectable FSS and emission energy $\sim 0.4meV$ below the X^0 recombination energy, which is in agreement with the energy range for X^+ recombination[128, 93]. As shown in the right panels of figures 5.3 and 5.4 the positive trion recombines leaving a residual hole behind, $X+ \to h+$, which requires the use of NR excitation combined with the QR excitation to observe. Without application of the NR excitation this line is not observed. The X^- is typically $5 - 7meV$ lower in energy than the neutral exciton[129]. The relative energies of other excitonic species presented in Fig. 5.6 are in good agreement with those presented in refs[128, 93]. The spin states of X^+ are $|\downarrow\Uparrow\Downarrow\rangle$ and $|\uparrow\Uparrow\Downarrow\rangle$, where $\uparrow, \downarrow$ and $\Uparrow, \Downarrow$ denote electron and heavy hole spins respectively. These states correspond to residual hole spin states $|\Downarrow\rangle$ and $|\Uparrow\rangle$ where σ^+ and σ^- photons are emitted, on exciton recombination, to the left and right waveguide directions respectively.
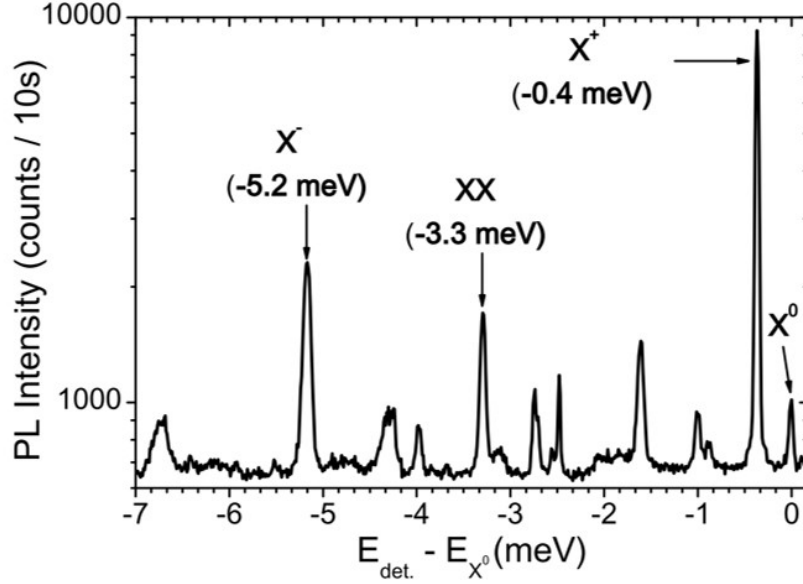
Figure 5.3: Spectrum showing excitonic species in a chirally coupled QD in a nanobeam waveguide. The x-axis shows relative energy seperation from the neutral exciton.

5.3.2 Finding the p-shell resonance

To find the p-shell resonance a PLE experiment was performed. With the stabilising laser applied to the QD; the excitation laser was applied to the left Bragg coupler and tuned through a 10nm range from 880-890nm. PLE signal was then collected from the right grating. The intensity of the QD peak at 911.5nm was recorded as a function of excitation wavelength. The power of the stabilising laser was $\sim 10nW$ and the power of the excitiation laser was $\sim 650nW$. The results of this are shown in fig. 5.7.

The bottom axis of figure 5.4 is given as a detuning from the ground state energy of the exciton transition. It shows a broad resonance at a detuning
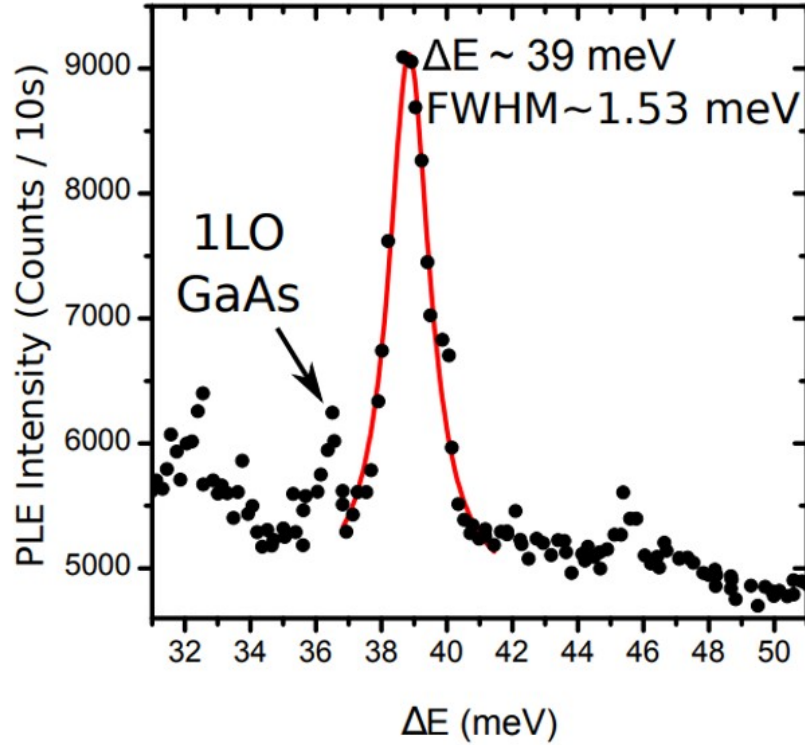
Figure 5.4: PLE spectrum of a chirally coupled QD. The x-axis shows detuning relative from the X^+ emission energy.

of $\sim 39 meV$ There are also some other features in this spectra, such as the 1LO phonon resonance at slightly lower energy.

5.3.3 Single Photon Verification

The single photon nature of the emission from the QD under study was verified by a second order correlation measurement. Figure 5.8(a) and (b) show a $g^{(2)}$ measurement taken under non-resonant and quasi-resonant excitation conditions respectively. As can be seen, at time $t = 0$ there is

marked dip in both sets of data. Under non-resonant excitation, the auto-correlation function $g^{(2)}(\tau)$ shows a value of $g^{(2)}(0) = 0.06 \pm 0.04$. The value under quasi-resonant excitation shows a higher of $g^{(2)}(0) = 0.21 \pm 0.03$. The larger value under quasi-resonant excitation is attributed to bunching due to charge fluctuations as previously observed [130]. These results confirm the single photon nature of the QD emission and also that the single photon nature is maintained under QR excitation.
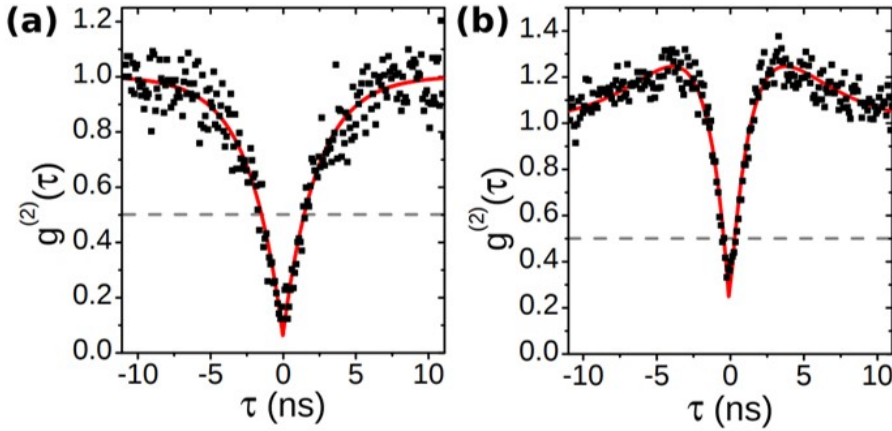
Figure 5.5: (a) Autocorrelation function $g^{(2)}(\tau)$ for NR excitation. (b) Autocorrelation function for QR excition.

5.3.4 Chirally-coupled Path-dependent initialization

QD selection

As stated earlier, it is important to select a QD that shows high contrast in spin readout. Strong PL emission was observed, with each Zeeman component (σ^+/σ^-) predominantly coupling to opposite propagation directions
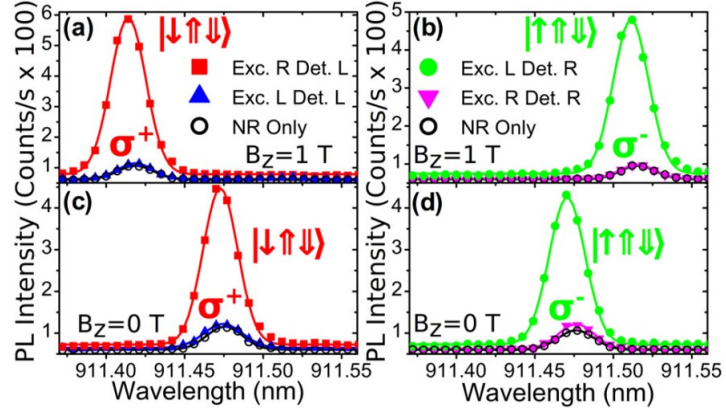
Figure 5.6: Spectra showing path to spin conversion results. Top (bottom) panel shows spectra taken from the right (left) out-coupler. Red and magenta (green and blue) traces are taken when the excitation laser is over the left (right) coupler.

(left/right) with a Zeeman energy splitting of $\Delta E_z = 147 \mu eV$. The spin readout contrast is calculated the same way as in chapter 4, using equation 4.1. Under non-resonant PL emission the measured contrasts are $C_{det.l}^{read} = 0.95 \pm 0.05$ and $C_{det.r}^{read} = -0.88 \pm 0.06$ from the left and right out-couplers respectively. The slight asymmetry between the measured contrasts could be caused by different reflection and extraction coefficients of the grating couplers due to fabrication defects.

As this QD shows a high degree of spin to path conversion it was chosen for QR spin initialisation. The spin state of the emitter determines which direction and hence the polarisation of the emitted photons. For QR spin initialisation photons are coupled in through the Bragg couplers, defining their propagation direction, which it turn excites the QD component that is coupled to that mode and not interacting with the other component.

Using the charged exciton has advantages over the neutral exciton due to

the lack of FSS, this means the spin states of the trion are always circularly polarised, and so directly map the propagation direction or polarisation to the spin state of the emitter after absorption. This is not the case for the neutral exciton which has linearly polarised states at low magnetic fields. Resonant excitation of the X^+ trion would enable coherent initialisation and control of the residual hole spin[131, 132, 133, 134]. Separating the RF signal from the QD and the excitation photons is not straight forward[130]. A tunable diode laser is incident upon one of the Bragg couplers and tuned to the p-shell resonance of the trion. This QR excitation has been shown to be spin preserving and to initialise the s-shell exciton spin states with fideltiy in planar samples[135] of > 0.95. Filtering the excitation field from the QD signal is now easily achieved using spectral filtering.

As shown in figures 5.3 and 5.4, QR laser photons are coupled into the waveguide through the terminating Bragg couplers. They then propagate along the waveguide, where they interact with a QD located at a c-point. The QD absorbs the photon, transferring the photon spin to the spin state of the p-shell X^+ trion. The carriers relax to the ground state in a spin preserving process. Recombination of the trion produces a σ^+ or σ^- polarised photon, which propagates either to the left or right depending on the initial spin state. The weak NR laser is applied from directly above the QD as in chapter 4.

Results from the QR initialisation experiment for a chirally-coupled QD is presented in figure 5.10. The measurements were performed with an applied magnetic field $B = 1T$. This separates the QD exciton spin components in energy for easy identification. If the collection path is fixed over the right

coupler, figure 5.10 (top panel), and QR excitation is coupled in from the left, a strong emission peak is observed for the σ^- component (red trace). If the excitation is moved to the right side (green trace) then no signal is observed. Weak signal is observed due to application of the NR laser, but this is a rather weak effect, and the contribution to the signal from the NR excitation is subtracted from the results shown. The opposite is true if the collection is moved to the left coupler. Here there is a strong σ^+ component observed when exciting from the right and no signal when exciting from the left. The results can be understood in the following way. When QR excitation is applied to the left couper, the waveguide mode travelling from left to right is excited. The application of NR excitation populates the QD with a hole of random orientation. If the hole is in the $| \Uparrow \rangle$ state then the QD will absorb the σ^- polarised QR photon. This will create a X^- trion with spin state $| \uparrow\Uparrow\Downarrow \rangle$ spin state. This exciton will then recombine, emitting a σ^- polarised photon in the same direction as the original excitation photon. This then leaves behind a residual hole in the $| \Uparrow \rangle$ state that can be used again to initialize the state, or the hole orientation can be randomised by the NR laser. If the residual hole is in the $| \Downarrow \rangle$ state then a QR excitation photon travelling from left to right will not excite the QD. The opposite spin states are excited when coupling in through the opposite coupler, see the bottom panel of figure 5.10. In the absence of exciton spin flips within the QD, emitted photons are not expected to be observed from the same coupler as excitation takes place. The directional emission shows there is a high degree of spin memory within the QD. Hence the device exhibits path-spin and spin-path conversion $|L\rangle \leftrightarrow | \downarrow\Uparrow\Downarrow \rangle$ and $|R\rangle \leftrightarrow | \uparrow\Uparrow\Downarrow \rangle$ where L and R

are the propagation directions of the photon within the waveguide.

The calculated contrast for this QD are $C_{det.l}^{init.} = -0.96 \pm 0.05$ and $C_{det.r}^{init.} = 0.99 \pm 0.06$. The small asymmetry in contrast values is possibly due to small differences in the fabrications of the terminating couplers. It is noted that the need for a NR laser could be removed by implementing p-type doping of the sample[136] and thus make the performed PL subtraction unecessary.

The experiments were also performed at 0T as the requirment for an external magnetic field may limit the scalability of this system. The calculated contrasts were still relatively large, with initialization contrasts calculated as $C_{det.l}^{init.} = -0.96 \pm 0.03$ and $C_{det.r}^{init.} = 0.92 \pm 0.03$ (see section 5.4.7). These slightly reduced contrast values are attributed to electron dephasing caused by the Overhauser field of nuclei in the QD at $B_z = 0T$[136, 137].

5.3.5   Symmetrically-coupled comparison

To confirm that the high degree of spin initialization arises due to the chiral coupling between the QD and waveguide, and not some other effect like the conservation of wave vector, a QD that does not show unidirectional emission was studied. This QD will be located at or very close to the centre of the waveguide, where the local polarisation in the waveguide is linear (L-point). A symmetrically coupled QD was identified using above bandgap excitation, just like in the chiral case, except both the σ^+ and σ^- components should be detected with roughly equal amplitudes from both Bragg couplers. The results of QR excitation on this nonchiral QD are shown in Figure 5.11. The results show almost equal emission intensities when the QD is excited from either grating coupler, and the signals levels are also independent of
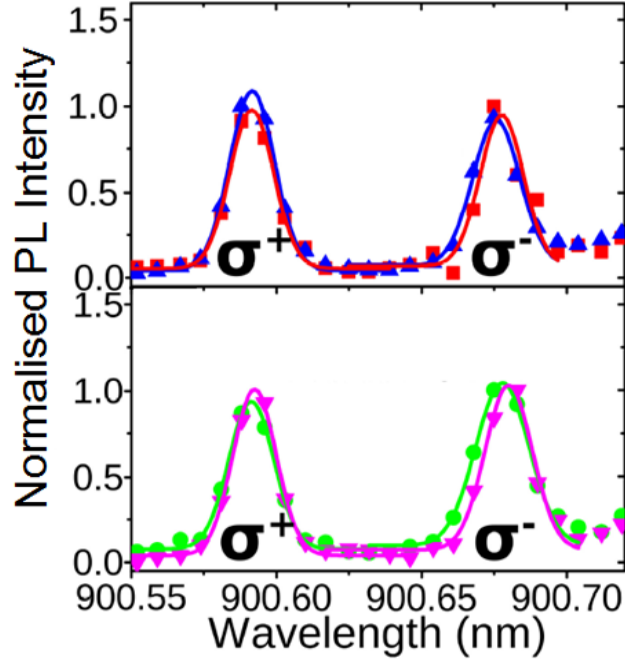
Figure 5.7: PL spectra for a symmetrically coupled QD. The top (bottom) panel show signals collected from the left (right) couplers with the blue and green (red and magenta) being excited from the left (right) couplers.

which coupler the emission is detected from, where extracted initialization contrasts very close to zero are found with $C_{det.l}^{init.} = (9 \pm 1) \times 10^{-3}$ and $C_{det.r}^{init.} = (-13 \pm 1) \times 10^{-3}$. These results confirm that the high fidelity of spin-path conversion for the displaced QD is indeed due to the chiral interface that arises between the QD exciton and the waveguide.

5.3.6   Polarisation dependence

The polarisation of the quasiresonant laser was also investigated. With the above bandgap repump laser fixed on the position of the QD and the col-

lection path fixed on one outcoupler. The quasiresonant laser was scanned over the whole waveguide. Fig 5.12 shows raster scans of the devices, where the left (right) column shows the detection fixed on the left (right) couplers. With panels (a)-(h) showing linear polarisations (H, V, D, and AD) (i)-(l) showing circular polarisations (σ^+ and σ^-). As can be seen in Fig 5.12, when collecting on the left (right) the majority of the collected signal is observed when the QR laser is on the right (left) out-coupler. All the panels show a high degree of spin initialization, meaning that the polarisation of the incoming laser has no effect on spin initialization.

It is expected that the polarisation of the incoming field should not have an effect on the contrast. This is because the photon does not retain the polarisation information once it is coupled into the waveguide mode. The intensity of PLE in panels (a)-(h) of Fig 5.12 vary, this is due to the polarisation of the incoming laser. This is because the incoupling efficiency depends upon the overlap between the mode of the incoming laser, which is polarisation dependent, and the free space modes of the outcouplers. Maximum efficiency is seen for linear polarisation (V); which is transverse to the waveguide mode. The design of the out-couplers is such that they principally couple transversely polarised light to the waveguide mode[130].

Figure 5.13 compares the experimental excitation maps (left column), when exciting through the right coupler, to simulated farfield profiles (right column) of the light scattered by this design of grating coupler. The simulations were produced by convolving the far field profiles of the grating and a Gaussian beam. Analysis of the profiles was done using a near to far field transformation of the monitor field data within the software[109]. As can be
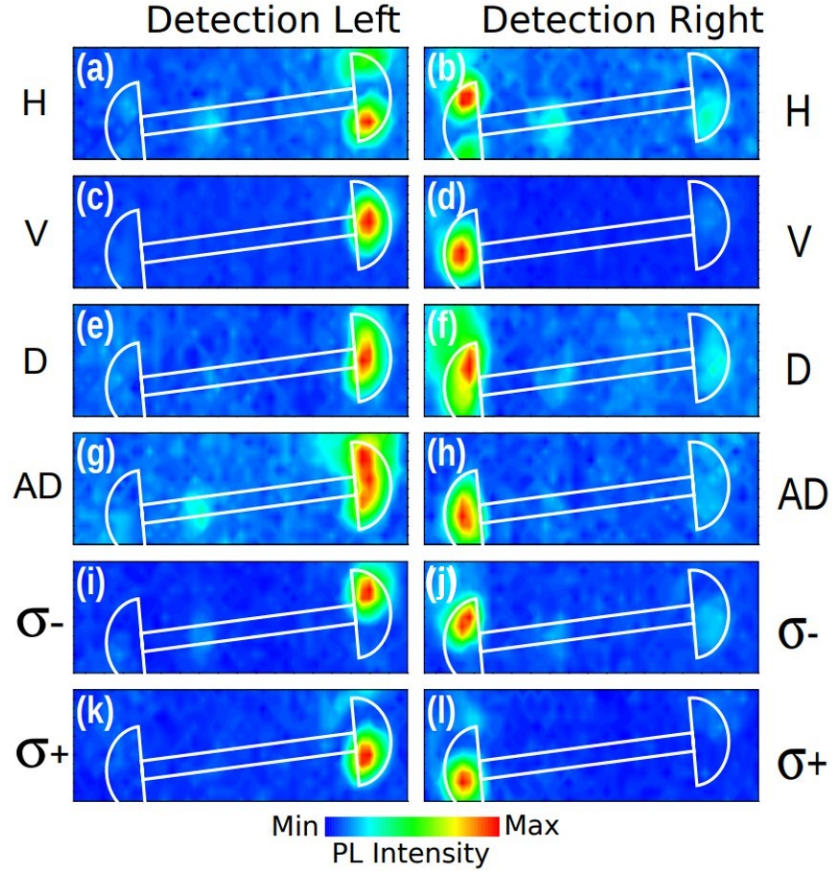
Figure 5.8: Excitation maps taken at $B_z = 0T$ using a raster scan of the quasires-
onant laser over the device, filtered at the QD emission wavelength of 911.5 nm.
The same laser powers were used in all scans. In the left and right columns the po-
sition of detection is fixed at the left and right grating coupler respectively, when
the QR laser polarisation is (a)-(b) horizontal, (c)-(d) vertical, (e)-(f) diagonal,
(g)-(h) antidiagonal, (i)-(j) left circular, and (k)-(l) right circular. The polarisa-
tions are defined relative to the horizontal axis of the apparatus. A schematic
outline of the waveguide and coupler is added in white. The apparent rotation of
the devices is due to a small rotation induced by the detection optics.
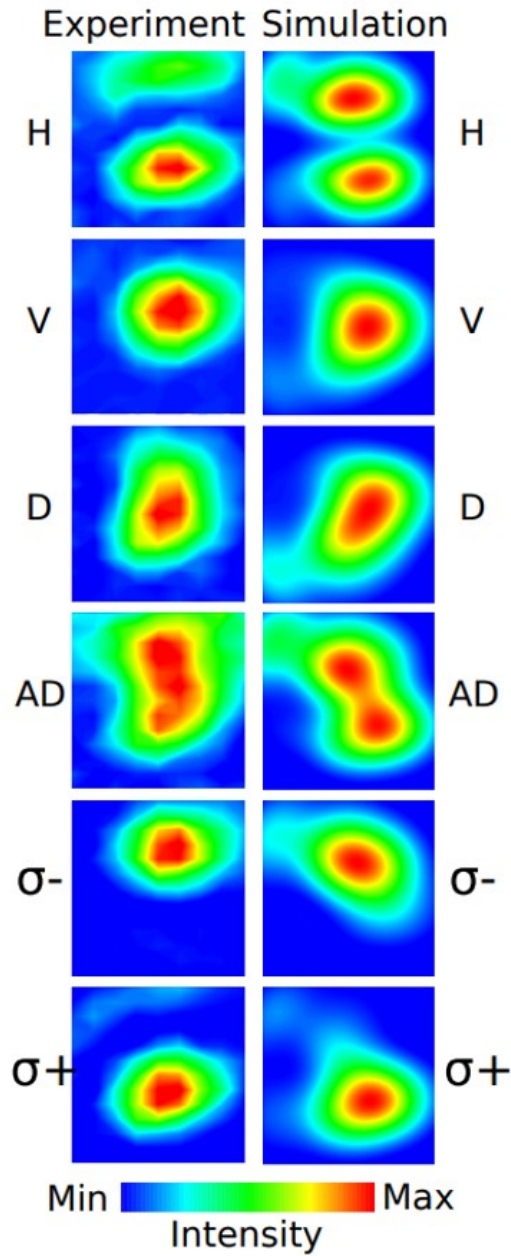
Figure 5.9: (left column) Excitation maps over the right grating coupler when collecting PL emission from the left grating coupler for a range of laser polarisations. (right column) Simulated farfield profiles of scattered light from a grating coupler for a range of polarisations. In the simulated data, a convolution of the far fields of the grating coupler and a Gaussian beam is applied.

seen in figure 5.13, there is good agreement between experiment and simulation. This confirms the origin of the profiles observed in figure 5.12. The weaker component in experiment for the H polarisation is due to less efficient collection of signal as the maximum travel range of the mirrors in the optical path is reached.

Vertically polarised light is mainly scattered when it is incident on the centre of the coupler and horizontal light is mainly scattered by the edges of the couplers; as can be seen in figures 5.12 and 5.13. The profiles of the diagonal polarisations are broader as they overlap with the y-polarised peak, and one of the x-polarised peaks. For the circular polarisations, peaks are seen above or below the centre of the grating coupler. This is due to the opposing phase of the longitudinal electric field components of the waveguide mode above and below the waveguide axis(see figure 4.3).

5.4 Discussion

In conclusion, in-plane spin initialisation and readout of a charged exciton spin in a chirally-coupled QD embedded within a single mode waveguide using a quasiresonant excitation scheme has been demonstrated. High directionality contrasts of ~ 1 at $B_z = 1T$ and > 0.9 at $B_z = 0T$ have been found in experiment. Comparisons with a symmetrically-coupled QD are made and show that the high fidelity of spin preparation is due to the chiral coupling of the QD. The component of the QD that will be excited is entirely dependent on the direction the excitation field propagates within the waveguide, and that it is independent of the polarisation of the excitation field that is

coupled into the waveguide. The findings and techniques presented in this chapter could establish a method for communication between two or more quantum dots linked via waveguides and integrated on-chip. This work may contribute to the realisation of spin-optical on-chip networks[125]. Finally, the scheme demonstrated here is applicable to on-chip spin logic operating at ultrafast speeds, chip scale optical isolators, and the investigation of a diversity of spin-orbit coupling phenomena in a variety of classical and quantum systems[103, 101].

Chapter 6

Non-Reciprocal Resonant Transmission and Reflection of a Chirally-Coupled Quantum Dot

6.1 Introduction

Single photon nonlinearities[138] where states with one, two or more photons interact differently depending on the number of photons are of interest in the field of quantum information processing (QIP). A two-level system deterministically coupled to a 1-dimensional waveguide can demonstrate single-photon nonlinearities. An important parameter in the coupling of a QD to a waveguide is the β-factor, which is defined as the fraction of light emitted by the QD into waveguide supported modes over the total amount of emit-

ted light. As $\beta \to 1$, and in the coherent limit, the interaction between a single photon with the TLS results in a π phase shift[139] for the photon as it is reflected back along the waveguide. However, when the incident state is composed of more than one photon, the potential for the formation of a bound state causes preferential transmission of the wave-packet[140], leading to bunched statistics in the transmitted field and the formation of an efficient single-photon nonlinearity. In the case where β is smaller than unity, and/or dephasing is present, the same effects occur but with smaller magnitude. Such effects have been observed other systems, such as semiconductor quantum dots (QDs) coupled to photonic crystal waveguides[141, 142] and Silicon or Germanium Vacancy centres coupled to nanobeams[143, 144, 145], with transmission dips as low as 60% now reported[146].

The non-reciprocal coupling between dipole emitters and nano-photonic structures[99, 101, 127, 105, 125, 147, 124, 102] increases the functionality of this system. The chiral effects between QDs deterministically coupled to nanophotonic waveguides arise from the spin-orbit interaction of light[103], due to the confinement of light by the waveguide, and leads to directionality in the β-factor. This means that orthogonal states of the exciton will couple to modes propagating in opposite directions along the waveguide. When a photon interacts with a QD located at a chiral point (c-point), it varies from the case described above as light is now transmitted with 100% probability and continues with a π phase shift, usually imparted onto the reflected component in the non-chirally coupled case. This forms the basis for a spin-dependent phase-shift, which can be used to implement a scalable quantum network[148]. In practice, this is hard to observe as parameters such as the

the β-factor are never unity. The directional coupling efficiency, β_{dir}, which is defined as the fraction of dipole emission which travels a single direction along the waveguide over the total dipole emission, is less than unity.

$$B_{dir}^{L/R} = \frac{I^{L/R}}{I^{Total}} \qquad (6.1)$$

So the behaviour of this system is expected to lie somewhere between the perfectly symmetric case and the perfectly chiral case. In this chapter, experimental data on a single QD chirally coupled to a nanobeam waveguide is presented with the use of a theoretical model to help describe the system. The main results are the observation of a reciprocity breaking spin dependent dip in the transmission spectra, which varies significantly depending on the direction of propagation through the waveguide. Reflection measurements are also performed where unexpectedly the more strongly coupled component shows the weaker signal. The numerical model provides an explanation of the observed effects in this system and attributes the reflection results to the partial saturation of the more strongly coupled component. Different behaviour is expected at lower power levels as described in section 6.2.

6.2 Theory

To gain a deeper understanding of the effects a chiral interface may have in transmission and reflection-type measurements, and any phenomena that may arise due to it, the system was modelled. Acknowledgements given to David Hurst for his work on developing the theoretical model using the Input-Output Formalism[149]. Fig 6.2 shows a simple schematic of the system, in

(a) System schematic.

(b) Selection rules.

(c) Directionality.

(d) SEM of a typical device.
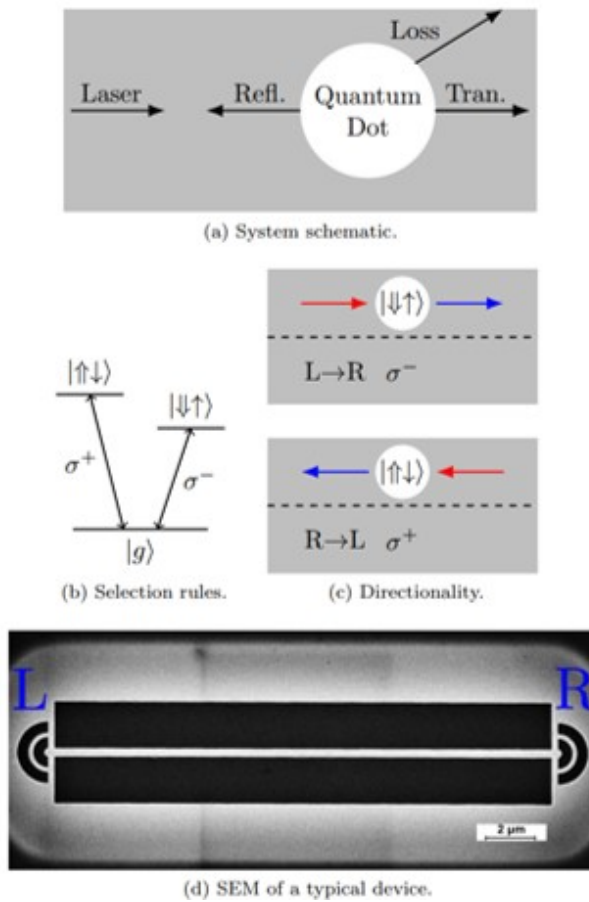
Figure 6.1: (a) Shows the interactions of an excitation field with a QD embedded in a waveguide. (b) Exciton transition rules. (c) The directional coupling. (d) Shows an SEM of a typical waveguide.

which a two-level system (TLS) is coupled to a continuum of modes of an optical waveguide. The transition from ground to excited state and vise-versa, couple either to the left propagating or right propagating modes depending on the helicity of the transition. Various parameters can be inserted into the model such as emitter lifetime and spectral diffusion. Values measured experimentally were put into the model with estimated values being used for the other parameters, see table 6.1. This was done to try and replicate the experimental results as closely as possible. In this section the main QD parameters are discussed as well as the results from the modelling.

Parameter	Symbol	Value	Notes
β-factor	β	0.7	Calculated in ref. [102]
Directionality	β_d	0.95	deduced from fig. 6.5
Radiative lifetime	τ	$1ns$	$0.95ns$ measured
Dephasing time	τ_d	$0.8ns$	comaprable to refs. [141, 142, 105, 130]
Spectral wandering parameter	σ	$4\mu eV$	deduced from PL linewidth
Dark probability	P_{dark}	0.25	In the range if refs. [141, 142]

Table 6.1: Table showing the parameters that were inserted into the numerical model.

The non-reciprocal spin-photon coupling of a chirally coupled QD arises from two factors: the chiral properties of the waveguide modes, and the strict selection rules for QD exciton transitions. The chirality of the modes originates from the strong light confinement in the nanobeam, which has lateral dimensions comparable to the wavelength of photons resonant with the QD transitions. The QD selection rules are illustrated in Fig. 6.1(b). Spin up ($| \Uparrow\downarrow \rangle$) or down ($| \Downarrow\uparrow \rangle$) excitons couple respectively to σ^+ or σ^-
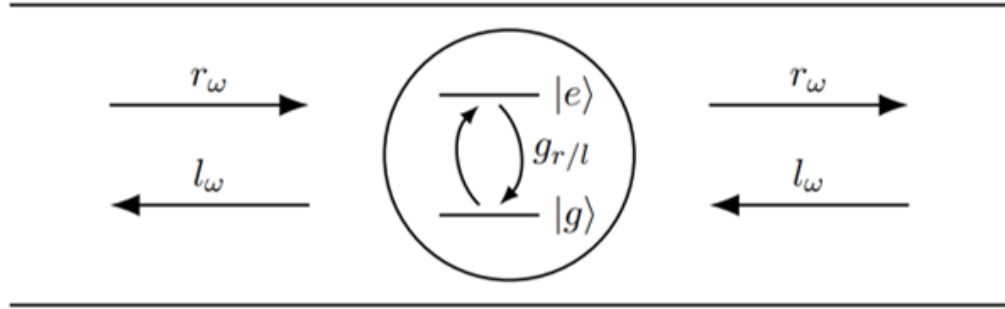
Figure 6.2: Two-level system interacting with the continuum of left and right propagating waveguide-confined modes.

circularly polarised light in order to preserve angular momentum. When such a QD is positioned at a C-point, the opposite circular polarisations propagate in different directions. The selection rules then imply that opposite spin excitons couple to modes propagating in opposite directions. This applies both to emission and to scattering, as shown schematically by the blue and red arrows respectively in Fig. 6.1(c).

As mentioned in the introduction, the transmission of an ideal chirally-coupled system is 100% for both QD spin states, but with a π phase shift for the transition that couples to the mode. Many factors influence the strength of the interaction and cause it to be lower than the ideal case.

The overall β-factor: The modelling of an ideal pointlike circular dipole emitter at a C-point of a nanobeam waveguide indicates that the total coupling corresponds to a best overall β-factor of around 70%[124]. This means that an excited QD will, with 30% probability, emit a photon into an unguided optical mode.

The pure dephasing rate: The characteristic features in the transmission

and reflection spectra rely on interference between the incident and scattered optical fields, making them highly sensitive to decoherence, which is described by the pure-dephasing time τ_d[150].

Spectral wandering and blinking: The charge environment around the QD is unstable and this causes line broadening as the exciton energy wanders on timescales set by charging and discharging of nearby trap states. Furthermore, there is always some finite probability P_{dark} that a photon arriving at the QD will find it in some optically inactive or 'dark' state. Both of these effects reduce the visibility of the resonant features in the spectra.

The directional coupling factor: This gives the probability that an exciton with given spin will emit preferentially to the left (L) or right (R), and is described by four parameters: ζ_L^+, ζ_R^+, ζ_L^- and ζ_R^-, where $+$ and $-$ represent the dipole spin. For ideal chiral-coupling, we would have $\zeta_L^+ = \zeta_R^- = 1$, and $\zeta_L^- = \zeta_R^+ = 0$. However, experimental values might be $\zeta_L^+ = \zeta_R^- = 0.95$ and $\zeta_L^- = \zeta_R^+ = 0.05$, owing to positioning of the QD slightly away from an ideal C-point.

Let us consider an imperfect dipole emitter located close to a C-point in a nanobeam waveguide, as illustrated in Fig. 6.1c. We assume that the dot has 95% directionality, with a left-to-right ($L{\rightarrow}R$) beam coupling predominantly to the $|\Downarrow\uparrow\rangle$ dipole, and vice versa for right-to-left ($R{\rightarrow}L$). The overall β factor is taken to be 70%, and we assume that the response of the QD is partially incoherent due to pure dephasing. A laser beam propagating from $L{\rightarrow}R$ will drive the QD strongly when resonant with the $|\Downarrow\uparrow\rangle$ dipole. This will cause both interference between scattered and incident fields, as well as emission into environmental loss modes, causing a dip in the transmission.
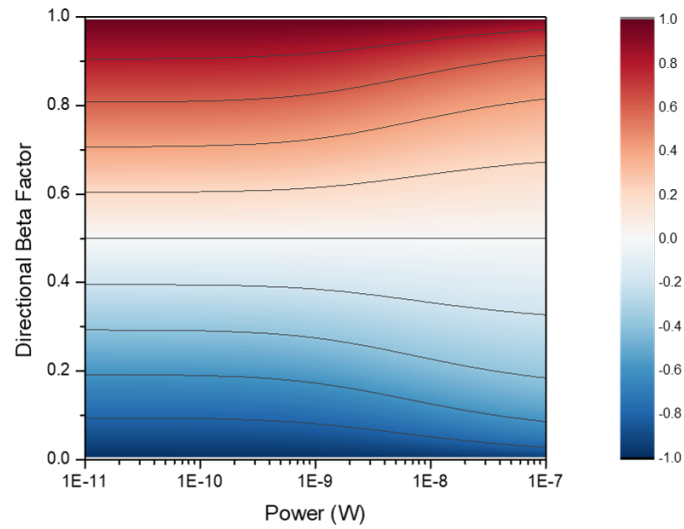
Figure 6.3: Calculated contrast as a function of directional β-factor and power in transmission. The darker areas show where the emission is most chiral.
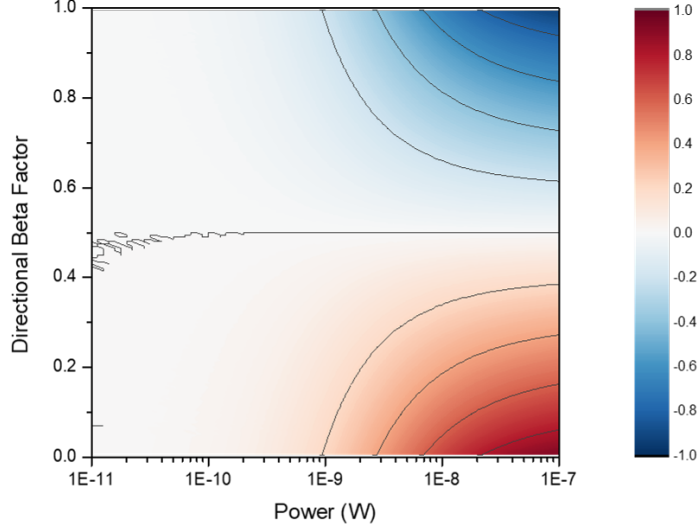
Figure 6.4: Calculated contrast as a function of directional β-factor and power in Reflection. The darker areas show where the emission is most chiral.

A much smaller dip is expected when resonant with the $| \Uparrow\downarrow \rangle$ dipole, as it couples only very weakly to the laser. We thus expect to see a strong difference in the transmission for the opposite circular dipoles, in agreement with the experimental data presented in section 6.4. The theoretical modelling reproduces this effect and clarifies that the depth of the $| \Downarrow\uparrow \rangle$ dip in our sample is limited by a combination of dephasing, spectral wandering and blinking.

Figure 6.3 shows a plot generated using the mathematical model introduced above. It shows expected contrast as a function of directional beta factor and the incident power of the excitation field at the location of the QD. The directional beta factor is used to quantify the degree of chiral-coupling

for a single Zeeman component with 0 and 1 being total chiral-coupling and 0.5 being symmetrically coupled. With a beta factor of 0.5 the contrast expected is always zero, regardless of power, as expected because the QD transitions interact equally with both the left and right propagating modes. As the power is increased the contrast for a given directional beta factor decreases. This can be thought of in the following way. As the power increases, the total energy in the system increases, this in turn leads to saturation of the emitter when interacting with the dominant propagation direction, and not in the opposite direction. So the highest contrasts in transmission should be observed at low powers, with only the most chirally-coupled systems maintaining high contrasts at higher powers.

It can be intuitively argued that the behaviour expected in a reflection geometry should be significantly different. Consider a $L{\rightarrow}R$ excitation field, coupling with $\beta_{dir} \sim 95\%$ to the $| \Downarrow\uparrow \rangle$ transition, which is in turn coupled to the opposite mode with $\sim 5\%$ transmitted into the $R{\rightarrow}L$ mode. The opposite is true for the $| \Uparrow\downarrow \rangle$ dipole, which couples 5% to the L$\rightarrow$R mode and 95% to the R$\rightarrow$L mode. Then, neglecting the interference effects, it might be expected that the same reflected signal be observed from both components. The fraction of the laser coupled into the R$\rightarrow$L mode is $\sim(95\% \times 5\%)$ in both cases and depends on the square of the β-factor[146]). This result is reproduced by the numerical model in the low power regime. On increasing the incident laser power towards the saturation limit of the QD, a qualitatively different behaviour is observed in experiment, with the reflection of a L$\rightarrow$R beam being much stronger for the $| \Uparrow\downarrow \rangle$ dipole. This asymmetry is reproduced by our numerical model, and can also be intuitively understood: the

transition that couples strongly to the incoming laser saturates first, leading to relatively stronger reflection for the other, nominally forbidden, transition. Figure 6.4 shows the contrast expected in reflection as a function of directional beta factor and power. As expected the contrast is low/zero for low powers or if the coupling is symmetric and asymmetry appears at higher powers.

For a symmetric system there should be no preference on propagation direction within the waveguide. Dips in transmission and peaks in reflection are still expected, but the features of the Zeeman components are expected to be the same magnitude. In the completely chiral case, however, a complete lack of a dip in transmission should be observed, and no reflection peak. Then light incident from the opposite direction should not interact at all, so again no transmission dip or reflection peak should be observed. In reality the experiment is more complicated as it is affected by all the factors discussed in this section. In the following sections the experimental results shall be presented and compared to the numerical model, which provides a good qualitative agreement for the behaviour observed (see section 6.4.3).

6.3 Experimental Arrangement

Figure 6.1 shows schematically the system under consideration. A QD that shows highly chiral coupling is coupled to a single-mode nanobeam waveguide and excited resonantly, as shown in Fig. 6.1(a). The non-chiral interaction of a dot with a resonant laser field has been studied in Refs.[141, 142, 146].In the following section a dot located at a C-point [125, 123] of the waveguide,

where the QD exciton spin couples to the direction of propagation[124, 123] is presented.

An above bandgap $808nm$ laser, which is termed the repump laser, was used to stabilise the charge environment around the dot and enable excitation of the QD using resonant excitation. The resonant laser can be positioned on either Bragg coupler to inject light into the waveguide mode; defining its direction. The collection path can also be moved around and collection is mainly done at the terminating couplers. See section 3.3 for more details. A schematic of the experiment is shown in figure 6.1(c), emission and resonant scattering are shown by the blue and red arrows respectively.

6.4 Results

Quantum dots near C-points were identified by non-resonantly excited photo-luminescence (PL), indicated schematically by the blue arrows in Fig. 6.1(c). The 808 nm, above band-gap, laser was focussed from above the waveguide and PL was collected from the left and right out-couplers. Over 50 randomly positioned dots were examined to find ones with highest spin-dependent directionality. Other properties such as intensity and linewidth were also taken into account when choosing potential QDs to perform experiments on.

The PL spectra at $B = 1T$ for the chirally-coupled QD employed in most of this chapter is shown in Fig. 6.5. Contrast values of $C_R = -0.91$ and $C_L = 0.84$ are found (See equation 4.1), with σ^+ light propagating predominantly to the left and σ^- predominantly to the right, as in Fig. 6.1(c). The Zeeman components are split due to application of the 1T magnetic field

parallel to the growth direction. This is necessary in this experiment for the chiral behaviour to be observed as degenerate components would render the chiral behaviour undetectable. With a candidate QD selected the response of the system under resonant excitation was explored.
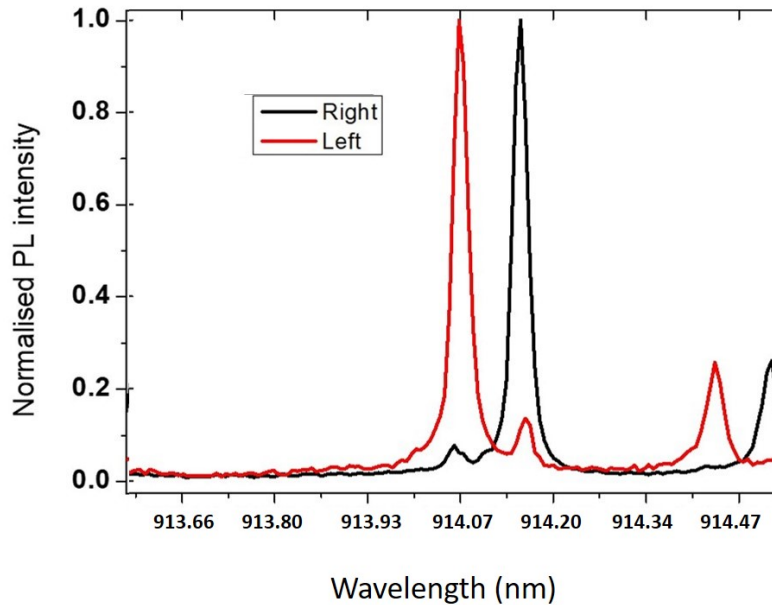
Figure 6.5: Spectra showing PL from a chirally-coupled QD in a waveguide where the black (red) trace shows emission collected from the left (right) coupler.

Ground State Dynamics

To achieve the best possible results; the ground state dynamics of the QD were investigated. As previously noted (See chapter 5), the use of an above bandgap excitation has been required in the past to stabilise the charge environment of the QD, and enable p-shell/quasi-resonant excitation. There is no resonant signal from the QD without the above band-gap laser, where
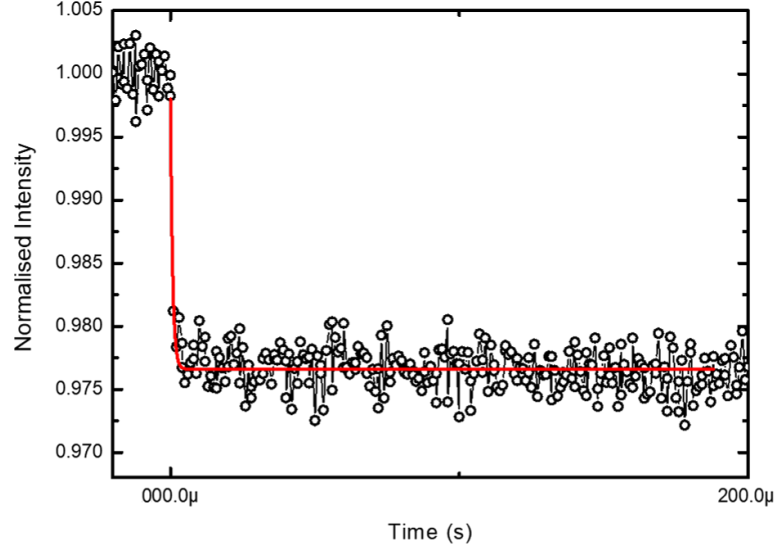
Figure 6.6: Ground state dynamics of a QD within a waveguide. This plot shows the typical time for a QD to capture a residual charge from the environment and becoming optically active.

it is referred to as the repump laser, as it creates free carriers to occupy and fill charge traps stabilising the environment. As we are likely working with a charged state of the QD, a residual charge has finite probabilities of tunnelling in and out of the QD in typical times. Here we define the ground state lifetime, τ_g, as the typical time taken for a charge to tunnel out of the QD, and τ_c, as the time taken for the QD to capture a charge. This sets limits to how fast we can switch the QD. Figures 6.6 and 6.7 show that the typical time for a charge to tunnel out of the QD and leave the QD in a dark state is $\sim 5\mu s$ and the typical time to capture a carrier and become optically active is $\sim 1\mu s$ respectively.
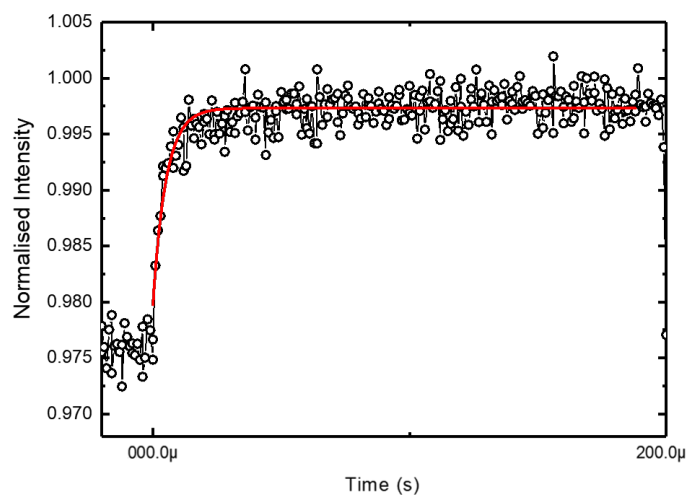
Figure 6.7: Decay of the ground state to dark state as a function of time. At t=0 the repump laser is turned off and the change in transmission versus time is recorded.

An Acousto-optical modulator was used to cycle the QD between its on and off states. This enabled the use of lock-in techniques to measure differential transmission and reflection spectra with high sensitivity. A frequency of 500Hz was used. This speed is much slower that the typical tunnelling times of the carriers associated with the QD. Using a faster cycle time reduces noise as it removes noise from components slower than the chopping rate. The caveat to this is that measured signal levels will be lower so longer intergration times are needed.

6.4.1   Transmission Results

The geometry for the experiment is shown schematically in Fig. 6.1(c). Excitation was provided by a tunable single-frequency laser coupled to one of the sets of Bragg couplers. Signal was detected from the opposite Bragg coupler. An 808 nm non-resonant repump laser was applied to stabilise the QD charge state[130]. There was no transmission signal without application of the repump laser. The normalised differential transmission spectrum, ΔT, was obtained by recording the signal intensity with and without the repump laser:

$$\Delta T = \frac{(I_{ON}^T - I_{OFF}^T)}{I_{OFF}^T}$$

where I_{ON}^T and I_{OFF}^T are the transmitted signals with the repump laser on and off respectively. The result here gives the contribution from the resonant QD transition. Moving the collection to the opposite Bragg coupler and repeating the measurments gives the reflection differential spectrum, ΔR, given by:

$$\Delta R = \frac{(I_{ON}^R - I_{OFF}^R)}{I_{OFF}^T}$$

where the superscript R represents the reflected signal. The experimental data showed a Fano lineshape for the transmission and reflected siganls. The asymmetric, Fano-resonance lineshapes are due to interference between the laser scattered by the QD and the spectral quasi-continuum arising from Fabry-Perot modes of the nanobeam which form due to back-scattering from the in and out-couplers[141].The fitting of the data was performed using Fano lineshapes described by the following equation:

$$y(\omega) = y_0 + A\frac{(q\Gamma + \omega + \omega_0)^2}{\Gamma^2 + (\omega - \omega_0)^2}$$

where y_0 is the background level, A is the signal amplitude, q is the Fano parameter, Γ is the line broadening and ω_0 is the resonant frequency. The experimental contrasts in transmission and reflection were then calculated from the fitted amplitudes given by:

$$C = \frac{I^{\sigma+} - I^{\sigma-}}{I^{\sigma+} + I^{\sigma-}}$$

Having identified and optimised the experimental method for a chirally-coupled QD, investigation into the non-reciprocal behaviour in resonant transmission was ready to proceed. A magnetic field separates the QD states ensuring the emitted photons hace circular polarisations[124]. In this chapter, however, the QD state is most likely charged, since the repump laser creates free electron-hole pairs. Lock-in techniques were used to maximise the signal to noise in the detection of the resonant laser transmitted through the output Bragg coupler[151].
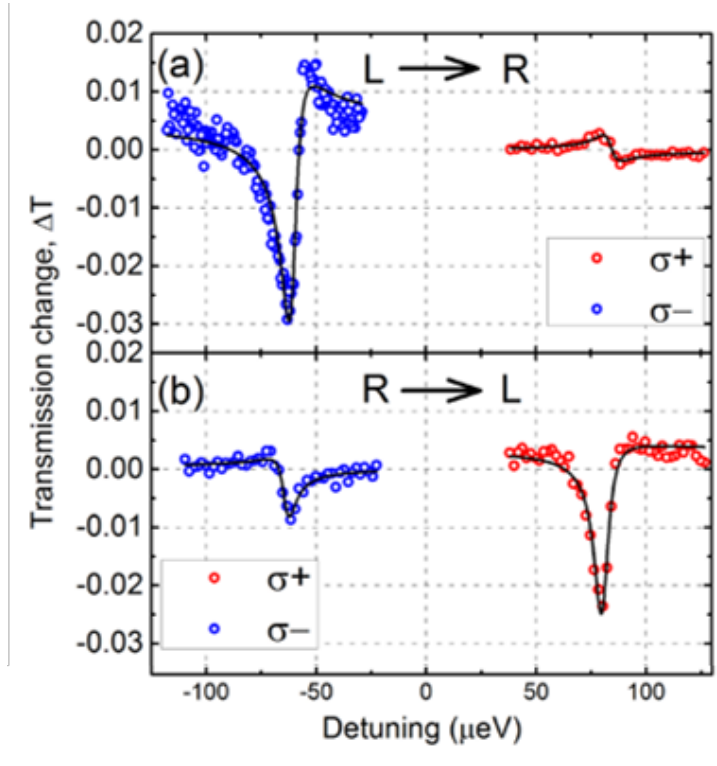
Figure 6.8: Differential transmission spectra for the chirally coupled QD at B =
1 T: (a) transmission change when resonant field is propagating towards the right;
(b) transmission change when resonant field is propagating to the left.

Resonant transmission spectra for L→R propagation are shown in Fig.
6.8(a), and for the opposite direction R→L propagation in Fig. 6.8(b). The
Energy axis is presented as a function of detuning from the exciton transition
energy at $B = 0$. Signals from both the σ^- and σ^+ exciton transitions are
seen. In Fig. 6.8(a) for L→R propagation, the σ^- dip is dominant, with
the σ^+ dip ∼10 times weaker. Complementary behaviour is observed for
R→L propagation in Fig. 6.8(b): σ^+ is the dominant transition, ∼2.5 times
stronger than σ^-. Contrast ratios in transmission between the σ^- and σ^+

components for propagation from L→R (R→L) are found to be −0.79 (0.45), indicating a strong left/right asymmetry between the coupling rates, with the dominant component switching upon changing propagation direction. This strong non-reciprocity in the transmission and PL data is in agreement with the theoretical results shown in Fig. 6.12.

6.4.2 Reflection Results

Figures 6.9(a) and 6.9(b) present results obtained in the reflection geometry. In Fig. 6.9(a), the resonant excitation field is input from the left Bragg coupler with the signal being detected from the same coupler. In contrast to the transmission experiment of Fig. 6.8(a), a stronger peak is seen for the more weakly coupled, σ^+, with only a weak feature for the more strongly coupled, σ^-. The reverse is true when the excitation is coupled into the left propagating mode, as in 6.9(b).

The predominance of the reflection signal from the spin that couples only weakly to the incoming mode is, at first, rather surprising: one might think that the QD transition coupled most strongly to the mode would show the strongest reflection. This would certainly be true for a chiral QD in transmission, but it is not the expected behaviour for a chirally-coupled QD in reflection. As explained in section 6.2, the reflected signals are expected to have equal strengths at low powers and then the less well coupled transition is expected to dominate at higher powers. The low-power regime is characterised by the balancing of the stronger coupling to the laser with weak back-scatter coupling, and vice versa, while the high-power regime has the strongly coupled transition saturating. In our experiments it was not possi-

ble to collect reflection data in the low power regime, due to the impractical integration times that would be required, and the results presented in Figs 6.9(a) and 6.9(b) were acquired when partial saturation of the QD was occurring. The observed results are exactly what should be expected when partially saturating on QD component. See section 6.4.3
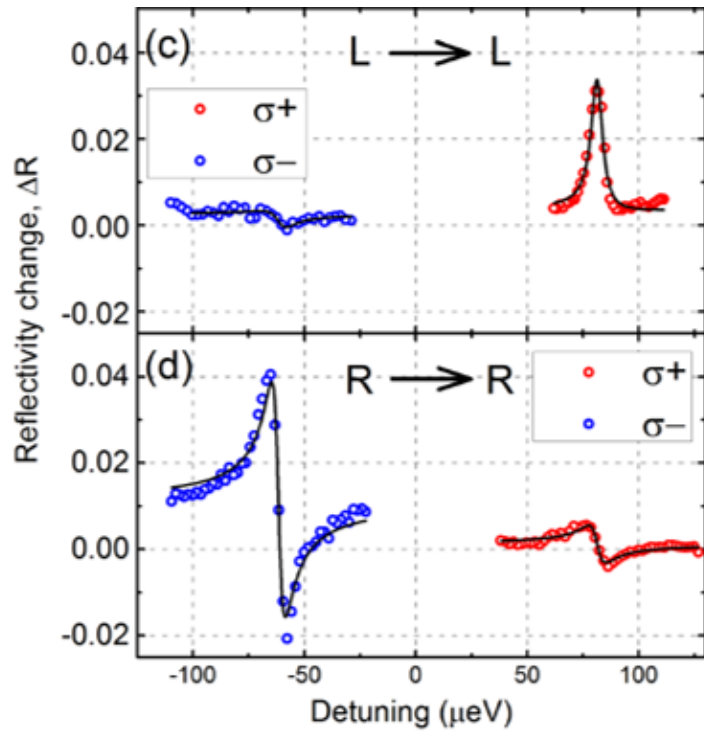
Figure 6.9: Differential reflectivity spectra for the chirally coupled QD at B = 1 T: (c) reflection change when resonant field is propagating towards the left; (d) reflection change when resonant field is propagating to the right.

6.4.3 Transmission Power Dependence

In order to compare the experimental results with the theoretical model to the data, the power levels between the two were related. This was done by performing a transmission power dependence on the more well coupled of the QD transitions, σ^+ in the R→L direction. See figure 6.10 for the experimental power dependence. Where the black trace, which used the lowest (5nW) power, shows the largest transmission dip. The magnitude of the dip is reduced with increasing excitation power. This is to be expected from a TLS as the QD can only interact with a single photon at any one time. Higher power means more photons are not interacting with the QD, reducing the size of the transmission dip as saturation is approached.

Figure 6.11 shows the power dependence of the transmission dip on resonance from the most highly coupled QD component, with the insert showing the experimental data. At powers below 10pW the transition dip is independent of excitation power as there is one photon or less impinging on the QD per lifetime. Then as the power is increased, the magnitude of the dip decreases as the QD is no longer able to interact with every photon. Above 10nW there is hardy any visible transmission dip as the QD has been saturated and scatters an insignificant amount of the excitation field.

In the experimental data there is little change in the transmission dip at 5nW and 20nW, but the change is more pronounced at higher powers. By comparing points on both the experiment and theoretical power dependencies it was possible to conclude that an experimental power of 50nW corresponds to a power within the waveguide of 100pW to 1nW. Comparing this power range to fig. 6.12, the green and yellow curves, the dominant transmission
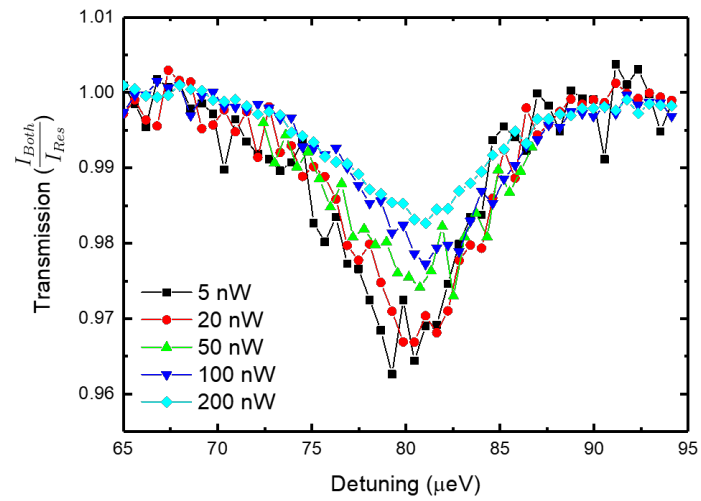
Figure 6.10: Transmission dip power dependence. The magnitude of the dip observed changes depending on the incident power. Powers between 5nW and 200nW were used.
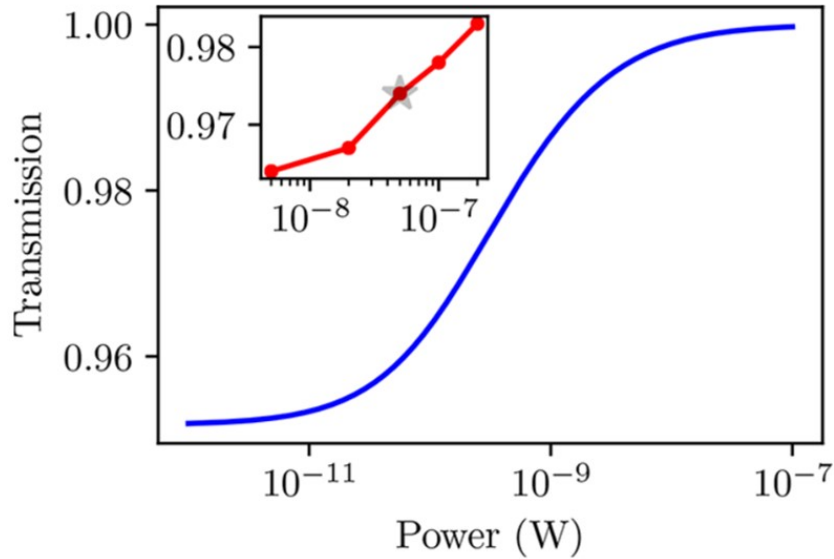
Figure 6.11: Plot showing the theoretical transmission through a waveguide as function of incident power. The inset shows the experimental data.

dip remains dominant during this range but the contasts start to drop. In the reflection an asstmmetry develops at these powers with the more weakly coupled component being stronger, see figure 6.13. The model qualitatively predicts the asymmetry measured in figure 6.9 due to the two components saturating at different powers.

6.4.4 Non-Chirally-Coupled Comparison

In the following section a QD that exhibits symmetric coupling to a waveguide will be subject to the same transmission and reflection experiments as presented above. This data will then be compared to the chiral coupling case.
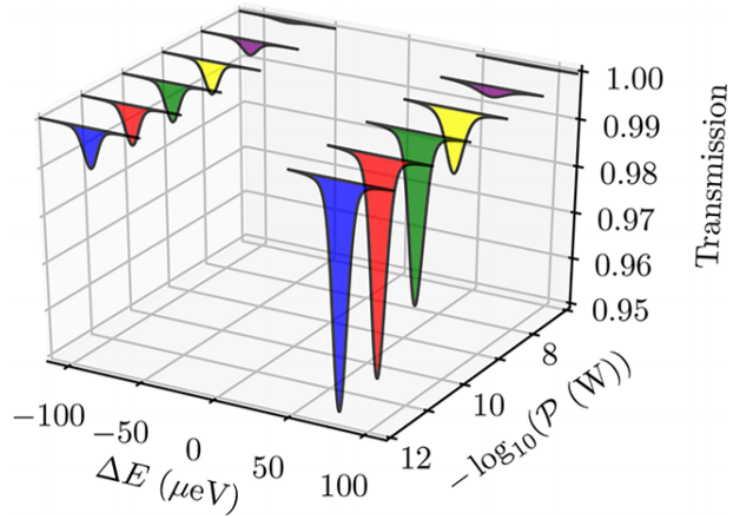
Figure 6.12: Calculated transmission of the system for a left to right propagating resonant field. Powers of 1, 10, and 100 pW are represented by blue, red and green curves respectively, with 1, 10, and 100 nW shown in yellow, purple and orange.
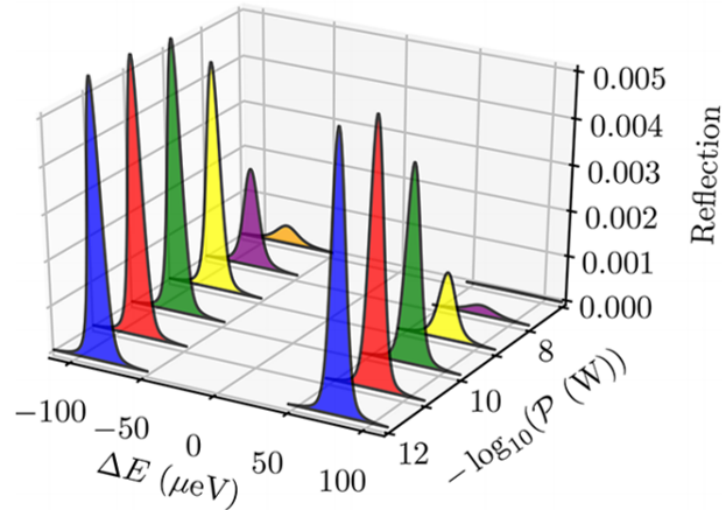
Figure 6.13: Calculated reflection of the system for reflection to the left. Powers of 1, 10, and 100pW are represented by blue, red and green curves respectively, with 1, 10, and 100 nW shown in yellow, purple and orange.

Non-chirally coupled PL

Non-resonant excitation was used to find a QD that was symmetrically cou-
pled to a waveguide. The random positioning of QDs within the nanobeam
means that some of them are positioned near non-chiral points at the centre
of the waveguides. These can be identified by near equal PL intensities for
the two Zeeman components at the Bragg couplers. Figure 4.13 shows PL
spectra collected from one such non-chirally coupled dot at B = 1 T. Two
Zeeman components are observed with very similar intensities. Their con-
trast ratio is ~ 0.02, as opposed to the values of -0.91 and 0.84 for the chiral
QD in Fig. 6.5.

Non-chirally coupled Transmission and Reflection

Figure 6.14 shows resonant transmission and reflectivity spectra for the same
QD with the laser incident from the left out-coupler. Similar resonant trans-
mission dip magnitudes are observed for both the σ^+ and σ^- transitions,
in strong contrast to Fig. 6.8. Similarly, near equal intensity Zeeman com-
ponents are observed in the reflection spectrum, which contrasts with the
results for the chirally-coupled QD in Fig. 6.9. These results confirm that
the asymmetry in the σ^+ and σ^- transitions seen in the transmission and
reflection data in figs. 6.8 and 6.9 originate from the chiral coupling between
the waveguide mode and the off-centre QD.

6.5 Discussion

Non-reciprocal transmission has been reported for a chirally coupled QD in a nano-photonic waveguide. The main experimental result is the observation of a reciprocity breaking spin-dependent transmission dip when in resonance with the QD, varying with the direction of propagation. These results are supported by a theoretical model of the system. The results observed in the reflection geometry, with the more weakly-coupled transition giving a larger signa, has been shown to be due to the partial saturation of the more-strongly coupled transition.

The results presented in this chapter may have uses in communication and QIP[152]. By integrating optical elements on-chip in a scalable geometry, devices such as optical diodes and circulators, operating at the single-photon level and switched by external laser control[125], and connected in circuits with other elements are a possibility as well as spin-based quantum networks[148], where quantum information is stored, manipulated and transmitted by QDs and photons.

6.6 Future Work

Further work with narrower-linewidth dots in charge-stabilised structures[142, 146] and with Purcell enhancement[142, 153], is expected to lead to larger dips in the transmission spectrum, enabling the power dependence in reflectivity to be investigated further. This would also approach the single photon limit, where ideally the photon can be deterministically imparted with a π-phase shift on transmission.
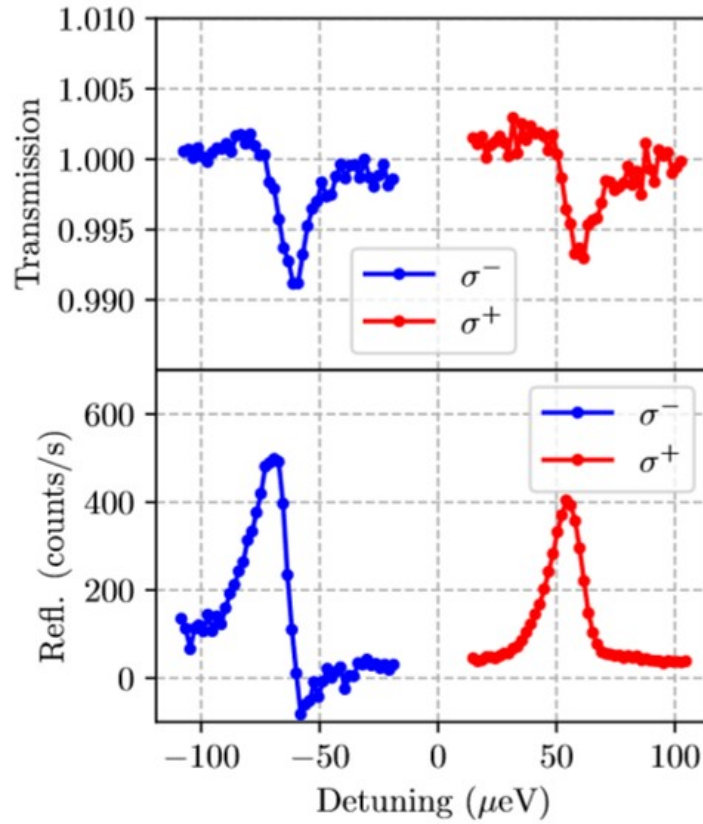
Figure 6.14: (a((b))) Spectrum showing resonant transmission (reflection) signal from a non-chirally coupled QD where the two Zeeman components have roughly equal amplitudes.

Chapter 7

Summary and Future Work

7.1 Summary

This thesis has presented and described a chiral interface between InAs QDs embedded within GaAs nanophotonic waveguides. Simulations and experiments have shown the breaking of reciprocity in these systems and how they may offer a future route to QIP applications.

Chapter 2 introduced the basic physical concepts and background information surrounding the use of QDs as embedded sources of single photons in III-V semiconductor circuits.

Chapter 3 detailed the computational methods used, as well as sample design, fabrication and experimental methods. This includes schematics of the experimental apparatus used for the experiments also.

7.1.1   Chapter 4: Spin to path conversion of QD excitons

Chapter 4 introduced directional emission from QDs embedded within nanophotonic waveguides, suspended nanobeam and W1 waveguides were used. Emission of opposite helicity components from QD exciton recombination were shown to couple to modes propagating in opposite directions if the QD was located at a C-point. The degree of directional emission depends on the QDs location within the waveguide. Comparing the nanobeam to a W1 revealed that the nanobeams had larger areas of high contrast, meaning that the restriction on QD position was not as high as the W1.

7.1.2   Chapter 5: Path to spin initialisation of QD excitons

Chapter 5 uses Quasi-resonant excitation to selectively excite components of a QD exciton. Here, opposite helicity components are excited depending on the propagation direction through the waveguide of the excitation field. The selective excitation is shown to arise due to the chiral interface between the QDs and the photonic environment. It has been shown that the selective excitation of a single QD spin component and the subsequent re-emission is directional.

7.1.3 Chapter 6: Resonant chiral interactions of QD excitons

Chapter 6 investigates the transmission of photons through a waveguide, when the photons are resonant with a chirally-coupled QD. Dips in the transmission is seen when on resonance with the QD transitions. The chiral interface causes an asymmetry in the transmission dips as opposite helicity components couple to modes propagating in opposite directions. A numerical model of the system gives good qualitative agreement with the results and explains the asymmetry observed in reflection measurements when none was expected.

7.2 Future Work

7.2.1 Waveguide optimisation

The waveguides used throughout this thesis were optimised to support a single mode to which a QD may couple. As shown in Chapter 4, the highly chiral areas in a standard W1 photonic waveguide are less than 1 per cent of the total waveguide area. One possible improvement is to perform a transflection operation to the standard W1 design. This will produce a Glide Plane Waveguide (GPW) as in figure 7.1. This breaks the symmetry of this system, leading to larger chiral areas. As well as an increase in the chiral areas GPWs should be able to achieve higher beta factors that the suspended nanobeams and enable the detection of larger dips in transmission. Changing the hole radii and centre positions may also allow the creation of a pho-

Figure 7.1: Schematic of a GPW design that will be fabricated.

tonic environment with larger chiral areas and using tapers between different waveguide designs may offer added benefits such as improved in-coupling, less loss throughout the circuit and greater extraction efficiencies.

7.2.2   Further integration of circuit elements

A chiral interface will arise in many photonic systems which confine light on the order of its wavelength. As such many devices are candidates to be used, such a microdisks, where a QD at a C-point would emit photons that would propagate around the disk in opposite directions depending on the photon polarisation. These photons could then be coupled out using evanescently coupled waveguides.

7.2.3   Multi-photon measurements

Registering multiple QDs

The QD registration technique briefly mentioned in chapter 4 could in theory be extended to the registration of several QDs with the aim of embedding them in a single device. By deterministically coupling QD spins, positioning QDs at chiral points, the emission direction can be controlled where QD emission will be directed and interact with the next QD in a spin dependent
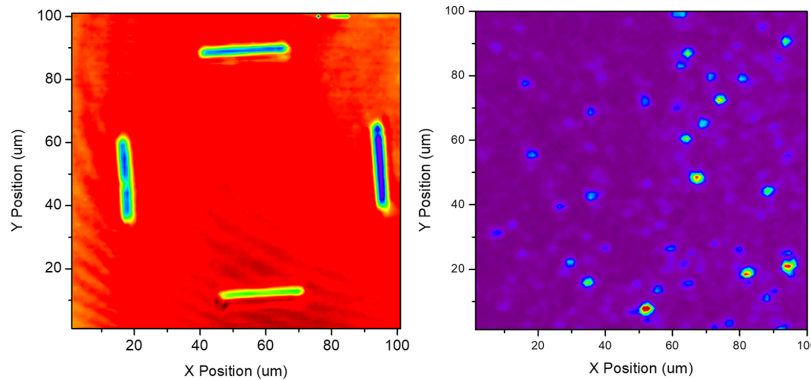
Figure 7.2: (left) Raster scan of a sample with etched makings to be used for QD position registration. (right) rasta scan showing emission from QDs between 900 and 900.25*nm*.

1-dimensional chain. Figure 7.2 shows early work on registering the positions of multiple QDs. The left image shows a raster scan of a $50\mu m$ x $50\mu m$ where a HeNe laser was scanned over the area. The 4 dark regions are etched and the drop in laser intensity identifies their position. The relative position of QDs can then be determined and structures can be fabricated around them. The right image shows QD PL from the same area where the signal is filtered so only emission between 900 and 900.25nm is shown. Ideally the QDs would be in resonance with each other but a small difference can hopefully be overcome by the use of electro-tuning with the use of diode structures.

Electro-tuning of QD emission wavelength

Once at least two QDs have been registered and positioned within a device their wavelengths may need tuning into resonance with each other. Using a diode structure, see section 3.3.3, enables a bias to be applied and the
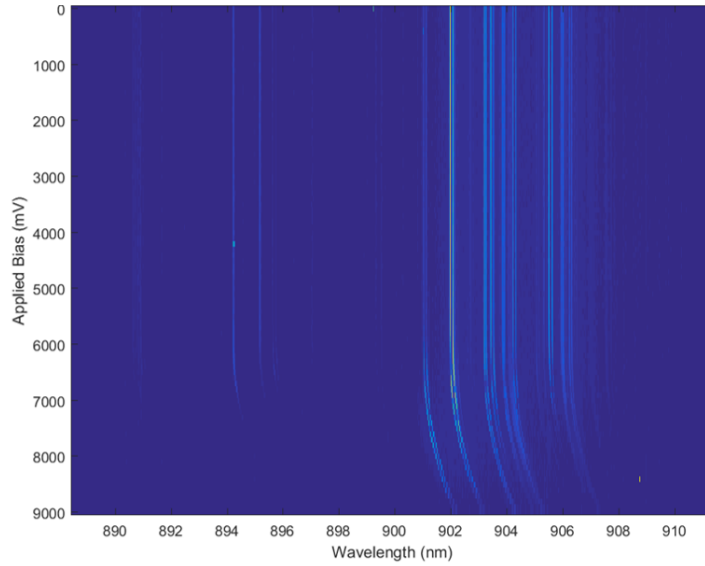
Figure 7.3: Voltage tuning of QDs located in waveguides on a diode sample.

emission wavelength of QDs can be tuned. Figure 7.3 shows an example of the emission wavelength of QDs changing once the applied bias is above $\sim 6V$. This device was not studied any further.

7.3   Conclusion

To conclude, this thesis has investigated the chiral interface that arises when quantum emitters are positioned at c-points of photonic waveguides. Nonresonant, quasiresonant and resonant techniques have been used to study this system. With the aims that the non-reciprocal nature of these systems may be used in future QIP applications.

Bibliography

[1] R. P. Feynman. Simulating physics with computers. *International journal of theoretical physics*, 21(467-488), 1982.

[2] P. W. Shor. Algorithms for quantum computation: Discrete logarithms and factoring. *in Foundations of Computer Science, 1994 Proceedings., 35th Annual Symposium*, (124-134), 1994.

[3] L. K. Grover. A fast quantum mechanical algorithm for database search. *in Proceedings of the twenty-eighth annual ACM symposium on Theory of computing*, (212-219), 1996.

[4] J. I. Cirac and P. Zoller. Quantum computations with cold trapped ions. *Physical Review Letters*, 74(4091), 1995.

[5] Y. Nakamura, Y. A. Pashkin, and J. S. Tsai. Coherent control of macroscopic quantum states in a single-cooper-pair box. *Nature*, 398(786-788), 1999.

[6] N. A. Gershenfeld and I. L. Chuang. Bulk spin-resonance quantum computation. *Science*, 275(350-356), 1997.

127

[7] C. H. W. Barnes, J. M. Shilton, and A. M. Robinson. Quantum computation using electrons trapped by surface acoustic waves. *Physical Review B*, 62(8410), 2000.

[8] T. D. Ladd, F. Jelezko, R. Laflamme, Y. Nakamura, C. Monroe, and J. L. O'Brien. Quantum computers. *Nature*, 464(45-53), 2010.

[9] J. L. O'Brien. Optical quantum computing. *Science*, 318(1567-1570), 2007.

[10] E. Knill, R. Laflamme, and G. J. Milburn. A scheme for efficient quantum computation with linear optics. *Nature*, 409(46-52), 2001.

[11] T. B. Pittman, M. J. Fitch, B. C. Jacobs, and J. D. Franson. Experimental controlled-not logic gate for single photons in the coincidence basis. *Physical Review A*, 68(032316), 2003.

[12] J. L. O'Brien, G. J. Pryde, A. G. White, T. C. Ralph, and D. Branning. Demonstration of an all-optical quantum controlled-NOT gate. *Nature*, 426(264-267), 2003.

[13] A. Politi, M. J. Cryan, J. G. Rarity, S. Yu, and J. L. O'Brien. Silica-on-silicon waveguide quantum circuits. *Science*, 320(646-649), 2008.

[14] M. A. Pooley, D. J. P. Ellis, R. B. Patel, A. J. Bennett, K. H. A. Chan, I. Farrer, D. A. Ritchie, and A. J. Shields. Controlled-not gate operating with single photons. *Applied Physics Letters*, 100(211103), 2012.

[15] J. L. O'Brien, A. Furusawa, and J. Vuckovic. Photonic quantum technologies. *Nature Photonics*, 3(687-695), 2009.

[16] S. Barz, E. Kashefi, A. Broadbent, J. F. Fitzsimons, A. Zeilinger, and P. Walther. Demonstration of blind quantum computing. *Science*, 335(303-308), 2012.

[17] H. J. Kimble. The quantum internet. *Nature*, 453(1023-1030), 2008.

[18] J. K. S. Poon. Integrated ultra-low-loss resonator on a chip. *Nature*, 12(255-256), 2018.

[19] M. A. Nielsen and I. L. Chuang. *Quantum Computation and Quantum Information*. Cambridge University Press, 2011.

[20] D. P. DiVincenzo. The physical implementation of quantum computation. *Fortschritte der Physik*, 48(771-783), 2000.

[21] Y. Benny, S. Khatsevich, Y. Kodriano, E. Poem, R. Presman, D. Galushko, P. M. Petroff, and D. Gershoni. Coherent Optical Writing and Reading of the Exciton Spin State in Single Quantum Dots. *Physical Review Letters*, 106(040504), 2011.

[22] J. D. Joannopoulos, S. G. Johnson, J. N. Winn, and R. D. Meade. *Photonic Crystals: Molding the Flow of Light*. Princeton University Press, 2008.

[23] A. Greilich, D. R. Yakovlev, A. Shabaev, Al. L. Efros, I. A. Yugova, R. Oulton, V. Stavarache, D. Reuter, A. Wieck, and M. Bayer. Mode

Locking of Electron Spin Coherences in Singly Charged Quantum dots. *Science*, 313(341), 2006.

[24] D. Brunner, B. D. Geradot, P. A. Dalgarno, G. Wust, K. Karrai, N. G. Stoltz, P. M. Petroff, and R. J. Warburton. A Coherent Single-Hole Spin in a Semiconductor. *Science*, 325(70), 2009.

[25] P. Borri, W. Langbein, S. Schneider, U. Woggon, R. L. Sellin, D. Ouyang, and D. Bimberg. Ultralong Dephasing Time in InGaAs Quantum Dots. *Physical Review Letters*, 87(15), 2001.

[26] A. K. Ekert. Quantum cryptography based on bell's theorem. *Physical Review Letters*, 67(661), 1991.

[27] H. Inamori, N. Lutkenhaus, and D. Mayers. Unconditional security of practical quantum key distribution. *The European Physical Journal D*, 41(599-627), 2007.

[28] B. Lounis and M. Orrit. Single-photon sources. *Reports on Progress in Physics*, 68(1129-1179), 2005.

[29] C. Santori, D. Fattal, J. Vuckovic, G. S. Solomon, and Y. Yamamoto. Indistinguishable photons from a single-photon device. *Nature*, 419(594-597), 2002.

[30] R. Seguin, A. Schliwa, S. Rodt, K. Potschke, U. W. Pohl, and D. Bimberg. Size-dependent fine-structure splitting in self-organised inas/gaas quantum dots. *Physical Review Letters*, 95(257402), 2005.

[31] A. Drabenstedt, L. Fleury, C. Tietz, F. Jelezko, S. Kilin, A. Nizovtzev, and J. Wrachtrup. Low-temperature microscopy and spectroscopy on single defect centers in diamond. *Physical Review B*, 60(11503), 1999.

[32] T. Wilk, S. C. Webster, A. Kuhn, and G. Rempe. Single-Atom Single-Photon Quantum Interface. *Science*, 317(5837), 2007.

[33] D. Gammon, E. S. Snow, B. V. Shanabrook, D. S. Katzer, and D. Park. Fine structure splitting in the optical spectra of single gaas quantum dots. *Physical Review Letters*, 76(16), 1996.

[34] L. Zhang, Y-J. Yu, L-G. Chen, Y. Luo, B. Yang, F-F. Kong, G. Chen, Y. Zhang, Q. Zhang, Y. Luo, J-L. Yang, Z-C. Dong, and J. G. Hou. Electrically driven single-photon emission from an isolated single molecule. *Nature Communications*, 8(580), 2017.

[35] M. A. Reed. Spatial quantization in GaAs-AlGaAs multiple quantum dots. *Journal of Vacuum Science & Technology B: Microelectronics and Nanometer Structures*, 4(358), 1986.

[36] D. Leonard, M. Krishnamurthy, C. M. Reaves, S. P. Denbaars, and P. M. Petroff. Direct formation of quantum-sized dots from uniform cogerent islands of InGaAs on GaAs surfaces. *Applied Physics Letters*, 63(3203-3205), 1993.

[37] J. Y. Marzin, J. M. Gerard, A. Izrael, D. Barrier, and G. Bastard. Photoluminescence of Single InAs Quantum Dots Obtained by Self-Organised Growth on GaAs. *Physical Review Letters*, 73(716-719), 1994.

[38] B. Lounis, H. Bechtel, D. Gerion, P. Alivisatos, and W. Moerner. Photon antibunching in single CdSe/ZnS quantum dot flourescence. *Chemical Physics Letters*, 329(399-404), 2000.

[39] G. Chen, T. H. Stievater, E. T. Batteh, X. Li, D. G. Steel, D. Gammon, D. S. Katzer, D. Park, and L. J. Sham. Biexciton quantum coherence in a single quantum dot. *Physical Review Letters*, 88(117901), 2002.

[40] W. Izumida, O. Sakai, and S. Tarucha. Tunneling through a quantum dot in local spin singlet-triplet crossover region with Kondo effect. *Physical Review Letters*, 87(216803), 2001.

[41] Q. Xie, A. Madhukar, P. Shen, and N. Kobayashi. Vertically Self-Organised InAs Quantum Box Islands on GaAs(100). *Physical Review Letters*, 75(2542-2545), 1995.

[42] P. Michler, A. Kiraz, C. Becher, W. V. Schoenfeld, P. M. Petroff, L. Zhang, E. Hu, and A. İmamoğlu. A Quantum Dot Single-Photon Turnstile Device. *Science*, 290(2282-2285), 2000.

[43] V. Zwiller, H. Blom, P. Jonsson, N. Panev, S. Jeppesen, T. Tsegaye, E. Goobar, M. E. Pistol, L. Samuelson, and G. Björk. Single quantum dots emit single photons at a time: Antibunching experiments. *Applied Physics Letters*, 78(2476), 2001.

[44] Z. Yuan, B. E. Kardynal, R. M. Stevenson, A. J. Shields, C. J. Lobo, K. Cooper, N. S. Beattie, D. A. Ritchie, and M. Pepper. Electrically Driven Single-Photon Source. *Science*, 295(102-105), 2002.

[45] M. Pelton, C. Santori, J. Vučković, B. Zhang, G. S. Solomon, J. Plant, and Y. Yamamoto. Efficient Source of Single Photons: A Single Quantum Dot in a Micropost Microcavity. *Physical Review Letters*, 89(233602), 2002.

[46] C. Santori, D. Fattal, J. Vučković, G. S. Solomon, and Y. Yamamoto. Single-photon generation with InAs quantum dots. *New Journal of Physics*, 6(89), 2004.

[47] W. H. Chang, W. Y. Chen, H. S. Chang, T. P. Hsieh, J. I. Chyi, and T. M. Hsu. Efficient Single-Phton Sources Based on Low-Density Quantum Dots in Photonic-Crystal Nanocavities. *Physical Review Letters*, 96(117401), 2006.

[48] S. Strauf, N. G. Stoltz, M. T. Rakher, L. A. Coldren, P. M. Petroff, and D. Bouwmeester. High-frequency single-photon source with polarization control. *Nature Photonics*, 1(704-708), 2007.

[49] K. Sebald, P. Michler, T. Passow, D. Hommel, G. Bacher, and A. Forchel. Single-photon emission of CdSe quantum dots at temperatures up to 200K. *Applied Physics Letters*, 81(2920-2922), 2002.

[50] F. Tinjod, B. Gilles, S. Moehl, K. Kheng, and H. Mariette. II-VI quantum dot formation induced by surface energy change of a strained layer. *Applied Physics Letters*, 82(4340-4342), 2003.

[51] K. Brunner. Si/Ge nanostructures. *Reports on Progress in Physics*, 65(27), 2002.

[52] A. P. Alivisatos. Semiconductor cluster , nanocrystals and quantum dots. *Science*, 271(933), 1996.

[53] S. Guha, A. Madhukar, and K. C. Rajkumar. Onset of incoherency and defect introduction in the initial stages of molecular beam epitaxical growth og highly strained $In_xGa_{1-x}As$ on GaAs(100). *Applied Physics Letters*, 57(2110), 1990.

[54] G. A. Narvaez, G. Bester, and A. Zunger. Dependence of the electronic structure of self-assembled (In, Ga)As/GaAs quantum dots on height and composition. *Journal of Applied Physics*, 98(043708), 2005.

[55] W. Sheng and J. P. Leburton. Electron-hole alignment in InAs/GaAs self-assembled quantum dots: Effects of chemical composition and dot shape. *Physical Review B*, 63(161301), 2001.

[56] A. Milnes and A. Polyakov. Indium arsenide: a semiconductor for high speed and electro-optical devices. *Materials Science and Engineering: B*, 18(237-259), 1993.

[57] A. Zrenner. A close look on single quantum dots. *The Journal of Chemical Physics*, 112(7790), 2000.

[58] T. Ihara. Biexciton cascade emission reveals absolute absorption cross section of single semiconductor nanocrystals. *Physical Review B*, 93(235442), 2016.

[59] O. Benson, C. Santori, M. Pelton, and Y. Yamamoto. Regulated and entangled photons from a single quantum dot. *Physical Review Letters*, 84(2513), 2000.

[60] R. M. Stevenson, R. J. Young, P. Atkinson, K. Cooper, D. A. Ritchie, and A. J. Shields. A semiconductor source of triggered entangled photon pairs. *Nature*, 439(179-182), 2006.

[61] A. J. Hudson, R. M. Stevenson, A. J. Bennett, R. J. Young, C. A. Nicoll, P. Atkinson, K. Cooper, D. A. Ritchie, and A. J. Shields. Coherence of an Entangled Exciton-Photon State. *Physical Review Letters*, 99(266802), 2007.

[62] M. Ward, M. Dean, R. M. Stevenson, A. J. Bennett, D. Ellis, K. Cooper, I. Farrer, C. A. Nicoll, D. A. Ritchie, and A. J. Shields. Coherent dynamics of a telecom-wavelength entangled photon source. *Nature Communications*, 5(3316), 2014.

[63] R. Thompson, R. Stevenson, A. Shields, I. Farrar, C. Lobo, D. Ritchie, M. Leadbeater, and M. Pepper. Single-photon emission from exciton complexes in individual quantum dots. *Physical Review B*, 64(201302), 2001.

[64] D. A. B. Miller, D. S. Chemla, T. C. Damen, A. C. Gossard, W. Wiegmann, T. H. Wood, and C. A. Burrus. Band-Edge Electroabsorption in Quantum Well Structures: The Quantum-Confined Stark Effect. *Physical Review Letters*, 53(2173), 1984.

[65] A. J. Bennett, R. B. Patel, J. Skiba-Szymanska, C. A. Nicoll, I. Farrer, D. A. Ritchie, and A. J. Shields. Giant Stark effect in the emisson of single semiconductor quantum dots. *Applied Physics Letters*, 97(031104), 2010.

[66] R. B. Patel, A. J. Bennett, I. Farrer, C. A. Nicoll, D. A. Ritchie, and A. J. Shields. Two-photon interference of the emission from electrically tunable remote quantum dots. *Nature Photonics*, 4(632-635), 2010.

[67] P. Lodahl, S. Mahmoodian, and S. Stobbe. Interfacing single photons and single quantum dots with photonic nanostructures. *Reviews of Modern Physics*, 87(347), 2015.

[68] E. M. Purcell. Spontaneous emission probabilities at radio frequencies. *Physical Review B*, 69(681), 1946.

[69] E. T. Jaynes and F. W. Cummings. Comparison of quantum and semi-classical radiation theories with application to the beam maser. *Proceedings of the IEEE*, 51(89-109), 1963.

[70] I. I. Rabi. Space quantization in a gyrating magnetic field. *Physical Review*, 51(652), 1937.

[71] J. Hopfield. Theory of the contribution of excitons to the complex dielectric constant of crystals. *Physical Review*, 112(5), 1958.

[72] A. Kiraz, P. Michler, C. Becher, B. Gayral, A. İmamoğlu, L. Zhang, E. Hu, W. V. Schoenfeld, and P. M. Petroff. Cavity-quantum electrodynamics using a single InAs quantum dot in a microdisk structure. *Applied Physics Letters*, 78(3932-3934), 2001.

[73] T. Yoshie, A. Scherer, J. Hendrickson, G. Khitrova, H. M. Gibbs, G. Rupper, C. Ell, O. B. Shchekin, and D. G. Deppe. Vacuum Rabi splitting with a single quantum dot in a photonic crystal nanocavity. *Nature*, 432(200-203), 2004.

[74] J. P. Reithmaier, G. Sęk, A. Löffler, C. Hofmann, S. Kuhn, S. Reitzenstein, L. V. Keldysh, V. D. Kulakovskii, T. L. Reinecke, and A. Forchel. Strong coupling in a single quantum dot-semiconductor microcavity system. *Nature*, 432(197-200), 2004.

[75] K. Hennessy, A. Badolato, M. Winger, D. Gerace, M. Atatüre, S. Gulde, S. Fält, E. L. Hu, and A. İmamoğlu. Quantum nature of a strongly coupled single quantum dot-cavity system. *Nature*, 445(896-899), 2007.

[76] E. Yablonovitch. Inhibited spontaneous emission in solid-state physics and electronics. *Physical Review Letters*, 58(2059), 1987.

[77] S. John. Strong localization of photons in certain disordered dielectric superlattices. *Physical Review Letters*, 58(2486), 1987.

[78] D. Broxtermann, M. Sivis, J. Malindretos, and A. Rizzi. Mbe growth of high electron mobility 2degs in algan/gan heterostructures controlled by rheed. *AIP Advances*, 2(012108), 2012.

[79] A. Cho and J. Aurthur. Molecular beam epitaxy. *Progress in solid state chemistry*, 10(157-191), 1975.

[80] R. Asaro and W. Tiller. Interface morphology development during stress corrosion cracking: Part i. via surface diffusion. *Metallurgical Transactions*, 3(1789-1796), 1972.

[81] A. Danescu. The asaro-tiller-grinfeld instability revisited. *International Journal of Solids and Structures*, 38(4671-4684), 2001.

[82] P. M. Fauchet. Light emission from si quantum dots. *Materials Today*, 8(1), 2005.

[83] S. Golka, M. Arens, M. Reetz, and T. Kwapien. Time-multiplexed, inductively coupled plasma process with seperate $SiCl_4$ and O_2 steps for etching of GaAs with high selectivity. *Journal of Vacuum Science and Technology B, Nanotechnology and Microelectronics: Materials, Processing, Measurement and Phenomena*, 27(2270), 2005.

[84] A. Cohen. Critical point drying. Principles and procedures. *Scanning electron microscopy*, (303-324), 1979.

[85] R. Heitz, M. Veit, N. N. Ledentsov, A. Hoffmann, D. Bimberg, V. M. Ustinov, P. S. Kopev, and Z. I. Alferov. Energy relaxation by multiphoton processes in InAs/GaAs quantum dots. *Physical Review B*, 65(10435), 1997.

[86] N. H. Bonadeo, J. Erland, D. Gammon, D. Park, D. Katzer, and D. Steel. Coherent optical control of the quantum state of a single quantum dot. *Science*, 282(1473-1476), 1998.

[87] S. Sauvage, P. Boucaud, R. Lobo, F. Bras, G. Fishman, R. Prazeres, F. Glotin, J. Ortega, and J.-M. Gerard. Long polaron lifetime in InAs/GaAs self-assembled quantum dots. *Physical Review Letters*, 88(177402), 2002.

[88] E. Zibik, L. Wilson, R. Green, G. Bastard, R. Ferreira, P. Phillips, D. Carder, J. R. Wells, M. Skolnick, J. Cockburn, M. J. Steer, and M. Hopkinson. The polaronic nature of intraband relaxation in

InAs/GaAs quantum dots. *Physica E: Low-dimensional Systems and Nanostructures*, 26(408-412), 2005.

[89] K. Kuroda, T. Kuroda, K.Watanabe, T. Mano, K. Sakoda, G. Kido, and N. Koguchi. Final-state readout of exciton qubits by observing resonantly excited photoluminescence in quantum dots. *Applied Physics Letters*, 90(051909), 2007.

[90] A. Muller, E. B. Flagg, P. Bianucci, X. Y. Wang, D. G. Deppe, W. Ma, J. Zhang, G. J. Salamo, M. Xiao, and C. K. Shih. Resonance Fluorescence from a Coherently Driven Semiconductor Quantum Dot in a Cavity. *Physical Review Letters*, 99(187402), 2007.

[91] E. Siebert, T. Warming, A. Schliwa, E. Stock, M. Winkelnkemper, S. Rodt, and D. Bimberg. Spectroscopic access to single-hole energies in inas/gaas quantum dots. *Physical Review B*, 79(205321), 2009.

[92] T. Warming, E. Siebert, A. Schliwa, E. Stock, R. Zimmermann, and D. Bimberg. Hole-hole and electron-hole exchange interactions in single inas/gaas quantum dots. *Physical Review B*, 79(125316), 2009.

[93] Y. Benny, Y. Kodriano, E. Poem, D. Gershoni, T. A. Truong, and P. M. Petroff. Excitation spectroscopy of single quantum dots at tunable positive, neutral and negative charge states. *Physical Review B*, 86(085306), 2012.

[94] F. Grazioso, B. R. Patton, and J. M. Smith. A high stability beam-scanning confocal optical microscope for low temperature operation. *Review of Scientific Instruments*, 81(093705), 2010.

[95] N. Prtljaga, R. J. Coles, J. O'Hara, B. Royall, E. Clarke, A. M. Fox, and M. S. Skolnick. Monolithic integration of a quantum emitter with a compact on-chip beam-splitter. *Applied Physics Letters*, 104(231107), 2014.

[96] P. Kok and B. W. Lovett. *Introduction to Optical Quantum Information Processing.* Cambridge University Press, 2010.

[97] S. D. Barret and P. Kok. Efficient high-fidelity quantum computing using matter qubits and linear optics. *Physical Review A*, 71(060310), 2005.

[98] F. J. Rodríguez-Fortuão, G. Marino, P. Ginzburg, D. O'Connor, A. Martínez, G. A. Wurtz, and A. V. Zayats. Near-field interference for the unidirectional excitation of electromagnetic guided modes. *Science*, 340(328-330), 2013.

[99] C. Junge, D. O'Shea, J. Volz, and A. Rauschenbeutel. Strong coupling between single atoms and nontransversal photons. *Physical Review Letters*, 110(213604), 2013.

[100] R. Mitsch, C. Sayrin, B. Albrecht, P. Schneeweiss, and A. Rauschenbeutel. Quantum state-controlled directional spontaneous emission of photons into a nanophotonic waveguide. *Nature Communications*, 5(5713), 2014.

[101] J. Petersen, J. Volz, and A. Rauschenbeutel. Chiral nanophotonic waveguide interface based on spin-orbit interaction of light. *Science*, 346(67-71), 2014.

[102] B. le Ferber, N. Rotenberg, and L. Kuipers. Nanophotonic control of circular dipole emission. *Nature Communications*, 6(6695), 2015.

[103] K. Y. Bliokh, F. J. Rodríguez-Fortuão, F. Nori, and A. V. Zayats. Spin-orbit interactions of light. *Nature Photonics*, 9(796-808), 2015.

[104] I. J. Luxmoore, N. A. Wasley, A. J. Ramsey, A. C. T. Thijssen, R. Oulton, M. Hugues, S. Kasture, V. G. Achanta, A. M. Fox, and M. S. Skolnick. Interfacing spins in an ingaas quantum dot to a semiconductor waveguide circuit using emitted photons. *Physical Review Letters*, 110(037402), 2013.

[105] I. Sollner et al. Deterministic photon-emitter coupling in chiral photonic circuits. *Nature Nanotechnology*, 10(775-778), 2015.

[106] A. B. Young, A. C. T. Thijssen, D. M. Beggs, P. Androvitsaneas, L. Kuipers, J. G. Rarity, S. Hughes, and R. Oulton. Polarization engineering in photonic crystal waveguides for spin-photon entanglers. *Physical Review Letters*, 115(153901), 2015.

[107] S. M. Thon, M. T. Rakher, H. Kim, J. Gudat, W. T. M. Irvine, P. M. Petroff, and D. Bouwmeester. Strong coupling through optical positioning of a quantum dot in a photonic crystal cavity. *Applied Physics Letters*, 94(111115), 2009.

[108] A. Dousse, L. Lanco, J. Suffczyński, E. Semenova, A. Miard, A. Lemaítre, I. Sagnes, C. Roblin, J. Bloch, and P. Senellart. Controlled light-matter coupling for a single quantum dot embedded in a

pillar microcavity using far-field optical lithography. *Physical Review Letters*, 101(267404), 2008.

[109] Lumerical FDTD Solutions. Lumerical solutions, inc, 2014.

[110] S. S. Johnson and J. J. Joannopoulos. Block-iterative frequency-domain methods for maxwell's equations in a plane wave basis. *Optics Express*, 8(173-190), 2001.

[111] N. A. Wasley, I. J. Luxmoore, R. J. Coles, E. Clarke, A. M. Fox, and M. S. Skolnick. Disorder-limited photon propagation and anderson-localization in photonic crystal waveguides. *Applied Physics Letters*, 101(051116), 2012.

[112] A. Faraon, I. Fushman, D. Englund, N. Stoltz, P. Petroff, and J.Vuckovic. Dipole induced transparency in waveguide coupled photonic crystal cavities. *Optics Express*, 16(12154), 2008.

[113] M. Bayer, G. Ortner, O. Stern, A. Kuther, A. A. Gorbunov, A. Forchel, P. Hawrylak, S. Fafard, K. Hinzer, T. L. Reinecke, S. N. Walck, J. P. Reithmaier, F. Klopf, and F. Schäfer. Fine structure of neutral and charged excitons in self-assembled in(ga)as/(al)gaas quantum dots. *Physical Review B*, 65(195315), 2002.

[114] A. Kuther, M. Bayer, A. Forchel, A. Gorbunov, V. B. Timofeev, F. Schäfer, , and J. P. Reithmaier. Zeeman splitting of excitons and biexcitons in single in0.60ga0.40as/gaas self-assembled quantum dots. *Physical Review B*, 58(R7508(R)), 1998.

[115] M. Bayer, A. Kuther, A. Forchel, A. Gorbunov, V. B. Timofeev, F. Schäfer, J. P. Reithmaier, T. L. Reinecke, and S. N. Walck. Electron and hole g factors and exchange interaction from studies of the exciton fine structure in in0.60ga0.40as quantum dots. *Physical Review Letters*, 82(1748), 1999.

[116] J. J. Finley, D. J. Mowbray, M. S. Skolnick, A. D. Ashmore, C. Baker, A. F. G. Monte, and M. Hopkinson. Fine structure of charged and neutral excitons in inas-al0.6ga0.4as quantum dots. *Physical Review B*, 66(153316), 2002.

[117] P. Stepanov, A. Delga, X. Zang, J. Bleuse, E. Dupuy, E. Peinke, P. Lalanne, J-M. Gérard, and J. Claudon. Quantum dot spontaneous emission control in a ridge waveguide. *Applied Physics Letters*, 106(041112), 2015.

[118] P. Tighineanu, A. S. Sørensen, S. Stobbe, and P. Lodahl. Unraveling the mesoscopic character of quantum dots in nanophotonics. *Physical Review Letters*, 114(247401), 2015.

[119] A. Delteil, Z. Sun, W. b. Gao, E. Togan, S. Faelt, and A. Imamoglu. Generation of heralded entanglemaent between distant hole spins. *Nature Physics*, 12(218-223), 2016.

[120] R. J. Warburton. Single spins in self-assembled quantum dots. *Nature materials*, 12(483), 2012.

[121] T. Ramos, B. Vermersch, P. Hauke, H. Pichler, and P. Zoller. Non-markovian dynamics in chiral quantum networks with spins and photons. *Physical Review A*, 93(062104), 2016.

[122] B. Vermersch, T. Ramos, P. Hawke, and P. Zoller. Implementation of chiral quantum optics with rydberg and trapped-ion setups. *Physical Review A*, 93(063830), 2016.

[123] R. J. Coles, D. M. Price, B. Royall, E. Clarke, M. S. Skolnick, A. M. Fox, and M. N. Makhonin. Path-dependent initialization of a single quantum dot exciton spin in a nanophotonic waveguide. *Physical review B*, 95(121401(R)), 2017.

[124] R. J. Coles, D. M. Price, J. E. Dixon, B. Royall, E. Clarke, P. Kok, M. S. Skolnick, A. M. Fox, and M. N. Makhonin. Chirality of nanophotonic waveguide with embedded quantum emitter for unidirectional spin transfer. *Nature Communications*, 7(11183), 2016.

[125] P. Lodahl, S. Mahmoodian, S. Stobbe, P. Schneeweiss, J. Volz, A. Rauschenbeutal, H. Pichler, and P. Zoller. Chiral quantum optics. *Nature*, 541(473-480), 2017.

[126] I. J. Luxmoore, N. A. Wasley, A. J. Ramsey, A. C. T. Thijssen, R. Oulton, M. Hugues, A. M. Fox, and M. S. Skolnick. Optical control of the emission direction of a quantum dot. *Applied Physics Letters*, 103(241102), 2013.

[127] F. J. Rodríguez-Fortuão, I. Barber-Sanz, D. Puerto, A. Griol, and A. Martinez. Resolving light handedness with an on-chip silicon microdisk. *ACS Photonics*, 1(762), 2014.

[128] E. Poem, Y. Kodriano, C. Tradonsky, B. D. Geradot, P. M. Petroff, and D. Gershoni. Radiative cascades from charged semiconductor quantum dots. *Physical Review B*, 81(085306), 2010.

[129] R. J. Warburton, C. Schaflein, D. Haft, F. Bickel, A. Lorke, K. Karrai, J. M. Garcia, W. Schoenfeld, and P. M. Petroff. Optical emission from a charge-tunable quantum ring. *Nature*, 405(926-929), 2000.

[130] M. N. Makhonin, J. E. Dixon, R. J. Coles, B. Royall, I. J. Luxmoore, E. Clarke, M. Hugues, M. S. Skolnick, and A. M. Fox. Waveguide coupled resonance fluorescence from on-chip quantum emitter. *Nano Letters*, 14(12)(6997-7002), 2014.

[131] M. Kroner, A. O. Govorov, S. Remi, B. Biedermann, S. Seidl, A. Badolato, P. M. Petroff, W. Zhang, R. Barbour, B. D. Gerardot, R. J. Warburton, and K. Karrai. The nonlinear Fano effect. *Nature*, 451(311-314), 2008.

[132] T. M. Godden, J. H. Quilter, A. J. Ramsay, Yanwen Wu, P. Brereton, S. J. Boyle, I. J. Luxmoore, J. Puebla-Nunez, A. M. Fox, and M. S. Skolnick. Coherent Optical Control of the Spin of a Single Hole in an InAs/GaAs Quantum Dot. *Physical Review Letters*, 108(017402), 2012.

[133] C. De Greve, P. L. McMahon, D. Press, T. D. Ladd, D. Bisping, C. Schneider, M. Kamp, L. Worschech, S. Hofling, A. Forchel, and Y. Yamamoto. Ultrafast coherent control and suppressed nuclear feedback of a single quantum dot hole qubit. *Nature Physics*, 7(872-878), 2010.

[134] A. J. Brash, L. M. P. P. Martins, F. Liu, J. H. Quilter, A. J. Ramsay, M. S. Skolnick, and A. M. Fox. High-fidelity initialization of long-lived quantum dot hole spin qubits by reduced fine-structure splitting. *Physical Review B*, 92(121301(R)), 2015.

[135] A. Boyer de la Giroday, A. J. Bennett, M. A. Pooley, R. M. Stevenson, N. Sköld, R. B. Patel, I. Farrer, D. A. Ritchie, and A. J. Shields. All-electrical coherent control of the exciton states in a single quantum dot. *Physical Review B*, 82(241301(R)), 2010.

[136] Y. Cao, A. J. Bennett, I. Farrer, D. A. Ritchie, and A. J. Shields. Polarization-correlated photons from a positively charged quantum dot. *Physical Review B*, 92(081302(R)), 2015.

[137] E. A. Chekhovich, M. N. Makhonin, A. I. Tartakovskii, A. Yacoby, H. Bluhm, K. C. Nowack, and L. M. K. Vandersypen. Nuclear spin effects in semiconductor quantum dots. *Nature Materials*, 12(494-504), 2013.

[138] D. E. Chang, V. Vuletić, and M. D. Lukin. Quantum nonlinear optics - photon by photon. *Nature Photonics*, 8(685-694), 2014.

[139] S. Fan, S. E. kocabaŞ, and J.-T. Shen. Input-output formalism for few-photon transport in one-dimensional nanophotonic waveguides coupled to a qubit. *Physical Review A*, 82(063821), 2010.

[140] H. Zheng, D. J. Gauthier, and H. U. Baranger. Waveguide QED: Many-body bound-state effects in coherent and Fock-state scattering from a two-level system. *Physical Review A*, 82(063816), 2010.

[141] A. Javadi, I. Söllner, M. Arcari, S. L. Hansen, L. Midolo, S. Mahmoodian, G. Kiršanskė, T. Pregnolato, E. H. Lee, J. D. Song, S. Stobbe, and P. Lodahl. Single-photon non-linear optics with a quantum dot in a waveguide. *Nature Communications*, 6(8655), 2015.

[142] D. Hallett, A. P. Foster, D. L. Hurst, B. Royall, P. Kok, E. Clarke, I. E. Itskevich, A. M. Fox, M. S. Skolnick, and L. R. Wilson. Electrical control of nonlinear quantum optics in a nano-photonic waveguide. *arXiv:1711.00682v2*, 2017.

[143] A. Sipahigil, R. E. Evans, D. D. Sukachev, M. J. Burek, J. Borregaard, M. K. Bhaskar, C. T. Nguyen, J. L. Pacheco, H. A. Atikian, C. Meuwly, R. M. Camacho, F. Jelezko, E. Bielejec, H. Park, M. Lončar, and M. D. Lukin. An integrated diamond nanophotonics platform for quantum-optical networks. *Science*, 354(847-850), 2016.

[144] M. K. Bhaskar, D. D. Sukachev, A. Sipahigil, R. E. Evans, M. J. Burek, C. T. Nguyen, L. J. Rogers, P. Siyushev, M. H. Metsch, H. Park, F. Jelezko, M. lonča, and M. D. Lukin. Quantum Nonlinear Optics

with a Germanium-Vacancy Color Center in a Nanoscale Diamond Waveguide. *Physical Review Letters*, 118(223603), 2017.

[145] M. J. Burek, C. Meuwly, R. E. Evans, M. K. Bhaskar, A. Sipahigil, S. Meesala, B. Machielse, D. D. Sukachev, C. T. Nguyen, J. L. Pacheco, E. Bielejec, M. D. Lukin, and M. Lončar. Fiber-Coupled Diamond Quantum Nanophotonic Interface. *Physical Review Applied*, 8(024026), 2017.

[146] H. Thyrrestrup, G. Kiršanskė, H. Le Jeannic, T. Pregnolato, L. Zhai, L. Midolo, N. Rotenberg, A. Javadi, R. Schott, A. D. Wieck, A. Ludwig, M. C. Löbl, I. Söllner, R. J. Warburton, and P. Lodahl. Quantum optics with near lifetime-limited quantum-dot transitions in a nanophotonic waveguide. *arXiv:1711.10423*, 2017.

[147] B. Lang, R. Oulton, and D. M. Beggs. Optimised photonic crystal waveguide for chiral light-matter interactions. *Journal of Optics*, 19(045001), 2017.

[148] S. Mahmoodian, P. Lodahl, and A. S. Sørensen. Quantum Networks with Chiral-Light-Matter Interaction in Waveguides. *Physical Review Letters*, 117(241501), 2016.

[149] M. J. Collett and C. W. Gardiner. Squeezing of intracavity and traveling-wave light fields produced in parametric amplification. *Physical Review A*, 30(3), 1984.

[150] A. Reigue, J. Iles-Smith, F. Lux, L. Monniello, M. Bernard, F. Margaillan, A. Lemaitre, A. Martinez, D. P. S. McCutcheon, J. Mørk,

R. Hostein, and V. Voliotis. Probing Electron-Phonon Interaction through Two-Photon Interference in Resonantly Driven Semiconductor Quantum Dots. *Physical Review Letters*, 118(233602), 2017.

[151] H. S. Nguyen, G. Sallen, C. Voisin, Ph. Roussignol, C. Diederichs, and G. Cassabois. Optically Gated Resonant Emission of Single Quantum Dots. *Physical Review Letters*, 108(057401), 2012.

[152] C. Sayrin, C. Junge, R. Mitsch, B. Albrecht, D. O'Shea, P. Schneeweiss, J. Volz, and A. Rauschenbeutel. Nanophotonic Optical Isolator Controlled by the Internal State of Cold Atoms. *Physical Review X*, 5(041036), 2015.

[153] S. Mahmoodian, K. Prindal-Nielsen, I. Søllner, S. Stobbe, and P. Lodahl. Engineering chiral light–matter interaction in photonic crystal waveguides with slow light. *Optical Materials Express*, 7(43-51), 2017.